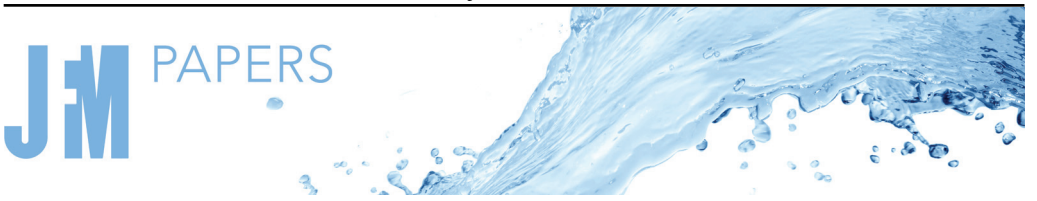
J. Fluid Mech. (2026), *vol.* 1026, A34, doi:10.1017/jfm.2025.10937



On the interdependence between flame shape and vortex breakdown mode in turbulent swirling reacting flows

Léo C.C. Mesquita[1,*], **Aymeric Vié**[2] and **Sébastien Ducruix**[2]

[1]Combustion Aerothermal - Fluid Mechanics, Rolls-Royce plc., Derby DE24 8BJ, UK

[2]CNRS, CentraleSupélec, Laboratoire EM2C, Université ParisSaclay, Gif-sur-Yvette 91190, France

Corresponding author: Léo C.C. Mesquita, leo.mesquita@rolls-royce.com

(Received 21 December 2024; revised 1 August 2025; accepted 13 October 2025)

This work uses large-eddy simulations to study the transition of a tulip flame stabilised by bubble vortex breakdown (BVB) mode towards a V flame stabilised by a conical vortex breakdown (CVB). The transition is triggered when the equivalence ratio is increased, resulting in a rise in temperature within the central recirculation zone (CRZ). Simultaneously, the pressure inside the CRZ bubble increases, while the average pressure inside the combustion chamber remains constant. This increase in pressure causes the CRZ bubble to open radially and expand, changing the vortex breakdown mode from BVB to CVB, and the flame shape from a tulip shape to a V shape. A criterion for a limit pressure inside the CRZ was then devised based on the radial momentum equation and the balance between centrifugal force and radial pressure gradient, found to control the radial motion of the CRZ. This criterion helped us to understand the main events of the transition, showing that, once the pressure inside the CRZ exceeds the limit given by the criterion, the flow topology changes from a BVB mode to a CVB mode. This transition highlights the differences between a BVB mode and a CVB mode, showing for the first time that there are characteristic pressure and velocity profiles for each mode in their swirling jets and CRZ. Finally, a significant achievement of this work is the identification of a novel mechanism for the controlled transition of vortex breakdown mode, a combustion-driven transition of vortex breakdown mode.

Key words: vortex breakdown, turbulent reacting flows, flames

[*] Results obtained while a researcher at Université Paris-Saclay, CNRS, CentraleSupélec, Laboratoire EM2C

© The Author(s), 2026. Published by Cambridge University Press.

https://doi.org/10.1017/jfm.2025.10937 Published online by Cambridge University Press

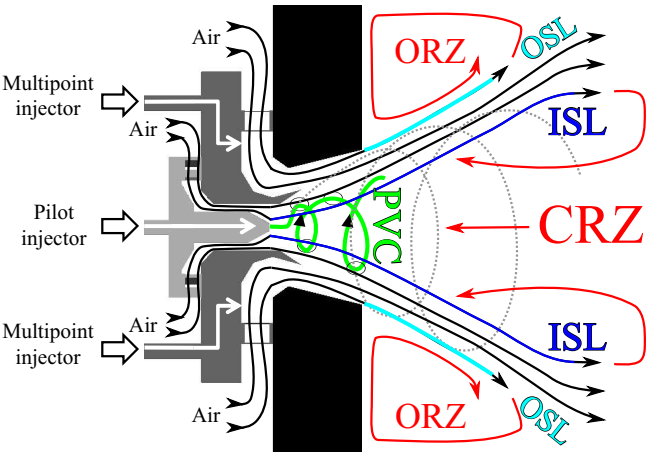


Figure 1. Schematic representing a typical swirling-flow topology within an aeronautical combustion chamber, showing the two-stage BIMER injector and main flow elements: ISL, OSL, CRZ, ORZ and a possible PVC.

1. Introduction

In flows with high velocities, like in aeronautical combustors, the continuous stabilisation of a flame to sustain the combustion process during operation is a fundamental part of a functional design. Roughly, three mechanisms must be in play to achieve this flame stabilisation: fuel and air must be supplied in order to create a flammable mixture; there must be a continuous source of heat to continuously initiate the combustion reactions; and flow topology and velocity must allow the flame to keep a stable position, not blowing the flame away. A common and clever solution to achieve most of the aforementioned mechanisms is to swirl the flow, inducing vortex breakdown to create a recirculation zone at the centre of the combustion chamber (Lucca-Negro & O'Doherty 2001; Syred 2006; Huang & Yang 2009; Lefebvre & Ballal 2010; Candel *et al.* 2014).

There are many techniques to create a swirling flow, varying from curved pipes to tangential flows, but the most conventional way employed in aeronautical combustors is to force the flow through a swirler before entering the chamber (Lefebvre & Ballal 2010). A swirler is a cylindrical mechanism with carved angular vanes (radial swirler) or with twisted blades (axial swirler) with the objective of increasing the magnitude of the tangential (or swirl) component of the velocity vector (Dodds & Bahr 1990).

The creation of a vortex breakdown for flame stabilisation leads to a complex flow topology inside a combustion chamber. This topology and its many zones of interest are summarised in the schematics in figure 1. One can observe the formation of a central recirculation zone (CRZ) and a toroidal outer recirculation zone (ORZ) at the chamber corners due to the swirling flow exiting the swirlers. This creates an inner shear layer (ISL) between the swirling helical jet and the CRZ and an outer shear layer (OSL) between the swirling helical jet and the ORZ. The possible presence of a helical hydrodynamic instability called the precessing vortex core (PVC) (Syred 2006) near the injector is also highlighted.

All these flow structures have a role in the flame stabilisation process. The recirculation zone attracts the burnt gases and, as they recirculate, they become a continuous source of heat to sustain combustion. Simultaneously, the shear layers create regions of low velocity, but with high turbulence (as the vast majority of applications are turbulent). If one thinks of premixed flames, which have a characteristic consumption speed (Kuo & Acharya 2012),

https://doi.org/10.1017/jfm.2025.10937 Published online by Cambridge University Press

in order to keep the flame in a fixed and stable position, the flow velocity should be of the same magnitude, but with an opposed direction to the flame's turbulent speed. The flame speed magnitude in the deflagration regime is generally somewhat limited and can hardly reach the bulk flow velocity of an aero-engine, so it is then necessary to create low velocity regions if one intends to stabilise a flame. In the topology of a swirling flow (figure 1), these low velocity regions are the ISL and OSL. As both are on the limits of the CRZ and ORZ, the ISL and OSL are within close proximity to the recirculating burnt gases, a constant heat source that ignites the mixture, in addition to the low velocities. However, in aeronautical combustors, fuel is delivered in liquid form, requiring mixing and resulting in partially premixed flames. A non-premixed region is located close to the injector, where the fuel is dense, while downstream burns a premixed flame, where the fuel is more thoroughly mixed. The shear layer remains a stabilisation zone for the flame in these cases, as its high turbulence accelerates fuel break-up and mixing (Lefebvre 1980; Lefebvre & Ballal 2010). Thus, vortex breakdown accomplishes two (and improves the third one) of the main mechanisms necessary to maintain a stable flame in an aeronautical combustion chamber, while providing a spatial anchoring zone for the flame.

It is precisely the interactions between flame, fuel stream and flow topology that determine the regions where the flame can stabilise and define what is commonly called the flame shape, which is a characteristic, stable topology that the flame has in space. Modifications to the flame reactivity or the flow field have the power to alter the flame topology; thus, multiple parameters influence the flame shape. The impact of parameters such as swirl number (Tangirala *et al.* 1987; Durbin *et al.* 1996; Stone & Menon 2002; Huang & Yang 2005; Idahosa *et al.* 2009; Tummers *et al.* 2009; Alekseenko *et al.* 2011; Driscoll & Temme 2011; Sweeney *et al.* 2012; Durox *et al.* 2013; Markovich *et al.* 2014; Guiberti *et al.* 2015; Parra-Santos *et al.* 2015; Chong, Lam & Hochgreb 2016; Santhosh & Basu 2016; Degeneve *et al.* 2019; Carneiro Piton *et al.* 2020; Kallifronas *et al.* 2023; Bae *et al.* 2024; Santhosh *et al.* 2025), fuel composition (Wicksall *et al.* 2005; Guiberti *et al.* 2015; Arndt *et al.* 2019; Agostinelli *et al.* 2022; Papafilippou, Chishty & Gebart 2022), equivalence ratio and preheat temperature (Chterev *et al.* 2014; Malbois *et al.* 2017; Taamallah *et al.* 2019; Tomasch *et al.* 2025), fuel dilution (Terhaar, Oberleithner & Paschereit 2014), fuel stratification or distribution between injectors (Providakis 2013; Hermeth *et al.* 2014; Renaud *et al.* 2015*b*; Cheneau *et al.* 2019*a*; Han *et al.* 2019) and evaporation rate (Domingo-Alvarez *et al.* 2020) are well known and broadly discussed. However, the impact of the vortex breakdown mode on the flame shape is not explicitly documented in the literature (other than the authors' own work, to the best of their knowledge), even if the effect of swirl number on the flame shape is common knowledge. In swirling flows, generally, flame shapes are named based on the shape of the flame cross-section. To illustrate, figure 2 presents various flames stabilised in the BIMER combustor from Mesquita (2021), which represent common aerodynamically stabilised flame shapes resulting from the use of shear layers as a stabilisation mechanism: figure 2(*a*) shows a tulip flame and figure 2(*b*) a V flame, both stabilised mostly by the ISL, while figure 2(*g*) shows an M flame, stabilised by the OSL and the CRZ. Looking at these three specific flames, one can see that their shapes are clearly different; however, this is not always the case when comparing tulip, V and M flames, as the differences can become more subtle. Taking the tulip flame of figure 2(*c*), the M flame of figure 2(*e*) and the V flame of figure 2(*f*), for example, all three have a shape that resembles the letter 'M', because all three have an OSL-stabilised branch and another branch close to the centreline. However, upon examining the details, one can see how they differ and why they belong to different families of flame shapes. The M flames (figures 2*g* and 2*e*) consistently have their leading edge lifted and aerodynamically stabilised behind the vortex breakdown bubble, therefore

https://doi.org/10.1017/jfm.2025.10937 Published online by Cambridge University Press

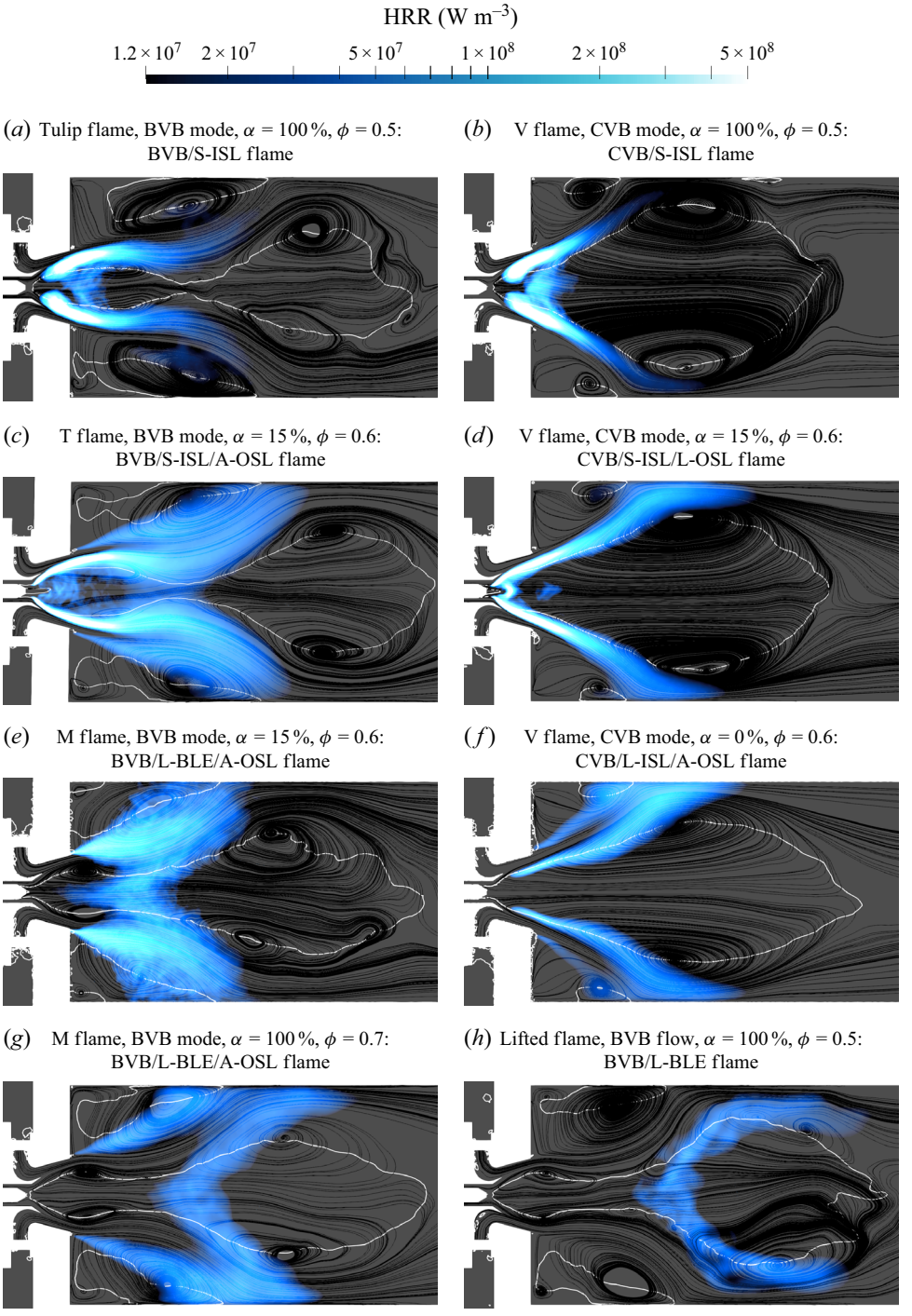


Figure 2. Large-eddy simulation time-averaged heat release rate (HRR) field with averaged two-dimensional flow streamlines and white iso-line of zero axial velocity of the BIMER combustor at various conditions presenting different flame shapes with their associated vortex breakdown modes, and the flame shape nomenclature of table 1. Here, ϕ is the global equivalence ratio, and the staging factor α is the fuel mass flow through the pilot injector over the sum of pilot and multipoint fuel mass flow.

https://doi.org/10.1017/jfm.2025.10937 Published online by Cambridge University Press

Vortex breakdown mode	Bubble vortex breakdown (BVB), Conical vortex breakdown (CVB), Coanda (COA), No vortex breakdown – wake (WAKE), No vortex breakdown – jet (JET)	
Inner branch stabilisation	Attached (A), lifted (L), fuel stabilised (F) or spray stabilised (S)	Inner shear layer (ISL), bubble leading edge (BLE) or absent ( )
Outer branch stabilisation	Attached (A), lifted (L), fuel stabilised (F) or spray stabilised (S)	Outer shear layer (OSL) or absent ( )

Table 1. Standard swirling flame shape nomenclature adopted in this work.

only existing in a BVB mode. In opposition, the characteristic exclusive element of all tulip and all V flames is that they are ISL stabilised, occasionally with an OSL-stabilised branch, thus labelling flames in figures 2(*c*) and 2(*f*) as M flames would be inconsistent and misleading. Another important point is the difference between tulip and V flames. Even if both are ISL-stabilised flames, their difference lies in the different vortex breakdown modes. It is precisely the BVB mode that confers the characteristic tulip-like shape of the tulip flame, or the CVB mode that defines the conically diverging shape of the V flame. Therefore, this highlights that it is not enough to name a flame solely by its appearance; the vortex breakdown mode and the flame stabilisation mechanism are needed to define a consistent nomenclature that clearly distinguishes different families of flame shapes. For example, the flame in figure 2(*h*) would likely be called a lifted V flame, however, as it is stabilised in a BVB mode, it cannot be a V flame if one follows the above nomenclature convention, thus classing it as a lifted tulip or a no-OSL-M would be more appropriate and fully consistent, especially when comparing it with the flames in figures 2(*c*) and 2(*g*).

There are other flame shape names that can be found in the literature, such as trumpet-like (Terhaar *et al.* 2014), annular flame (Terhaar *et al.* 2014), lifted (Han *et al.* 2019), S flame (Han *et al.* 2019), sV (Renaud, Ducruix & Zimmer 2017), W (Nogenmyr *et al.* 2011; Ciardiello *et al.* 2020), just to cite some. However, this non-universal nomenclature and the lack of consistency lead to confusion and increase the complexity of comparing flames from different works, as there is not a clear criterion to classify a flame other than one's interpretation of the flame shape. As another example, the V flames in figures 2(*b*) or 2(*d*) could be called W flames, because of their interaction with the spray. This shows that leaving to one's interpretation the resemblance of the flame transverse cut to a letter does not result in a consistent and comparable nomenclature. And to make this matter even more complex, the flow topology, which is an essential part of the flame stabilisation, is not considered when identifying the flame shape. To render the discussion in this work clearer, we will classify all the flame shapes using the following nomenclature, composed of three parts and summarised in table 1: first, the vortex breakdown mode is identified (CVB, BVB, Coanda flow or two possible stabilisations when there is no vortex breakdown, wake and jet stabilisation). Then, the inner branch stabilisation is characterised: if it has an attached, lifted, fuel-stabilised or spray-stabilised inner branch that is ISL stabilised, has a bubble leading edge or is fully stabilised by the fuel stream and not by the ISL. Finally, the outer branch stabilisation: if it has an attached, lifted, fuel-stabilised or spray-stabilised

https://doi.org/10.1017/jfm.2025.10937 Published online by Cambridge University Press

OSL branch or, if no OSL branch is present, this part is omitted. Figure 2 illustrates the application of this nomenclature to the BIMER combustor flames from Mesquita (2021). This nomenclature will be used throughout this work to facilitate comparisons between flames from different studies that may be of the same family, despite having different names.

The discussion, nomenclature and flame images above illustrate that the vortex breakdown mode, because it controls the swirling flow topology, is as central to defining the flame shape as the flame chemistry. However, apart from our work in Mesquita *et al.* (2021*a*), Mesquita *et al.* (2021*b*) and Mesquita *et al.* (2023*b*), the authors are unaware of any publications that explicitly discuss flame shape transitions and their correspondence to changes in vortex breakdown mode. Moreover, studies specifically addressing vortex breakdown mode transitions caused by combustion could not be found. The present work aims to bridge this gap by using large-eddy simulations (LES) to study a swirl-stabilised aeronautical burner where a flame, initially in a tulip shape (figure 2*a*), changes to a V shape (figure 2*b*) after an increase in equivalence ratio, while the vortex breakdown mode transitions simultaneously from the BVB mode to the CVB mode. Instead of aiming for linear stability analysis (Dagan, Arad & Tambour 2016; Oberleithner *et al.* 2011, 2015), space-state bifurcation analysis (Douglas, Emerson & Lieuwen 2022) or numerical simulations (Moise & Mathew 2019; Moise 2020; Moise & Mathew 2021; Keeton *et al.* 2022) for simplified systems, we focus on a comprehensive physical study of a case representative of a practical aero-engine combustor to understand the role of one of the main operating parameters of a flame – the equivalence ratio – in defining the flame shape. We demonstrate how increasing the equivalence ratio causes the flame to impose a transition of the vortex breakdown mode. Moreover, we demonstrate that there is an interdependence between the vortex breakdown mode and the flame shape: the change in vortex breakdown mode caused by the flame ultimately changes the flame shape in accordance with the new vortex breakdown mode. Therefore, we propose a stability criterion for the BVB mode in reacting media that can be linked to operating conditions, as understanding the limits of stability of the vortex breakdown mode is central to the stable operation of the flame and the combustor. This work builds upon the study by the authors in Mesquita *et al.* (2021*a*), where a vortex breakdown mode transition was identified as responsible for a change in flame shape and for altering the stability of the burner. This represents a step forward from the recent works of Moise & Mathew (2021) and Keeton *et al.* (2022) in understanding this phenomenon in a real engineering application, as we explicitly model the swirler, the turbulent flow, and the combustion process.

The paper is organised as follows: first, we present a literature review on vortex breakdown phenomena, vortex breakdown mode transitions and flame shape transitions. Second, the experimental rig and operating conditions are described. Then, the numerical set-up is presented, along with the initialisation procedure. In the results section, the transition in flame shape and the flow are shown and analysed, followed by the definition of a criterion that can predict the stability of the vortex breakdown mode in this case. Finally, a discussion is proposed on the criterion, as it is applied in other cases in the same combustor.

2. Literature review of flow and flame transitions

2.1. *Vortex breakdown*

The vortex breakdown phenomenon occurs when the flow swirl velocity is sufficiently high to create an adverse pressure gradient in the axial direction while centrifuging the flow outward and to form a stagnation point at the centre of the swirling axis (Brown &

https://doi.org/10.1017/jfm.2025.10937 Published online by Cambridge University Press

Lopez 1990; Lopez 1990; Lucca-Negro & O'Doherty 2001). This forces a sudden radial expansion of the swirling vortex, creating a depression at its centre. As the swirl velocity decays axially, so does the pressure depression at the centre of the swirling vortex, inducing a reverse axial flow and creating a CRZ. This process is described and illustrated by Syred (2006). The formation of a CRZ due to vortex breakdown was classified by Harvey (1962) as the transition between weakly and strongly swirled flows; however, Harvey (1962) reported different vortex breakdown modes depending on the level of swirl. Sarpkaya (1971) first identifies three types of vortex breakdown while performing experiments in laminar flows, for which the ratio of tangential to axial velocity was progressively increased at a fixed flow rate Reynolds number (Re) ≈ 5000: the first mode to appear for the lowest swirl levels is the spiral vortex breakdown, where the swirling vortex creates a helical structure. Then, if the swirl level is further increased, the spiral mode transitions to an (axisymmetric) BVB mode, creating a bubble-like CRZ. Finally, the double-helix vortex breakdown is a special mode that is observed when very slow ($1/60°/\mathrm{s}$) changes in swirl velocities are applied, creating a double-helix structure. If the swirl level is further increased or if the system is disturbed, the flow transitions to the BVB mode. The last mode was observed much later when Sarpkaya (1995) performed new experiments to study turbulent vortex breakdowns. At $Re = 200\,000$ and circulation number $\Omega = \Gamma/U_0 D_0 = 0.50$ (where Γ is the circulation of the vortex, U_0 is the cross-sectionally averaged axial velocity and D_0 is the tube diameter), Sarpkaya (1995) observed the BVB mode develop to a vortex breakdown with a fully conical shape, with linear growth from the stagnation point to the end of the wake, naming it the CVB mode. Sarpkaya (1995) then stated that the CVB should be considered as the fourth fundamental type of vortex breakdown, in addition to the spiral, bubble and double-helix types.

In a later study, Billant, Chomaz & Huerre (1998) also observed the appearance of BVB and CVB in a non-confined swirling flow. They gave further insights into the flow around and inside the recirculation zones of the two vortex breakdown modes. As reported by other researchers, the BVB mode bubble exhibits a diverging flow that is followed by a contraction, resulting in the ovoid shape of the CRZ and in the creation of a toroidal vortex ring that recirculates the fluid. The flow inside the bubble is well organised and strong. In the CVB mode, which Billant *et al.* (1998) were the first to characterise in detail, the flow expands from the stagnation point, but there is no contraction further downstream, as the flow recirculates inside the cone, also creating a toroidal vortex ring at the base of the cone. The conical sheet that separates the swirling jet from the CRZ is unstable and begins to distort and roll up into vortices before breaking into turbulence further downstream. The authors state that these instabilities might come from streamwise shear and/or centrifugal instabilities. From their observations of the flow in the CVB mode, Billant *et al.* (1998) argue that the CVB observed by them differs from the one observed by Sarpkaya (1995), as the conical state reported in the latter is 'in fact a bubble whose turbulent conical wake has come so close to the stagnation point that the whole structure looks like a cone (. . .) appearing as the natural evolution of the wake of a bubble towards a turbulent state as Re is increased'. Thus, since the conical state reported by Sarpkaya (1995) does not display any of the characteristics observed by Billant *et al.* (1998) (such as the important quasi-steady, organised flow inside the cone), Billant *et al.* (1998) state that the conical mode represented in their study should be regarded as a reference CVB.

2.2. *The BVB-CVB vortex breakdown mode transitions*

Despite the different modes being well characterised, no single mechanism fully describes all the transitions between the BVB and the CVB modes found in the literature. Several

https://doi.org/10.1017/jfm.2025.10937 Published online by Cambridge University Press

works report this transition in various configurations, discussing multiple mechanisms; however, in all cases, the swirl level and the relationship between axial and swirl velocity are key parameters for the onset of the two vortex breakdown modes, with the triggering parameter varying in each case.

Sarpkaya (1995), who first described the BVB-CVB mode transition, observed the change of mode increasing the Reynolds number from $Re = 10\,000$ up to $Re = 250\,000$, while the circulation number was kept around $\Omega \approx 0.6$ in a water tank. As the Reynolds number increases, the wake behind the bubble moves upstream until it merges with the bubble, resulting in a full CVB. However, as aforementioned, Billant *et al.* (1998) questions the observation of a CVB by Sarpkaya (1995), thus the Reynolds number as a cause for the transition from the BVB to the CVB must also be regarded with caution.

Indeed, in opposition to Sarpkaya (1995), to trigger vortex breakdown mode transitions Billant *et al.* (1998) progressively increased the swirl level (characterised by the swirl parameter, $S_{pa} = 2V_\theta(R/2, x_0)/V_x(0, x_0)$, which puts in relation the tangential velocity V_θ at the centre of the jet ($V_\theta(R/2, x_0)$) and the axial velocity V_x, both measured at the axial position of the initiation of vortex breakdown, where R is the radius of the nozzle exit), but keeping the Reynolds number constant. Starting from a fully axial jet, the swirl parameter was progressively increased, causing the jet to become distorted, then helical and, eventually, an axisymmetric BVB was formed, which could be stable or later slowly evolve into an axisymmetric CVB. Thus, Billant *et al.* (1998) observed that the two vortex breakdown modes, bubble and conical, coexisted for the same values of Reynolds number (in the range $300 < Re < 1200$) and swirl parameter, creating bi-stable states. Even if the data available were not enough to propose a mechanism explaining why the change in vortex breakdown mode would sometimes be triggered, Billant *et al.* (1998) found that temperature perturbations of the order of 0.1 °C had some influence in defining which vortex breakdown mode would appear. The authors supposed that buoyancy effects could be at the origin of this influence, with higher jet temperatures (compared with the tank temperatures) favouring the appearance of CVB.

Terhaar *et al.* (2015), studying the addition of an axial air stream at the centre of the swirler as a way to mitigate flashback risks in swirling combustors, observed that increasing the axial flow rate triggered a change in vortex breakdown mode for isothermal flows. For a constant high swirl number ($S = 0.9$), when the axial injection rate is increased to over 10 % of the total air injection rate, the CRZ expands and the vortex breakdown mode changes from the bubble to the conical mode. After a parametric study, Terhaar *et al.* (2015) derived a model and mapped the triggering of the mode change for the isothermal flow as a function of the level of swirl and axial flow injection rates. While the authors clearly state that the onset of vortex breakdown is controlled by the swirl number, the resulting vortex breakdown mode (BVB or CVB) is not a sole consequence of the swirl number, both appearing for various swirl numbers as for Billant *et al.* (1998). However, unlike Billant *et al.* (1998), who found that small temperature differences triggered the transitions, for Terhaar *et al.* (2015), the shape of the inflow velocity profile seemed to determine the selection of the vortex breakdown type. High primary swirl number at high rates of axial injection promoted CVB, whereas the same swirl number without axial injection resulted in a BVB. Even if reacting conditions were also analysed, when a methane lifted flame was present, no change in vortex breakdown mode was observed with the increase in axial flow, the vortex breakdown mode remaining the bubble one.

More recently, Santhosh, Miglani & Basu (2014) and Rajamanickam & Basu (2018) observed the formation of a CVB in an isothermal flow with two coaxial jets (an internal central axial jet and an external tangential one) while varying the swirl number for various Reynolds numbers. Vortex breakdown forms when the swirl number attains a certain

https://doi.org/10.1017/jfm.2025.10937 Published online by Cambridge University Press

value, but only in cases where the tangential jet dominates the flow. In these two works, this regime is characterised by a modified Rossby number $Ro_m = |\Delta u_y|/u_\theta < 1$, where Δu_y is the difference of the bulk velocity based on the mass flow rate and tube surface section between the two jets and u_θ is the tangential velocity of the tangential jet. As in Billant *et al.* (1998), first a BVB is observed, but this time, when the swirl number is further increased (keeping $Ro_m < 1$), the vortex breakdown mode changes into a CVB, the change being clearly triggered by the increase in swirl number. However, increasing the swirl further makes the vortex breakdown mode re-transition into a bubble mode. Thus, Rajamanickam & Basu (2018) stresses that CVB exists only for a very narrow band of swirl number S_G. Additionally, they note that CVB was observed for vane swirlers, but only with coaxial jets. A similar statement is made by Terhaar *et al.* (2015), where the authors claim the CVB mode could be linked with a simultaneous high level of swirl and axial flows in the jet, creating a specific and propitious inlet velocity profile that allows the stabilisation of the CVB mode. Comparing the results, it is possible to infer that the CVB observed by Rajamanickam & Basu (2018) is a similar state as the one observed by Billant *et al.* (1998), characterised by the quick opening of the swirling jet and by a slow, organised and quasi-steady flow inside the CRZ, as illustrated by the streamlines for the $S_G = 2.53$ CVB case.

In a subsequent group of studies, Moise & Mathew (2019) used direct numerical simulations (DNS) to study the effect of increasing swirl number on the topology of laminar swirling flows, confirming past experimental observations and the transition from spiral vortex breakdown to BVB, and finally to CVB. Afterwards, Moise (2020) discussed the co-existence of both BVB and CVB for the same swirl number, highlighting the importance of hysteresis effects on swirling flow topologies. Following these studies, Moise & Mathew (2021) used LES to investigate the impact of turbulence on vortex breakdown modes. They observed a similar progression in the turbulent regime – BVB to CVB with increasing swirl – but additionally reported the emergence of a wide-open CVB structure, likely associated with a Coandă-type attachment of the flow to the wall. Moise & Mathew (2021) thoroughly characterised each of the modes, showing the flow fields and discussing the exclusive characteristics of each of the modes.

In parallel, Douglas *et al.* (2022) used space-state global bifurcation analysis (in a different approach to linear stability analysis of Terhaar *et al.* 2015; Dagan *et al.* 2016) to provide a stability map of different swirling flow modes of a laminar annular jet as a function of swirl number, Reynolds number and centre-body diameter. They identified the three modes: (i) wake, a pre-breakdown flow; (ii) vortex breakdown, a BVB-like isolated central recirculation bubble; and (iii) wall jet, which can be divided into two regimes: a CVB-like regime where the recirculation bubble expands radially due to the influence of wall-jet entrainment, but with the jet still separated from the wall, and a wide-open CVB-like configuration (as per the Moise & Mathew 2021 definition) where the jet attaches along the outer wall due to a full Coandă effect. These transitions were characterised through a sequence of bifurcations, including symmetry-breaking Hopf and saddle-node bifurcations, along with pronounced hysteresis loops. They retrieve the classic onset of BVB as swirl increases enough to generate a stagnation point and reverse flow on the axis; however, Douglas *et al.* (2022) show that the vortex breakdown can occur at lower swirl levels caused by flow perturbations induced by a PVC, for example. The transition to CVB involves the merging of this bubble with the wake behind the bluff body and the radial expansion of the bubble, but more importantly, the study concluded that the transition to CVB is governed by a nonlinear exchange of dominance between the central low-pressure region associated with the vortex breakdown recirculation zone and the outer low-pressure region generated by wall-jet entrainment. At even higher swirl, the Coandă effect drives

https://doi.org/10.1017/jfm.2025.10937 Published online by Cambridge University Press

the formation of a wall-attached jet analogous to the wide-open CVB of Moise & Mathew (2021). Another important result from Douglas *et al.* (2022) for the context of this work is the conclusion that a transition to or from the wall-jet (or CVB) regime is unlikely to occur spontaneously due to flow and swirl level fluctuations, normally requiring a significant change in bulk flow swirl level. The authors argue that a BVB-CVB transition due to flow fluctuations would require strong perturbations, such as external forcing or special initial conditions, that could cause the flow to 'jump' spontaneously between the breakdown (BVB) and wall-jet (CVB) solution manifolds. This conclusion is similar to that of Mesquita *et al.* (2021*a*), which demonstrated how flow oscillations induced by a thermoacoustic instability led to a transition from the CVB mode to the BVB mode. Douglas *et al.* (2022) also found that larger centre-body diameters and higher Reynolds numbers lower the critical swirl needed for these transitions, due to increased azimuthal momentum and reduced entrainment, respectively. Their analysis reveals that even in laminar flows, these mechanisms produce a richly structured and multi-stable parameter space.

Finally, Keeton *et al.* (2022) employed theoretical and numerical approaches to study vortex breakdown in variable-density laminar swirling jets. They assessed the effect of increasing the swirl number for cases with different density ratios between the swirling jet and the atmosphere. This work provides a first insight into how swirling flow topologies could behave under reacting conditions. The authors demonstrate that altering the jet-to-ambient density ratio impacts the critical swirl number that triggers the BVB and CVB modes, revealing a significant decrease with increasing density ratio for thin initial shear-layer thicknesses. However, for thicker initial shear layers, the critical swirl numbers showed little dependence on the density ratio.

These few works addressing the transition of BVB to CVB mode highlight the complexity of the problem. In particular, Rajamanickam & Basu (2018) emphasise the scarcity of available studies on CVB and the limited understanding of the problem. Despite the investigation of various parameters triggering the BVB-CVB transition (Reynolds number, temperature, inlet velocity profile, geometry and swirl number) and the fact that all the works that observed a CVB (Sarpkaya 1995; Billant *et al.* 1998; Santhosh *et al.* 2014; Terhaar *et al.* 2015; Rajamanickam & Basu 2018; Moise & Mathew 2019; Moise 2020; Moise & Mathew 2021; Douglas *et al.* 2022; Keeton *et al.* 2022) showed that it evolves from an already stabilised BVB, it is still an open question if a general mechanism controlling the change of a BVB into a CVB exists. Moreover, Moise (2020), Moise & Mathew (2021) and Keeton *et al.* (2022) stress the importance of further studying the effect of temperature on BVB to CVB transitions.

Furthermore, when considering turbulent reacting flows, the study of BVB to CVB transitions, and in particular their impact on the change in flame shape, is even less documented in the literature. Even if vortex breakdown mode transitions are likely to occur simultaneously with the flame shape changes (and vortex breakdown mode changes are certain to impact the flame shape), the existing studies of transitions and bifurcations in reacting flows focus only on flame shape changes as a function of operating parameters, rather than the flow topology. Nevertheless, some works where these phenomena might be happening simultaneously are discussed in the following paragraphs, as well as other works that provide relevant context for this study.

2.3. *Flame shape transitions*

2.3.1. *Swirl number effect*

Among the several works discussing the well-known effect of swirl number on flame shape, it is essential to highlight the study by Santhosh & Basu (2016) in the context of

https://doi.org/10.1017/jfm.2025.10937 Published online by Cambridge University Press

this work. Following their non-reacting studies in Santhosh *et al.* (2014) and Santhosh & Basu (2016), the authors used the same unconfined co-axial double-concentric pipe set-up to study the effect of changing the swirl number on the average flame shape in a reacting medium. By progressively increasing the tangential momentum of the external pipe air flow, while maintaining the central fuel pipe as a fully axial flow, they observed two regimes of change in flame shape, which they classified as primary transition and secondary transition. The primary transition consisted of a change in flame shape from a zero-swirl straight jet flame (JET/F), to a lifted flame with blue base (WAKE/L-BLE), then to a swirling flame (BVB/A-ISL), as the swirl number is progressively increased, showing the impact of vortex breakdown on the axial position and shape of the flame. The secondary transition characterises the change in flame shape for the cases where initially the central axial fuel jet penetrates through the BVB created by the swirling flow from the external co-axial pipe. This interaction creates an initial state that the authors call a 'dual ring' average flow structure, where the recirculation zone, on average, is composed of two concentric toroidal vortices, the external one from the BVB mode, and the internal as a consequence of the interaction of the axial jet with the recirculation zone. This flow field leads to a flame shape that the authors identify as a swirling flame with a conic tailpiece (a BVB/A-ISL with a central tail due to the central axial jet). From the 'dual ring' state, if the swirl number is further increased, the modified Rossby number becomes close to zero ($Ro_m = |\Delta u_y|/u_\theta \approx 0$), meaning that the pressure gradient due to rotational effect dominates over the pressure gradient due to axial jet entrainment. This results in the suppression of the axial jet's influence on the flow topology, which transitions from the 'dual ring' state to the well-known axisymmetric BVB. The flame shape changes accordingly, losing the tailpiece and moving to a high swirl lean flame (BVB/A-ISL). Even if in the Santhosh & Basu (2016) study there is no change of vortex breakdown mode (but rather a change in topology due to variations of axial and tangential momentum between the co-axial streams), the authors show how a change of operating conditions changes the flow topology, and how this change of flow topology consequently changes the flame shape. This is an important evidence of the link between swirling flow topology and flame shape; however, in the case of Santhosh & Basu (2016), it seems that there is little influence of the flame on the flow field, as the same analysis and conclusions of the flow field evolution can be drawn for the non-reacting case.

2.3.2. *Equivalence ratio effect*

Chterev *et al.* (2014) explored how flame shapes and flow structures evolve in an annular, premixed, swirl-stabilised combustor, with an aerodynamic centre body, resulting in aerodynamically stabilised flow and flame. The authors observed four different flame shapes while increasing the fuel (gaseous natural gas) equivalence ratio and keeping the same flow swirl:

(i) flame I: a very weak lifted flame stabilised behind the vortex breakdown bubble stagnation point (seemingly a weak BVB/L-BLE flame, even if the vortex breakdown mode is not identified);
(ii) flame I': heat release increases to significant values and the flame keeps its completely lifted stabilisation (also seemingly a BVB/L-BLE flame, but stronger and wider than Flame I, now similar to figure 2*h*);
(iii) flame BB: the further increase in equivalence ratio makes the flame propagate upstream over the OSL, creating an M-shaped flame (BVB/L-BLE/A-OSL, similar to figure 2*g*) attached to the chamber entrance lips;

https://doi.org/10.1017/jfm.2025.10937 Published online by Cambridge University Press

(iv) flame IV: even further increasing the equivalence ratio makes flame BB abruptly bifurcate, stabilising also in the ISL, rather than over the vortex breakdown stagnation point. Chterev *et al.* (2014) claimed that this bifurcation happened because of combustion-induced flow separation along the centre body, leading the flame to stabilise upstream of the combustor inlet. Although the authors do not discuss or address this in their work, examining the flame image (similar to figure 2*f*) suggests that the flow field topology and vortex breakdown mode may also have changed with the flame shape. This transition appears to significantly impact the flow field, as it causes the leading edge of the flame BB to move upstream and anchor at the centre body, resulting in a flame IV that is an attached conical V flame, thus becoming a CVB/A-ISL/A-OSL flame. This could suggest a simultaneous transition from a BVB to a CVB, coinciding with the transition in flame shape.

Taamallah *et al.* (2019) also investigated the change in flame shape caused by the progressive increase in equivalence ratio from the lean blow off limit for gaseous CH_4-H_2 flames. As the equivalence ratio is progressively increased, first a columnar lifted flame is formed (flame I), stabilised behind the recirculation zone and extending in the entire combustion chamber (similar to Chterev *et al.* 2014, flame I). The authors note that the flow is similar to the non-reacting case, both of which, in the authors' view, share a CVB. However, the flow field measured by Particle image velocimetry (PIV), as shown by the authors, appears to have characteristics of a BVB rather than a CVB. Indeed, as the equivalence ratio is increased, the flame tip moves upstream until it reaches the swirler centre body, anchoring at this position (flame II) and expanding the recirculation zone, as shown by the PIV flow field images. The authors claim that the transition from flame I to flame II causes the CRZ to close and to change from a CVB to a BVB. However, the PIV images presented suggest the opposite: a transition from BVB to CVB as the flame goes from shape I to II. Additionally, the authors state that further increasing the equivalence ratio from flame II leads to the flame stabilising 'along the ISL with a conical shape (flame III)', but the flow would still keep a BVB, which appears inconsistent. Indeed, as described by Billant *et al.* (1998) and Rajamanickam & Basu (2018), the CRZ in a BVB is shorter and narrower than the CVB. Observing closely the experimental images in Taamallah *et al.* (2019) and, in particular, the numerical simulations of the same experiments in Tomasch *et al.* (2025), one may think that the CRZ present in the non-reacting flow and flame I resembles more a BVB mode and flames II, III and IV, a CVB one, as the CRZ expands and becomes larger and longer. Furthermore, flames II and III resemble the ones in figures 2(*b*) and 2(*d*), respectively, also suggesting a CVB mode. Taamallah *et al.* (2019) present the flow field solved with LES, comparing the non-reacting and reacting cases to highlight the differences in the vortex breakdown mode. However, the LES CRZ presented in Taamallah *et al.* (2019) appears to be more upstream and of a different shape than the experimental one, and it is known that numerical methods can predict the wrong flow topology due to various set-up choices. This becomes particularly evident when analysing the more recent LES study by Tomasch *et al.* (2025), where the numerical results closely match the experimental data, supporting the hypothesis of a non-reacting BVB mode and that the flames trigger a change towards a CVB mode by a slow transition or by combustion-induced vortex breakdown (Konle & Sattelmayer 2009), even though this is not part of the paper's discussion. Unfortunately, neither Taamallah *et al.* (2019) nor Tomasch *et al.* (2025) provided more information on the vortex breakdown change, its temporal evolution or the flame's influence over it. This is another argument supporting the systematic identification and matching of the vortex breakdown mode with the flame shape, as two different modes seem to be present in Taamallah *et al.* (2019). Continuing to increase the equivalence ratio

https://doi.org/10.1017/jfm.2025.10937 Published online by Cambridge University Press

from flame III makes the flame front propagate to the ORZ, stabilising a 'double-annular flame' (flame IV) (seeming a CVB/A-ISL/A-OSL flame, similar to figure 2*f*).

Guiberti *et al.* (2015), Taamallah *et al.* (2015*b*, 2016) and Foley *et al.* (2017) carefully investigated the transition when the flame front from an ISL-stabilised flame propagates to the OSL by the progressive increase of the equivalence ratio, each proposing a Karlovitz number-based criterion. Taamallah *et al.* (2015*b*) and Taamallah, Shanbhogue & Ghoniem (2016) concluded that vortical structures would be the responsible for entraining a reaction kernel to the ORZ, igniting the mixture inside it. This phenomenon would only be possible beyond a critical equivalence ratio, which would create an ignitable mixture inside the ORZ. The wall heat losses were also noted to have some influence on this transition. Huang & Yang (2004), and Taamallah *et al.* (2015*a*) studied how this transition and the stabilisation of the flame over the OSL trigger thermoacoustic instabilities. However, these phenomena are only shown to influence the stabilisation of the OSL branch of the flame, with no mention (or evidence) that they affect the vortex breakdown mode.

Malbois *et al.* (2017) studied experimentally a lean-premixed aero-engine injection system operated with kerosene in the HERON (High prEssuRe facility for aerO-eNgines) single sector high-pressure optical combustion chamber from SAFRAN Helicopter Engines. Two different flame shapes were observed depending on the equivalence ratio and operating pressure. For the majority of the operating conditions, a 'tulip-shape' flame that is mostly straight and confined at the centre of the combustion chamber was observed (similar to figure 2*a*, so seemingly a BVB/S-ISL flame, even if the vortex breakdown mode is not mentioned). However, when increasing the mixture equivalence ratio for an operating pressure of 0.41MPa, the tulip flame transitions to a V-shaped flame with a wider radial opening, forming a large CRZ and interacting with the walls (similar to figure 2*d*, so seemingly a CVB/S-ISL flame, even if the vortex breakdown mode is not mentioned). The authors observe that OH is already present at the inlet of the combustion chamber for both flames, suggesting that the combustion process begins upstream of the combustion chamber and thus that the flames are stabilised within the injection system. The authors also observe that the flame can switch suddenly between shapes. However, no details are given on the flow topology, vortex breakdown mode, the mechanisms leading to the stabilisation of either flames or on the transition itself.

In a subsequent experimental study, Legros *et al.* (2021) made detailed measurements of the axial velocity field for non-reacting and reacting conditions with varying pressures and Fuel-to-Air ratio. The authors demonstrate that the non-reacting axial velocity field is remarkably similar to the tulip flame flow field, both characterised by a small, elliptic, and elongated bubble CRZ. The authors also note that the increase in pressure reduces the length of the CRZ. The axial velocity field of the V flame, however, is quite different to the non-reacting one, with a wide and broad CRZ, indicating the flame's influence on the flow field. However, no insight is given into the causes of the bifurcation to a V flame. Even if not mentioned by the authors, it appears that the non-reacting and tulip flames exhibit a BVB mode, while the V flame displays a CVB mode.

Two separate LES works were conducted by Rochette (2019) and Domingo-Alvarez *et al.* (2020) to gain more insight into the tulip and V flames in the HERON rig and to understand the transition. However, due to a lack of experimental measurements on spray boundary conditions, none of the studies were able to reproduce the two flames. Rochette (2019) obtained numerically a lifted flame, different from both experimental V and tulip flames, while Domingo-Alvarez *et al.* (2020) retrieved the same lifted flame as Rochette (2019), but could simulate the tulip flame, after doing a parametric study on the spray boundary conditions. Domingo-Alvarez *et al.* (2020) showed that the difference between stabilising a lifted or a tulip flame depends on the evaporation time scale, which

https://doi.org/10.1017/jfm.2025.10937 Published online by Cambridge University Press

is impacted by the chosen injection diameter for the droplets. However, since none of the numerical works managed to simulate both flames and the transition from Malbois *et al.* (2017) and Legros *et al.* (2021), no further insight into the transition was provided, and the mechanisms behind the change of flame shape observed by Malbois *et al.* (2017) are yet to be investigated and explained.

2.3.3. *Fuel dilution effect*

Terhaar *et al.* (2014) studied the effect of increasing steam dilution in gaseous methane–hydrogen flames, as dilution is expected to significantly reduce the flame speed and reactivity. Thus, this study goes in the opposite direction of Chterev *et al.* (2014), Malbois *et al.* (2017) and Taamallah *et al.* (2019), where the equivalence ratio was progressively increased. The level of steam dilution was found to affect the stabilisation of the flame, and three different flame shapes were observed, each presenting different flow features. The first flame (I) is a short, compact hydrogen V-flame anchored at the centre body (similar to figure 2*b*, seemingly a CVB/A-ISL flame, even if the vortex breakdown mode is not identified). Reducing the amount of hydrogen and/or steam diluting this flame, it starts becoming longer, but still anchors at the centre body, progressively changing into the long V-flame (II) (similar to figure 2*d*, so seemingly a CVB/L-ISL flame, even if the vortex breakdown mode is not identified). The anchored V-flame presents a significantly different flow field from the non-reacting case: the jet is more radially open, with higher axial and radial velocities and a wider CRZ with slower and less turbulent back flow inside it. Temperatures are very high, and burnt gases fill both CRZ and ORZ. No PVC is present, as it is suppressed by the flame. The vortex breakdown mode is not mentioned by the authors; however, the characteristics match those of a CVB mode, as the CRZ exhibits a clear conical shape. From flame II, if the steam dilution is further increased, the flame abruptly changes into a very long 'trumpet-like' flame (III) or T flame, detaching from the centre body and anchoring in its wake (similar to the tulip flame in figure 2*a*, so seemingly a BVB/A-ISL flame, even if the vortex breakdown mode is not identified). Terhaar *et al.* (2014) also present the T-flame flow field, where the CRZ is now narrow, with the jet also presenting a small opening angle. Some characteristics of the CRZ are visible: near the swirling jet entrance, it has a stretched bubble-like shape (which is hot and highly turbulent), followed by a contraction and re-expansion, creating an hourglass-like shape. The authors also do not mention the vortex breakdown mode, but it seems to be a BVB. It is also noted that the recirculating flow inside the CRZ for the T flame is considerably larger than that in the non-reacting case. As in the V flame, both CRZ and ORZ are filled with hot, burnt gases. As this flame is not attached to the centre body, but rather stabilised a little downstream in its wake, a PVC was able to form and stabilise. Further increasing the steam dilution rate leads to the flame detaching into an annular lifted shape (IV) (no flow field is present, so it could be a BVB/L-BLE/L-OSL flame similar to figure 2*e*). This abrupt detachment can occur from the trumpet-like flame (III) or directly from the V flame (II). Continuing to increase the steam dilution from flame (IV) leads to the flame being more distributed inside the chamber, located further downstream and closer to the walls (similar to an M flame in figure 2*g*, so seemingly a BVB/L-BLE/L-OSL flame). For the lifted annular flames, the flow field is very similar to the non-reacting case and also resembles the one for the T flame: the CRZ bubble (which is no longer stretched), the contraction, and re-expansion are visible. For the lifted flame, the jet opening is smaller than the non-reacting case due to the presence of hot gases only inside the ORZ. The CRZ exhibits a highly turbulent cold flow, which appears to be the reason the flame detaches from the centre body, as the equivalence ratio is reduced, thereby quenching the flame.

https://doi.org/10.1017/jfm.2025.10937 Published online by Cambridge University Press

As the flow is very close to the non-reacting case, a PVC was also observed. These results give valuable, detailed insights into how the mixture composition strongly affects the flame stabilisation. The decrease in reactivity and flame speed makes the flame detach from the bluff body and stabilise downstream. Furthermore, it frames how each flame interacts with the flow field to create unique flow features.

2.3.4. *Fuel stratification effects*

In staged fuel injectors, some studies discuss how flame shape transitions are caused by a change in the ratio between fuel injected by each stage. Hermeth *et al.* (2014) studied the occurrence of bistable flames in a two-staged gaseous industrial burner and the triggering of the transition caused by the change in fuel staging. The authors showed that two different flame shapes were possible for the same operating conditions: an attached M flame (similar to figure 2*f*, seemingly a CVB/A-ISL/A-OSL flame, even if the vortex breakdown mode is not identified) and a lifted M flame (similar to figure 2*g*, seemingly a BVB/L-BLE/A-OSL flame, even if the vortex breakdown mode is also not identified). To achieve this, a different path must be taken while changing the operating conditions to allow the stabilisation of each of the flames. To obtain the attached M flame at the operating point of interest, the operating parameters (namely, pressure, compressor temperature, air and fuel mass flow rates at each stage) must be increased slowly in a quasi-steady manner, allowing the flame to maintain its original attached shape. When operating conditions are changed abruptly, the flame detaches, stabilising in the lifted M shape. The authors observed significantly different HRRs, velocity, and temperature fields for each of the flames, with a PVC only present in the lifted M flame. In particular, the flow topology differs, seemingly indicating a change in vortex breakdown mode as the flame changes, although this is not discussed by the authors. Additionally, the acoustic activity of each flame was investigated through the construction of flame transfer functions for each flame, revealing that the detached flame exhibited a higher response amplitude for all studied frequencies, indicating that it was more acoustically active than the attached one. Finally, Hermeth *et al.* (2014) also studied other ways of triggering the flame bifurcations after they were stabilised on the operating conditions of interest. The first transition studied was from the attached M flame with a large CRZ to the lifted M flame, where a bubble-like CRZ is present. The first way to trigger this transition was to modify the pilot fuel ratio (defined as the ratio between the current pilot fuel mass flow rate and the nominal pilot fuel mass flow rate). This ratio controls the local equivalence ratio in different parts of the flame. The authors observe that the flame detaches when this ratio is reduced below 0.5 or increased beyond 4.0, highlighting that there is an ideal range of local equivalence ratio where an attached flame is possible. The second transition, from the lifted M flame to the attached M one, is triggered by introducing a forced modulation of the flow. The flame leading point of the lifted M flame flashes back when the forcing amplitude is higher than 30 % of the mean diagonal inlet velocity. Each of these mechanisms only affects the flames in one direction, meaning that forcing the attached flame at the studied amplitudes or changing the pilot fuel mass flow rate inside the same range of values for the attached flame did not trigger the flashback of the lifted flame. This study highlights the role of the pilot injector and of flow modulations on the motions of the central portion of the flame and its stabilisation mechanism.

In a separate family of studies on gaseous staged combustion, Han *et al.* (2018) and Han *et al.* (2019) demonstrate that different flame shapes can be achieved by varying the stratification ratio or the global equivalence ratio. However, the flow field is not significantly impacted by the changes in flame shape. Moreover, vortex breakdown mode

https://doi.org/10.1017/jfm.2025.10937 Published online by Cambridge University Press

changes are neither discussed nor seem to be linked with the flame shape changes, except in very extreme conditions where some of the swirler passages are closed, but these flow fields are not representative of real operation.

Finally, the BIMER combustor family of works brings the flame transition studies closer to aeronautical applications by introducing liquid fuel. Providakis (2013) characterised the impact of the staging factor α (ratio of fuel injected by the pilot injector, over the total fuel injected, as defined in figure 2) on the flame shape, while also studying the two-phase flow combustion physics – spray atomisation, droplet evaporation and fuel mixing. Providakis (2013) observed a stable V flame from a pilot-only condition ($\alpha = 100\,\%$) down to $\alpha = 60\,\%$ (similar to figure 2*d*, so a CVB/S-ISL/L-OSL flame). Further decreasing the staging factor, Providakis (2013) observed the development of a strong thermoacoustic instability at around $\alpha = 40\,\%$ with high levels of sound pressure level (SPL). This led to an unstable behaviour of the flame, which no longer presented a V shape, sometimes seeming to switch to a tulip shape (similar to figure 2*c*, so a BVB/S-ISL/A-OSL flame). Even further reducing the staging factor to $\alpha = 20\,\%$, the flame bifurcates and stabilises in an M shape (similar to figure 2*e*, so a BVB/L-BLE/A-OSL flame), increasing the SPL in the chamber. When the staging factor was re-increased from $\alpha = 20\,\%$ to $\alpha = 60\,\%$, the flame retained its M shape instead of reverting to the original V shape. Thus, one of the main findings of Providakis (2013) was to identify this bi-stable behaviour of the burner and also the conditions under which bi-stability was observed. However, no discussion was made concerning vortex breakdown modes or correlations between vortex breakdown mode changes and flame shape changes. Additionally, Providakis (2013) created a database for validating numerical models of the BIMER combustor, with flow velocity and droplet diameter distributions available for various conditions.

Following the experimental works of Providakis (2013), LES using an Euler–Euler approach to model the disperse liquid phase have been performed by Cheneau *et al.* (2019*a*). Cheneau *et al.* (2019*a*) started his numerical cycle with the ignition of the chamber at $\alpha = 100\,\%$ (air mass flow rate $\dot{m}_{air} = 53\,\mathrm{g\,s^{-1}}$ and global equivalence ratio of $\phi = 0.6$), resulting in a tulip flame (similar to figure 2*a*, so a BVB/S-ISL flame). When changing to $\alpha = 60\,\%$ to compare the numerical flame with the experimental one, the changing in the spatial distribution of fuel triggers a slow modification of the flame and flow: the flame moves upstream and widens passing from a tulip to a V flame after ≈ 80 ms (similar to figure 2*d*, so a CVB/S-ISL/L-OSL flame). Two paths are then followed after this bifurcation: either the staging factor can be re-increased to $\alpha = 100\,\%$, where the flame keeps its V shape, or the staging factor can be further decreased, following the procedure of Providakis (2013). When the staging factor is further decreased, Cheneau *et al.* (2019*a*) showed that the numerical simulations were not able to capture the strong thermoacoustic instability observed by Providakis (2013) around $\alpha = 40\,\%$ and, thus, the flame kept its V shape throughout the whole path until $\alpha = 0\,\%$. However, after approximately 100 ms, a perturbation suddenly led to the V flame transitioning to an M flame (similar to figure 2*e*, so a BVB/L-BLE/A-OSL flame). From the M flame obtained at $\alpha = 0\,\%$, the staging factor is then re-increased up to $\alpha = 100\,\%$, showing that once the flame stabilises in an M-shape, it is no longer able to switch shapes. With this thorough study, Cheneau *et al.* (2019*a*) was able to map all possible flame shapes as a function of the staging factor and also demonstrated that the $\alpha = 100\,\%$ case is a multi-stable point, where the three flames are possible and stable. Cheneau *et al.* (2019*a*) also performed a thorough validation of the LES against the experimental data, showing a good match of velocity profiles and of flame shapes. However, no discussion was held concerning vortex breakdown modes, their relationship with flame shapes, or the mechanisms driving the transitions.

https://doi.org/10.1017/jfm.2025.10937 Published online by Cambridge University Press

The most recent experimental and numerical coupled studies on the BIMER combustor were conducted by Renaud (2015) and Mesquita (2021), respectively. Renaud (2015) concentrated on further characterising the liquid-phase behaviour of each injection stage, the combustor stability and the flame shapes by varying the staging factor from $\alpha = 100\,\%$ to $\alpha = 0\,\%$ and modulating the flow with a siren. Moreover, the air mass flow rate and total power were reduced (respectively to $\dot{m}_{air} = [32, 43]\ \mathrm{g\,s^{-1}}$ and $Power = [45, 73]$ kW) to allow the closure of the hysteresis cycle first observed by Providakis (2013). The first part of Renaud (2015) study was dedicated to the complete characterisation of the liquid phase in terms of diameter and velocity distributions (through PIV and Phase Doppler Anemometry measurements). He first analysed the pilot-only case ($\alpha = 100\,\%$), to characterise the pilot spray, and then a Lean Premixed Prevaporised (LPP) representative point ($\alpha = 15\,\%$), to characterise the spatial distribution of fuel in a case dominated by multipoint injection. These were then studied numerically in Mesquita, Vié & Ducruix (2018), where a numerical model was developed to match the spray injection. Renaud (2015) moved, then, to reacting cases, igniting the flame with a pilot-only injection ($\alpha = 100\,\%$), obtaining a V flame (figure 2*b*, so CVB/S-ISL flame). The influence of the ignition procedure and operating conditions was then studied numerically in Mesquita *et al.* (2021*b*), where it was shown that the flame shape after ignition can have a V, an M (figure 2*g*, so a BVB/L-BLE/A-OSL flame) or a tulip (figure 2*a*, so a BVB/S-ISL flame) shape depending on how the flame is ignited. Mesquita *et al.* (2021*b*) also showed that the M and tulip flames retain the non-reacting flow field and BVB mode topology, while the V flame changes the vortex breakdown mode to a CVB. Renaud (2015) then reduced the staging factor to $\alpha = 15\,\%$, where the stable V flame (figure 2*d*, so a CVB/S-ISL/L-OSL flame) was studied in these mostly premixed conditions, and then to $\alpha = 0\,\%$ (figure 2*f* CVB/L-ISL/A-OSL flame), where, after the development of a thermoacoustic instability, the flame transitioned from a V shape to an M one (similar to figure 2*e*, so a BVB/L-BLE/A-OSL flame). This transition was studied numerically by Mesquita *et al.* (2021*a*), who demonstrated that the thermoacoustic instability triggers an intricate vortex collective interaction phenomenon that destabilises the flow field and causes the vortex breakdown mode to transition from CVB to BVB, resulting in a change in the flame shape as a consequence. Renaud *et al.* (2017) showed that this V-to-M transition could also be triggered by forcing the $\alpha = 15\,\%$ V flame with a siren. From the M flame at $\alpha = 0\,\%$, the staging factor was progressively increased and around $\alpha = 20\,\%$, Renaud *et al.* (2015*b*) observed a flashback of the M flame, where its central portion moved upstream and reattached at the spray in a tulip shape (similar to figure 2*c*). In a numerical study, Mesquita *et al.* (2023*a*) detailed the mechanism by which the combustion chamber temperature, the thermoacoustic cycle and the change in staging factor all contribute to causing the M flame to flashback to a tulip flame. Renaud (2015) showed that, in the conditions just after the transition, this tulip flame proved to be metastable, and after some milliseconds, it transitioned again to a V shape, closing the hysteresis cycle. With this comprehensive screening of the staging factor, Renaud (2015) characterised the V, M and tulip flames under different operating conditions. These were carefully studied numerically in Mesquita *et al.* (2023*b*), showing the effect of the staging factor on each flame shape, the CVB stabilisation mechanisms for the V flame and the BVB one for both M and tulip flames.

As shown in the literature review above, works from different groups suggest that the vortex breakdown mode changes simultaneously with flame shape transitions, even if this is not explicitly discussed by the authors. Furthermore, if we infer from the presented literature that BVB to CVB mode changes are indeed happening simultaneously with the flame shape transitions, results of Chterev *et al.* (2014), Malbois *et al.* (2017), Taamallah

https://doi.org/10.1017/jfm.2025.10937 Published online by Cambridge University Press

Authors	Transition trigger	Flame shape transition
Chterev *et al.* (2014)	Increase in flame reactivity via equivalence ratio increase	BVB/L-BLE → BVB/L-BLE/A-OSL BVB/L-BLE/A-OSL → CVB/A-ISL/A-OSL
Malbois *et al.* (2017)	Increase in flame reactivity via equivalence ratio increase	BVB/S-ISL → CVB/S-ISL
Taamallah *et al.* (2019)	Increase in flame reactivity via equivalence ratio increase	BVB/L-BLE → CVB/A-ISL CVB/A-ISL → CVB/A-ISL/A-OSL
Cheneau *et al.* (2019*a*)	Increase in flame reactivity via fuel stratification change	BVB/S-ISL → CVB/S-ISL/L-OSL
Providakis (2013)	Decrease in flame reactivity via fuel stratification change	CVB/S-ISL/L-OSL → BVB/S-ISL/A-OSL BVB/S-ISL/A-OSL → BVB/L-BLE/A-OSL
Terhaar *et al.* (2014)	Decrease in flame reactivity via fuel steam dilution increase	CVB/A-ISL/A-OSL → CVB/L-ISL/L-OSL CVB/L-ISL/L-OSL → BVB/L-ISL/L-OSL BVB/L-ISL/L-OSL → BVB/L-BLE/L-OSL
Hermeth *et al.* (2014)	Decrease in flame reactivity via fuel stratification change	CVB/A-ISL/A-OSL → BVB/L-BLE/A-OSL
Cheneau *et al.* (2019*a*)	Decrease in flame reactivity via fuel stratification change	CVB/S-ISL/L-OSL → BVB/L-BLE/A-OSL
Hermeth *et al.* (2014)	Flow modulation via external forcing	BVB/L-BLE/A-OSL → CVB/A-ISL/A-OSL
Renaud *et al.* (2017)	Flow modulation via external forcing	CVB/S-ISL/L-OSL → BVB/L-BLE/A-OSL
Mesquita *et al.* (2021*a*)	Flow modulation via thermoacoustic instability	CVB/L-ISL/A-OSL → BVB/L-BLE/A-OSL

Table 2. Summary of the literature review on flame shape transitions likely occurring simultaneously with transitions in vortex breakdown mode.

et al. (2019) and Cheneau *et al.* (2019*a*) suggest that an increase in the flame reactivity drives BVB to CVB transitions, results of Providakis (2013), Terhaar *et al.* (2014), Hermeth *et al.* (2014) and Cheneau *et al.* (2019*a*) suggest that a decrease in the flame reactivity drives CVB to BVB transitions, and results of Hermeth *et al.* (2014), Renaud *et al.* (2017) and those of Mesquita *et al.* (2021*a*) demonstrate flow modulations triggering vortex breakdown mode transitions. All these triggering mechanism and transitions are summarised in table 2. These results, in particular those suggesting a BVB to CVB transition with increasing equivalence ratio, provide quite a relevant context for this work, which demonstrates that the BVB transitions to a CVB simultaneously with the tulip flame's transition to a V-shaped flame as the equivalence ratio is increased. Therefore, not only do we show that the equivalence ratio is a clear trigger for this transition, but also that it is more appropriately identified as a BVB/S-ISL to CVB/S-ISL flow–flame transition rather than a simple change in flame shape.

3. The BIMER combustor

The BIMER combustor was designed to study the operation of a lean-burn injector that uses a swirling flow to stabilise the flame. Moreover, a two-stage fuel injection system is employed to adapt the combustion regime according to the operational requirements. For example, the central pressure-swirl pilot stage can stabilise a non-premixed flame for ignition and situations where more stability is required, while the main stage is designed to produce a premixed flame, increasing efficiency and reducing pollutant emissions during

https://doi.org/10.1017/jfm.2025.10937 Published online by Cambridge University Press

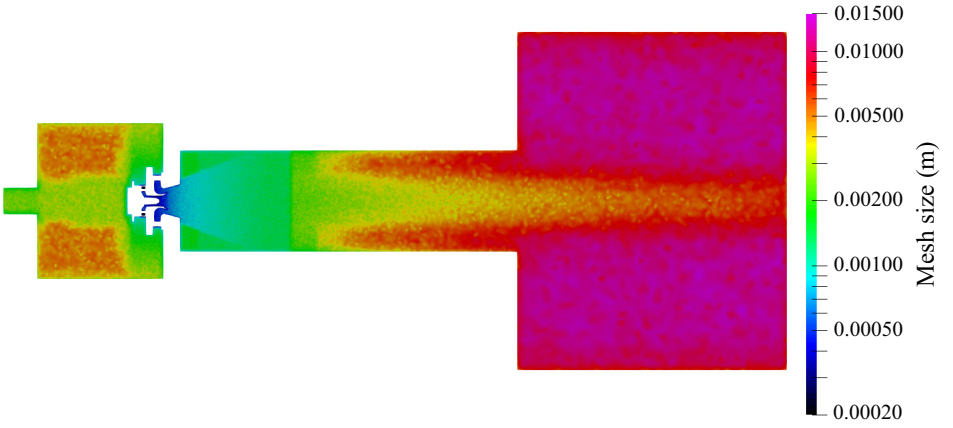


Figure 3. Transverse cut at the central plane of the BIMER combustor showing the cylindrical plenum, injector, combustor chamber and exit to the atmosphere. Flow from left to right and coloured by mesh size in log scale.

most of the operation. This intrinsic dynamic operation of the injector requires a careful examination of the flame's stability and how changes in the injection regime impact this stability. The injection regime can be characterised by: i) the proportion of fuel that goes through each stage, called the staging factor α defined as the ratio of fuel mass flow rate through the pilot stage and the total fuel mass flow rate, in percentage; and ii) by the equivalence ratio ϕ, defined as the ratio of fuel and air mass flow rates over the stoichiometric fuel/air ratio. There are various works on the BIMER combustor that study the effect of the staging factor on the stability of the burner (i.e. Renaud *et al.* 2015*b*; Mesquita *et al.* 2021*b*, 2023*a*), but, in this work, we focus on how the equivalence ratio affects the flame and therefore only the pilot injector is used and the staging factor is constant at $\alpha = 100\,\%$.

The rig (figure 3) comprises a cylindrical plenum and a rectangular combustion chamber ($500 \times 150 \times 150\,\text{mm}^3$). Three of the combustion chamber walls are water cooled (entrance, top and bottom), with two quartz windows on the sides to allow optical access. The injector has two swirling stages (figure 4): the first is the pilot stage at the centre, including a pressurised nozzle to create a hollow cone fuel spray with a half angle of 30°. The pilot stage swirler, where 15 % of the total air mass flow rate flows through, has a geometric swirl number of 0.6. The second stage is the outer and main one, referred to as the multi-point stage. Its injection system uses 10 holes of 0.3 mm diameter placed at the swirler vanes' exits to create a jet in cross-flow injection and improve mixing. This stage swirler is characterised by a geometric swirl number of 1, and 85 % of the air mass flow rate goes through it.

4. Large-eddy simulations of compressible reacting flows

The LES is performed using the AVBP code, co-developed by CERFACS and IFPEN (Wolf *et al.* 2012). The Navier–Stokes multi-species equations for LES of a two-phase flow with the Favre-averaging method ($\tilde{\cdot}$ superscript) are the following (Poinsot & Veynante 2012):

$$\frac{\partial \bar{\rho}}{\partial t} + \frac{\partial \bar{\rho}\tilde{u}_j}{\partial x_j} = \bar{\dot{s}}^{l\to g}_{mass}, \tag{4.1}$$

https://doi.org/10.1017/jfm.2025.10937 Published online by Cambridge University Press

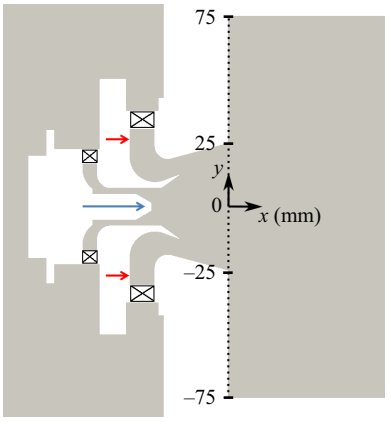


Figure 4. Two-dimensional view of the injector at the entrance of the combustion chamber. The central blue arrow indicates the pilot injector, while the two external red arrows show the radial position of multi-point injection holes. Flow from left to right.

$$\frac{\partial \bar{\rho}\tilde{u}_i}{\partial t} + \frac{\partial}{\partial x_j}(\bar{\rho}\tilde{u}_i\tilde{u}_j) = -\frac{\partial}{\partial x_j}\left(\bar{P}\delta_{ij} - \bar{\tau}_{ij} - \tau_{ij}^{sgs}\right) + \bar{\dot{s}}_{mo,i}^{l\to g}, \tag{4.2}$$

$$\frac{\partial \bar{\rho}\tilde{E}}{\partial t} + \frac{\partial}{\partial x_j}(\bar{\rho}\tilde{E}\tilde{u}_j) = -\frac{\partial}{\partial x_j}\left[\tilde{u}_i(\bar{P}\delta_{ij} - \bar{\tau}_{ij}) + \bar{q}_j + q_j^{sgs}\right] + \bar{\dot{\omega}}_T + \bar{\dot{s}}_{en}^{l\to g}, \tag{4.3}$$

$$\frac{\partial \bar{\rho}\tilde{Y}_k}{\partial t} + \frac{\partial}{\partial x_j}(\bar{\rho}\tilde{Y}_k\tilde{u}_j) = -\frac{\partial}{\partial x_j}\left(\bar{J}_{j,k} + J_{j,k}^{sgs}\right) + \bar{\dot{\omega}}_k + \bar{\dot{s}}_{sp_k}^{l\to g}, \tag{4.4}$$

where ρ is the gaseous density, u_i the ith-component of the velocity vector, P the pressure, Y_k the mass fraction of the kth-species, $\dot{\omega}_k$ the species chemical source, E the energy per unit mass (sum of the sensible energy e_s per mass and the kinetic energy per mass, $(u_i^2/2)$. The source terms $\dot{s}_{mass}^{l\to g}$, $\dot{s}_{mo,i}^{l\to g}$, $\dot{s}_{en}^{l\to g}$, $\dot{s}_{sp,k}^{l\to g}$ represent the coupling between the gas phase and a liquid phase. As this work considers a liquid fuel, only the fuel will have a source term $s_{fuel}^{l\to g}$ for the evaporation of the droplets. The filtered viscous stress tensor $\bar{\tau}_{ij}$, the filtered diffusion fluxes for species $\bar{J}_{k,i}$ and for energy $\bar{q}_i$ and the pressure–velocity product term $\bar{Pu}_i$ must be modelled. The superscript sgs refers to sub-grid scale terms.

The viscous tensor $\bar{\tau}_{ij}$ is approximated as

$$\bar{\tau}_{ij} = \overline{\mu\left(\frac{\partial u_i}{\partial x_j} + \frac{\partial u_j}{\partial x_i}\right) - \frac{2}{3}\mu\frac{\partial u_k}{\partial x_k}\delta_{ij}} \approx \bar{\mu}\left(\frac{\partial \tilde{u}_i}{\partial x_j} + \frac{\partial \tilde{u}_j}{\partial x_i}\right) - \frac{2}{3}\bar{\mu}\frac{\partial \tilde{u}_k}{\partial x_k}\delta_{ij}. \tag{4.5}$$

where μ is the dynamic viscosity and δ_{ij} is the Kronecker delta. The diffusive species flux vector is considered as

$$\bar{J}_{k,i} = \overline{\rho Y_k V_{k,i}} \approx -\bar{\rho}\left[\bar{D}_k\frac{W_k}{W}\frac{\partial \tilde{X}_k}{\partial x_i} - \tilde{Y}_k\tilde{V}_i^c\right]. \tag{4.6}$$

where D_k is the diffusion coefficient of species k into the rest of the mixture, W_k is the molecular weight of species k, W is the mean molecular weight of the mixture, X_k is the molar fraction of species k and V_c is the correction velocity. The filtered heat flux is considered as

https://doi.org/10.1017/jfm.2025.10937 Published online by Cambridge University Press

$$\bar{q}_i = -\lambda \frac{\partial T}{\partial x_i} + \sum_{k=1}^{\bar{N}} J_{k,i} h_{s,k} \approx -\bar{\lambda} \frac{\partial \tilde{T}}{\partial x_i} + \sum_{k=1}^{N} \bar{J}_{k,i} \tilde{h}_{s,k}. \tag{4.7}$$

where λ is the thermal conductivity and $h_{s,k}$ is the sensible enthalpy of species k. The sub-grid terms, identified as $\cdot^{sgs}$, are

$$\tau_{ij}^{sgs} = -\bar{\rho}(\widetilde{u_i u_j} - \tilde{u}_i \tilde{u}_j), \tag{4.8}$$

$$q_i^{sgs} = \bar{\rho}(\widetilde{E u_i} - \tilde{E}\tilde{u}_i), \tag{4.9}$$

$$J_{k,i}^{sgs} = \bar{\rho}(\widetilde{Y_k u_i} - \tilde{Y}_k \tilde{u}_i). \tag{4.10}$$

These unresolved variables require closure models. The following sections are then dedicated to detailing the choice of the needed models and to presenting the governing equations.

4.1. *Sub-grid closure models for LES*

The sub-grid terms represent the motion of the fluid for the turbulent scales that are filtered and, therefore, not resolved on the LES grid. Normally, the resolved LES scales comprise the majority of the turbulence spectrum, and the modelled sub-grid scales can be assumed to be statistically homogeneous, isotropic and responsible for the viscous dissipation of energy, which simplifies their modelling.

For this work, we model the sub-grid scales with the functional wall-adapting local eddy viscosity (Nicoud & Ducros 1999). It was developed to reproduce the asymptotic behaviour of the turbulent viscosity in function of $(y^+)^3$ near the wall. It does not need any modelling of the boundary layer, nor any turbulent wall law. Thus, the turbulent viscosity is defined as

$$\nu_t = C_W^2 \bar{\Delta}^2 \frac{(s_{ij}^d s_{ij}^d)^{3/2}}{(\tilde{S}_{ij}\tilde{S}_{ij})^{5/2} + (s_{ij}^d s_{ij}^d)^{5/4}}, \tag{4.11}$$

with s_{ij}^d the traceless symmetrical part of the square of the velocity gradient tensor

$$s_{ij}^d = \frac{1}{2}(\tilde{g}_{ij}^2 + \tilde{g}_{ji}^2) - \frac{1}{3}\tilde{g}_{kk}^2 \delta_{ij}, \tag{4.12}$$

where $\bar{\Delta}$ is the characteristic size of the LES filter and $\tilde{g}_{ij} = \partial \tilde{u}_j / \partial x_i$ the gradient of the resolved velocity. Thanks to numerical simulations of the isotropic homogeneous turbulence, the constant C_W has been estimated as 0.5 by (Nicoud & Ducros 1999).

The sub-grid terms of (4.2), (4.3) and (4.4) are approximated here as follows (Boileau 2007):

$$\tau_{ij}^{sgs} = \bar{\rho}(\widetilde{u_i u_j} - \tilde{u}_i \tilde{u}_j) \approx 2\bar{\rho}\nu_t \left(\frac{\partial \tilde{u}_i}{\partial x_j} + \frac{\partial \tilde{u}_j}{\partial x_i} \right) - \frac{2}{3}\bar{\rho}\nu_t \frac{\partial \tilde{u}_k}{\partial x_k}\delta_{ij}, \tag{4.13}$$

$$J_{i,k}^{sgs} = -\bar{\rho}(\widetilde{u_j Y_k} - \tilde{u}_j \tilde{Y}_k) \approx -\bar{\rho} \left(D_t \frac{W_k}{W} \frac{\partial \tilde{X}_k}{\partial x_i} - \tilde{Y}_k \tilde{V}_j^c \right), \tag{4.14}$$

$$q_i^{sgs} = -\bar{\rho} \left(\widetilde{u_j E} - \tilde{u}_j \tilde{E} \right) \approx -\lambda_t \frac{\partial \tilde{T}}{\partial x_i} + \sum_{k=1}^{N} J_{i,k}^{sgs} \tilde{h}_{s,k}, \tag{4.15}$$

https://doi.org/10.1017/jfm.2025.10937 Published online by Cambridge University Press

with ν_t the sub-grid scale turbulent viscosity, $D_t = \nu_t / Sc_t$ the turbulent molecular diffusion coefficient and $\lambda_t = \bar{\rho}\nu_t \bar{C}_p Pr_t$ the turbulent thermal diffusion coefficient. Also, Sc_t and Pr_t are respectively the turbulent Schmidt and Prandtl numbers.

4.2. *Two-phase flow modelling: Lagrangian discrete particle simulation approach*

One of the key points to correctly capture the governing phenomena in two-phase combustion is the numerical modelling of the liquid phase. As liquid fuel is injected to feed the combustion process, accurately representing the liquid phase and simulating the two-phase flow dynamics are essential for accurate predictions. The liquid fuel is injected at high pressure, and the liquid sheet is destabilised, disintegrating into filaments until it is broken down to form a mist of droplets with diameters of the order of 1 to 100 μm, which evaporate to feed the flame in gaseous fuel. Excepting the region near the liquid injection, where primary atomisation, coalescence and secondary atomisation take place, the majority of the flow in aeronautical combustion chambers is located in the diluted suspension region, where the mist of droplets is located.

Since resolving numerically primary atomisation is currently still out of reach for various reasons in the case of spray combustion simulations (Fiorina *et al.* 2016), a spray of droplets is commonly used to model the injection. Considering the context and application of this work, we rely on the Lagrangian point-particle strategy to model the liquid phase. In particular, a deterministic discrete particle simulation (DPS) is employed, where each numerical particle corresponds to a single physical particle. Thus, the fuel droplets are considered as point particles that are also local source terms for the gas under the following hypotheses:

(i) The spray can be considered as diluted, meaning that the volume occupied by the liquid and the collisions between the droplets are negligible. Moreover, the interactions between neighbouring droplets without contact are sufficiently small to also be neglected.
(ii) The droplets are spherical as a consequence of their small size. Indeed, for the small droplets, the surface tension forces are preponderant compared with other exterior forces that may modify the droplet shape. Thus, the equilibrium shape for the droplet is a sphere.

Therefore, with these hypotheses, a single droplet can be considered as a discrete point in space that is affected by the surrounding conditions, which will be evaluated at the particle's position (often indexed by $f@p$, meaning fluid at the particle's position). The evolution of a particle's state can be individually traced using the equations of motion that will be further discussed. The coupling with the gas phase is done through source terms of mass, momentum and energy (already presented in (4.1), (4.2), (4.3) and (4.4)). For this work, a two-way coupling is considered, where the liquid-phase influence over the gas phase ($l \rightarrow g$) and the gas-phase influence over the liquid phase ($g \rightarrow l$) are both modelled. However, this choice of modelling implies the need for another hypothesis: the considered particle perturbations to the flow field at $f@p$ are negligible compared with the perturbations caused by the other surrounding droplets to the flow field. This hypothesis is needed to consider that the flow at $f@p$, modelled as the far-field environment for the macroscopic models, is not altered by the analysed particle. The error introduced by this hypothesis is studied by Sirignano (2010).

In the Lagrangian DPS approach, the trajectory, the equations of mass, momentum and energy conservation are solved for each droplet individually with the following set of equations:

https://doi.org/10.1017/jfm.2025.10937 Published online by Cambridge University Press

$$\frac{\mathrm{d}X_{p,i}(t)}{\mathrm{d}t} = u_{p,i}, \tag{4.16}$$

$$\frac{\mathrm{d}m_p(t)}{\mathrm{d}t} = \dot{m}_p, \tag{4.17}$$

$$\frac{dm_p u_{p,i}(t)}{\mathrm{d}t} = F^{ext}_{i,p}, \tag{4.18}$$

$$\frac{\mathrm{d}m_p h_{s,p}(t)}{Dt} = \dot{\Phi}_p. \tag{4.19}$$

With the index p representing the particle, i the corresponding spatial coordinate, X the position, m the mass, $F^{ext}_{i,p}$ represent the external forces acting on the droplet, $\dot{m}_p$ is the mass variation and $\dot{\Phi}_p$ is the droplet's internal energy variation.

The coupling with the gas phase is done through the conservative transfer of the mass flux, momentum and energy flux of each droplet n to the gaseous LES equations by means of the source terms $s^{l\to g}$

$$s^{l\to g}_m = \frac{1}{\Delta V}\sum_{n=1}^{N} \Psi_n(x_{p,n})\dot{m}_{p,n}, \tag{4.20}$$

$$s^{l\to g}_{mo,i} = \frac{1}{\Delta V}\sum_{n=1}^{N} \Psi_n(x_{p,n})(-m_{m,p}F^{ext}_{i,p,n} + \dot{m}_{p,n}u_{p,n,i}), \tag{4.21}$$

$$s^{l\to g}_{en,i} = \frac{1}{\Delta V}\sum_{n=1}^{N} \Psi_n(x_{p,n})\left(-m_{p,n}\boldsymbol{F}_{p,n}\cdot\boldsymbol{u}_{p,n} + \frac{1}{2}\dot{m}_{p,n}\left\|\boldsymbol{u}_{p,n}\right\|^2 - \dot{\Phi}_{p,m}\right), \tag{4.22}$$

$$s^{l\to g}_{fuel} = \frac{1}{\Delta V}\sum_{n=1}^{N} \Psi_n(x_{p,n})\dot{m}_{p,n}. \tag{4.23}$$

Where the index *fuel* on the source term $s^{l\to g}_{fuel}$ for the conservation of species equation indicates that only the fuel species will have a source term coming from the evaporation of the droplets. Here, ΔV is the control volume of the flux transfer (generally, the nodal volume, i.e. the fictive volume around a node), N the number of particles inside that volume and $\Psi_n(x_p)$ an interpolation function depending on the mesh. For unstructured meshes, the interpolation is done by weighting the inverse of the particle's distance to the considered node (d_j) with the sum of the inverse of the distances of the particle to each node of the cell containing the particle (d_l)

$$\Psi_{n,j}(x_p) = \frac{\dfrac{1}{d_j}}{\sum_{l=1}^{N_v}\dfrac{1}{d_l}}, \tag{4.24}$$

where j is the index for the nodes of the containing cell and N_v is the number of nodes in the cell.

The Lagrangian DPS approach enables modelling the spray as if it were composed of a group of isolated droplets, allowing for the subsequent analysis of the spray as the collective behaviour of these isolated droplets. The necessary closure models are then presented in the following sections.

https://doi.org/10.1017/jfm.2025.10937 Published online by Cambridge University Press

4.3. *External forces acting on an isolated droplet*

The study of the dynamics of an evaporating droplet often neglects the effects of evaporation on the drag forces, considering only the motion of a non-evaporating rigid sphere in a flow. This reasonable hypothesis simplifies the modelling, and the forces acting on the surface of the rigid, spherical droplet can be divided into steady and unsteady forces.

The resulting total force ($F_{i,p}^{ext}$) from (4.18) for this work finally considers the drag (the particle's weight is neglected, as in this application is much inferior to the other forces)

$$F_{i,p} = \frac{1}{\tau_p}(u_{f@p} - u_{p,i}), \tag{4.25}$$

and the characteristic time τ_p with the Schiller & Naumann (1935) correction is defined as

$$\tau_p = \frac{\rho_l d_p^2}{18\mu_g f(Re_p)} \quad \text{with } f(Re_p) = \left(1 + 0.15Re_p^{0.687}\right). \tag{4.26}$$

4.4. *Evaporation source terms*

The evaporation model used in this work is the one developed by Abramzon & Sirignano (1989). The authors proposed to modify the Sherwood and Nusselt numbers to consider the effect of the convective boundary layer on the evaporation model, by introducing two correction factors F_M and F_T that are defined as

$$F_M = (1 + B_M)^{0.7}\frac{\ln(1 + B_M)}{B_M}, \tag{4.27}$$

$$F_T = (1 + B_T)^{0.7}\frac{\ln(1 + B_T)}{B_T}, \tag{4.28}$$

where B_M and B_T are Spalding mass and heat transfer numbers, respectively. The corrected Sherwood and Nusselt numbers are then

$$Sh^* = 2 + \frac{(Sh - 2)}{F_M}, \tag{4.29}$$

$$Nu^* = 2 + \frac{(Nu - 2)}{F_T}, \tag{4.30}$$

where Sh is the Sherwood number and Nu the Nusselt number. This model allows for a significant improvement in the numerical representation of droplet evaporation. The final equations for the droplet mass flux $\dot{m}_p$, gaseous conductive flux Φ_g^{cd} and droplet enthalpy flux Φ_p are then

$$\dot{m}_p = -Sh^*\pi d_p[\rho D_F]\ln(B_M + 1), \tag{4.31}$$

$$\Phi_g^{cd} = Nu^*\pi d_p\frac{\lambda}{C_P}(C_P(T_\zeta)T_\zeta - C_P(T_\infty)T_\infty)\frac{\ln(B_T + 1)}{B_T}, \tag{4.32}$$

$$\Phi_p = \frac{d}{\mathrm{d}t}(m_p h_{s,l}(T_p)) = -\Phi_g^{cv} - \Phi_g^{cd}, \tag{4.33}$$

where d_p is the droplet diameter, D_F is the fuel's diffusivity, λ is the thermal diffusivity, C_P is the constant pressure heat capacity of the mixture, T_ζ is the temperature at the surface of the droplet, T_∞ is the far-field temperature, Φ_g^{cd} and Φ_g^{cv} are respectively the gaseous conductive and the convective fluxes and $h_{s,l}$ is the sensible enthalpy of the droplet.

https://doi.org/10.1017/jfm.2025.10937 Published online by Cambridge University Press

4.4.1. *Modelling of fuel injection*

After the discussion on the modelling of the liquid-phase behaviour, the way in which these droplets are inserted in the numerical domain (i.e. their boundary conditions) must be discussed. This is done through the numerical modelling of the injection systems present, in the case of this work, in aeronautical combustion chambers. The BIMER combustor has two injection systems that must be separately modelled: the pilot pressure-swirl nozzle and the multipoint injection. The modelling strategies employed to model each of these systems are described in this section.

4.5. *Modelling the pilot spray: the fuel injection model by upstream reconstruction (FIMUR) for pressure-swirl atomisers*

The internal geometry of a typical pressure-swirl simplex atomiser, representative of the BIMER pilot injector. The liquid enters the atomiser through a tube perpendicular to the profile cross-section, generating a swirling motion of the liquid inside the atomiser cavity. The fuel is centrifuged to the walls of the atomiser, while the swirling movement causes the entrainment in a cylindrical region of radius R_a at the axis of rotation inside the injector. The discharge channel leads to an orifice of radius R_0, from where fuel is then injected inside the chamber. The angle formed by the axis of rotation and the droplets is called the spray half-angle and defined as θ_S. This angle is mostly a function of the injector geometry and of the size of the injection hole, while the droplet size depends mostly on the thickness of the liquid sheet inside the atomiser (affected by the fuel characteristics), the fluid velocity (controlled by the injection pressure) and interaction with the surrounding air (Rizk & Lefebvre 1983).

Using the assumption of a frictionless flow inside the atomiser and knowing the spray angle θ_S, it is possible to use empirical relationships to determine the contraction factor at the discharge orifice X (Rizk & Lefebvre 1985)

$$X = \frac{R_a^2}{R_0} = \frac{\sin^2\theta_S}{1+\cos^2\theta_S}. \tag{4.34}$$

Knowing the ratio X allows us to define the discharge coefficient C_D (Rizk & Lefebvre 1985)

$$C_D = 1.17\sqrt{\frac{(1-X)^3}{1+X}}. \tag{4.35}$$

The FIMUR (Sanjosé 2009) utilises these geometric parameters (R_a, R_0 and C_D), the fuel mass flow rate $\dot{m}_l$ and the spray characteristics (θ_S) to determine the velocity profiles of the injected droplets. The model defines $R_S^0 = (R_0 + R_a)/2$ and supposes that the axial velocity is constant at the plane $x = x_0$ and that, as a consequence of the swirling motion, the tangential velocity evolves linearly with the radius, having its maximum near the injector walls. A solid-body rotation is assumed for the liquid inside the atomiser cavity, which leads to a zero radial velocity. Finally, to determine the zone of particle injection, it is supposed that the liquid volume fraction is one between $[R_a, R_0]$ and zero at the central air entrainment zone. These assumptions lead to the following set of equations imposing the velocity profiles at the injector exit ($x = x_0$) and the region of injection:

$$u_{l,x}^0(\theta, r_0) = \frac{\dot{m}}{\rho_l \pi R_0^2 (1-X)}, \tag{4.36}$$

$$u_{l,r}^0(\theta, r_0) = 0, \tag{4.37}$$

https://doi.org/10.1017/jfm.2025.10937 Published online by Cambridge University Press

$$u^0_{l,\theta}(\theta, r_0) = \frac{\dot{m}}{\rho_l A_p}\frac{r_0}{R^0_S}, \tag{4.38}$$

$$\alpha^0_l(\theta, r_0) = \begin{cases} 0 \text{ if } r_0 \in [0,\ R_a], \\ 1 \text{ if } r_0 \in [R_a,\ R_0]. \end{cases} \tag{4.39}$$

Particles are injected from a ring with radii varying in the range $[R_a, R_0]$ and with an accordingly assigned velocity. The profiles resulting from these equations are illustrated in Sanjosé (2009).

Regarding the droplet diameter, the FIMUR does not utilise any correlation; instead, the user is responsible for inputting the distribution from which the diameter will be randomly sampled. This means in particular that the velocity and diameter attribution to a droplet are independent. The FIMUR has been validated and applied with success for various aeronautical applications (Sanjosé 2009; Sanjosé *et al.* 2011; Hannebique *et al.* 2013) and on the BIMER combustor (Cheneau 2019; Cheneau *et al.* 2019*a*,*b*; Mesquita *et al.* 2017, 2018, 2021*a*,*b*, 2023*a*,*b*). For the BIMER pilot spray, the injected droplet properties (i.e. velocity, diameter distribution) have been extracted from the experimental studies of Renaud *et al.* (2015*b*) and the injected Probability Density Functions (PDFs) correspond to the measurements. This injection set-up has been compared with the experiments and validated in the dedicated study of Mesquita *et al.* (2018). Due to the absence of measurements for different staging values, the diameter distribution is assumed to be constant, and the velocity is scaled according to the fuel mass flow rate.

4.6. *Modelling the multipoint injection*

The injection of fuel through the multipoint system is much simpler compared with the pilot pressure-swirl atomiser. In this system, fuel is injected through 10 equally spaced holes with only axial velocity, creating a jet-in-cross-flow that promotes atomisation. The numerical strategy is similar to this procedure: droplets are directly initialised over the surfaces of the injection holes, and the axial velocity is imposed directly from the fuel mass flow rate. This simple numerical modelling, despite ignoring some of the physics of jet-in-cross-flow atomisation, such as the column or surface breakups, has shown a satisfactory performance on the numerical simulations of the BIMER combustor by Cheneau *et al.* (2019*a*,*b*); Mesquita *et al.* (2017, 2018, 2021*a*,*b*, 2023*a*,*b*), but also in other similar applications (e.g. Jaegle 2009). Similarly to the pilot spray, the injected droplet properties (i.e. velocity, diameter distribution) for the multipoint injection have also been modelled from the experimental studies of Renaud *et al.* (2015*b*), after a detailed study and validation in Mesquita (2021). Thus, injected PDFs correspond to the measurements, with the diameter distribution considered constant for all staging values and the velocity is scaled according to the fuel mass flow rate.

4.6.1. *Modelling the droplet–wall interactions*

During the experimental campaign, a filming behaviour of fuel over the divergent wall was noticed by Renaud (2015). However, modelling fuel filming over walls reliably requires consideration of complex phenomena, and at the time this work began, an affordable, fully validated Lagrangian model for filming was not available to the authors. Therefore, a sliding condition for the droplets is used, where the droplets adhere to the wall and only move parallel to it, mimicking the filming behaviour. Cheneau *et al.* (2019*a*,*b*) and Mesquita *et al.* (2017, 2018, 2021*a*,*b*, 2023*a*,*b*) showed that this simple approximation was sufficient to approximate the fuel filming behaviour over the divergent cup of the burner.

https://doi.org/10.1017/jfm.2025.10937 Published online by Cambridge University Press

Additionally, an elastic rebound of the droplets is also employed when the droplets interact with hot walls.

4.7. *Chemistry modelling: the 2S_KERO_BFER reduced scheme*

The fuel used in this work is kerosene. The primary factor in selecting a chemical scheme for this work was the balance between computational cost and accuracy, as many operating points needed to be simulated, and the use of Lagrangian modelling for the liquid phase already implies a high computational cost. Cheneau *et al.* (2019*b*) and Mesquita *et al.* (2021*a*,*b*, 2023*a*,*b*) compared the simulations with the experiments and showed that modelling kerosene with the 2S_KERO_BFER reduced scheme developed by Franzelli *et al.* (2010) (assuming a unity Lewis number) produces good results for the LES of the BIMER combustor, validating its choice. Not only is the power of the burner well-captured numerically in all conditions and with all flame shapes, but dynamic phenomena, as ignition and flame shape transitions, are also well captured, as shown by Mesquita *et al.* (2021*a*,*b*, 2023*a*,*b*).

The kinetic scheme 2S_KERO_BFER is based on 6 species and 2 reactions, the oxidation of kerosene and the $CO - CO_2$ equilibrium

$$KERO + 10O_2 \rightarrow 10CO + 10H_2O, \tag{4.40}$$

$$CO + 0.5O_2 \leftrightarrow CO_2. \tag{4.41}$$

4.8. *Combustion modelling: thickened flame model for LES*

The thickened flame model for LES (TFLES) coupled with the 2S_KERO_BFER reduced chemistry is a combustion model that has already proven to produce accurate simulations in the context of turbulent two-phase multi-regime combustion (Shum-Kivan *et al.* 2017; Cheneau *et al.* 2019*b*; Mesquita *et al.* 2021*a*,*b*, 2023*a*,*b*).

The principle behind the thickened flame model, firstly proposed by Butler & O'Rourke (1977), is to divide the reaction rate and multiply the species and thermal diffusion by a factor $\mathcal{F}$, aiming to increase the flame thickness by the same factor $\mathcal{F}$, allowing it to be resolved on the LES mesh, and keeping unaltered the flame speed. Recalling that for a laminar premixed flame the flame thickness δ_L and the flame speed s_L are defined as (Kuo & Acharya 2012)

$$s_L \propto \sqrt{\dot{\omega}_T \mathcal{D}_{th}} \qquad \text{and} \qquad \delta_L \propto \frac{\mathcal{D}_{th}}{s_L} = \sqrt{\frac{\mathcal{D}_{th}}{\dot{\omega}_T}}, \tag{4.42}$$

where $\mathcal{D}_{th} = \lambda_{th}/\rho C_p$ is the thermal diffusivity and $\dot{\omega}_T$ is the HRR. The thickened quantities become then:

$$\bar{\dot{\omega}}_k = \frac{\dot{\omega}_k}{\mathcal{F}} \qquad \text{and} \qquad \bar{\dot{\omega}}_T = \frac{\dot{\omega}_T}{\mathcal{F}}, \tag{4.43}$$

$$\mathcal{D}_k \rightarrow \mathcal{F}\mathcal{D}_k \qquad \text{and} \qquad \mathcal{D}_{th} \rightarrow \mathcal{F}\mathcal{D}_{th}. \tag{4.44}$$

Leading to

$$\delta_L^{TF} = \mathcal{F}\sqrt{\frac{\mathcal{D}_{th}}{\dot{\omega}_T}}. \tag{4.45}$$

However, the artificial thickening of the flame modifies the flame–turbulence interactions, a modification that is visible through the consequent reduction by the same factor $\mathcal{F}$ of the Damkhöler number, which compares the characteristic time of turbulence

https://doi.org/10.1017/jfm.2025.10937 Published online by Cambridge University Press

		Thickening		Wrinkling	
Diffusivity:	$\mathcal{D}$	$\longrightarrow$	$\mathcal{F}\mathcal{D}$	$\longrightarrow$	$\mathcal{E}\mathcal{F}\mathcal{D}$
Reaction rate:	$\dot{\omega}$	$\longrightarrow$	$\dot{\omega}/\mathcal{F}$	$\longrightarrow$	$\mathcal{E}\dot{\omega}/\mathcal{F}$
Flame speed:	s_L	$\longrightarrow$	s_L	$\longrightarrow$	$\mathcal{E}s_L$
Flame thickness:	δ_L	$\longrightarrow$	$\mathcal{F}\delta_L$	$\longrightarrow$	$\mathcal{F}\delta_L$

Table 3. Summary of the TFLES model impact on combustion.

τ_t with the characteristic time for chemistry τ_c

$$Da = \frac{\tau_t}{\tau_c} = \frac{l_t s_L}{u'\delta_L} \longrightarrow Da^{TF} = \frac{l_t s_L}{u'\delta_L \mathcal{F}}. \tag{4.46}$$

The thickened flame is then less sensitive to turbulence and the wrinkling of the flame front is underestimated, thus reducing the flame surface and, consequently, the reactants consumption rate (Angelberger *et al.* 1998). For this reason, the effect of turbulence on the flame wrinkling was studied with DNS, and Colin *et al.* (2000) proposed an efficiency function $\mathcal{E}$ to account for the loss of wrinkling due to thickening and for the sub-grid flame wrinkling, aiming to improve the modelling of flame–turbulence interactions

$$\bar{\dot{\omega}}_k = \frac{\mathcal{E}\dot{\omega}_k}{\mathcal{F}} \qquad \text{and} \qquad \bar{\dot{\omega}}_T = \frac{\mathcal{E}\dot{\omega}_T}{\mathcal{F}}, \tag{4.47}$$

$$\mathcal{D}_k \rightarrow \mathcal{E}\mathcal{F}\mathcal{D}_k \qquad \text{and} \qquad \mathcal{D}_{th} \rightarrow \mathcal{E}\mathcal{F}\mathcal{D}_{th}. \tag{4.48}$$

The TFLES model is then summarised in table 3.

Many efficiency functions are available in the literature. The chosen efficiency function for this work is the one proposed by Charlette, Meneveau & Veynante (2002)

$$\mathcal{E} = \Xi\left(\frac{\Delta_e}{\delta_L^0}\right) = \left(1 + min\left[\frac{\Delta_e}{\delta_L^0}, \Gamma\frac{u'_{\Delta_e}}{s_L^0}\right]\right)^{\beta}, \tag{4.49}$$

with $\beta = 0.5$ a constant of the model, u'_{Δ_e} the sub-grid scale turbulent velocity and Γ the spectral efficiency function estimated in Charlette *et al.* (2002).

The thickened flame model was initially designed for premixed flames and must be modified to be applicable in partially premixed cases, as the thickening in the original model is applied uniformly, modifying the species and thermal diffusion even for the species mixing in the non-reacting zones and overestimating diffusion fluxes by the factor $\mathcal{F}$. Aiming to extend the flame thickening approach to non-premixed combustion, Legier, Poinsot & Veynante (2000) proposed a dynamic version of the model, where the thickening factor is only applied on the reacting zones. Thus, a flame sensor $\mathcal{S}$ was developed to identify the reaction zones and the thickening is only applied where the sensor is activated

$$\mathcal{S} = \tanh\left(\beta'\frac{\Omega}{\Omega_0}\right) \text{ with } \beta' = 50, \tag{4.50}$$

$$\Omega = Y_F^{\nu'_F} Y_O^{\nu'_O} \exp\left(-\Gamma_T\frac{E_a}{\mathcal{R}T}\right), \tag{4.51}$$

$$\mathcal{F} = 1 + (\mathcal{F}_{max} - 1)\mathcal{S}, \tag{4.52}$$

where Ω_0 is the maximum value of Ω in a one-dimensional laminar non-thickened flame, indices F and O correspond, respectively, to $Fuel$ and $Oxidant$ and Γ_T is the parameter used to activate the thickening function before the reaction, with a typical value of $\Gamma_T = 0.5$.

https://doi.org/10.1017/jfm.2025.10937 Published online by Cambridge University Press

It is common for simulations of complex geometries to encounter a wide range of mesh sizes. As a consequence, a single value for the filter size Δ_e will not be adapted, as the number of points to resolve the flame front will vary. To counter this practical issue, the maximum value of the thickening factor is weighted by the local mesh size Δ_x and by n, the user-defined number of points used to resolve the thickened flame front

$$\mathcal{F}_{max} = n\frac{\delta_L^0}{\Delta_x}. \tag{4.53}$$

Generally, $n = 5$ points are sufficient to correctly solve the flame front, a value adopted for the simulations performed in this work.

For numerical simulations of two-phase combustion, modelling the interactions between the liquid phase and the flame front is central, as the liquid spray reaches the reaction zone in most industrial applications. Thus, intense evaporation of fuel occurs, imposing a strong coupling between the evaporating liquid phase and the gaseous chemical reaction, with the evaporation potentially controlling the local reaction rate. Even if the TFLES model was developed for gaseous premixed flames only, modifications were introduced to account for liquid fuel combustion and to consider flame–liquid-phase interactions, thereby correctly representing the behaviour of the non-thickened flame front. In the BIMER combustor, despite being an LPP burner (and thus with an intended operation in lean-premixed regime), sometimes part of the flame burns in a non-premixed regime, as the liquid phase does not always pre-vaporise and premixes entirely before reacting. Nevertheless, these regions remain marginal when compared with the total flame, which burns in a premixed regime in the majority of cases considered in this work. Thus, even if using TFLES introduces an error when these non-premixed regions are present, this error has been shown to be marginal for the LES of the BIMER combustor and not to affect the combustion dynamics in several comparisons with experiments. Indeed, Cheneau *et al.* (2019*b*) and Mesquita *et al.* (2021*a*,*b*, 2023*a*,*b*) have shown that the use of TFLES coupled with 2S_KERO_BFER produced very good results for the BIMER combustor when compared with the experiments for pilot-only to multipoint-only operation, even in cases where the combustion was not completely premixed. Thus, this choice of modelling is kept in this work.

For a Lagrangian modelling of the liquid-phase, the approach used for the two-phase TFLES (TP-TFLES) is the one derived by Paulhiac (2015), who proposed an analysis of the thickened flame model as a modification of time (t) and space (x) through the thickening factor

$$x^{TFLES} \approx \frac{x}{\mathcal{F}}, \tag{4.54}$$

$$t^{TFLES} \approx \frac{t}{\mathcal{F}}. \tag{4.55}$$

Thus, to keep consistency, the same scale transformation must be applied to the liquid phase. This is achieved by applying the same scale transform as in (4.54) and (4.54) to the Lagrangian derivative ($(D/Dt) = (\partial/\partial t) + u_{p,i}(\partial/\partial x_i)$) and to the Lagrangian motion equations of particle p ((4.16), (4.18), (4.17), (4.19)), leading to the modification of the drag force, evaporation rate and heat transfer as the particles' characteristic time τ_p (4.26), mass variation $\dot{m}_p$ (4.31) and internal energy variation Φ_p (4.33) are modified by the thickening factor

$$\tau_p^{TFLES} = \mathcal{F}\tau_p, \tag{4.56}$$

$$\dot{m}_p^{TFLES} = \frac{\dot{m}_p}{\mathcal{F}}, \tag{4.57}$$

https://doi.org/10.1017/jfm.2025.10937 Published online by Cambridge University Press

$$\Phi_p^{TFLES} = \frac{\Phi_p}{\mathcal{F}}. \tag{4.58}$$

This implies that in the thickened space, the droplets evaporate $\mathcal{F}$ times slower and experience a drag force that is $\mathcal{F}$ times lower than the actual drag force. The calculations made by Paulhiac (2015) demonstrate that these modifications ensure the TP-TFLES modelling for Lagrangian particles accurately captures the non-thickened spray flame behaviour.

4.9. *Numerical set-up*

The LES is performed using the AVBP code, co-developed by CERFACS and IFPEN (Wolf *et al.* 2012), using a two-step Taylor–Galerkin (TTGC) numerical scheme (third order in space and time), along with the artificial diffusion implemented by Colin & Rudgyard (2000) to treat numerical perturbations and stiff gradients. The Navier–Stokes characteristic boundary conditions developed by Poinsot & Lele (1992) are used to impose the gaseous inlet and outlet boundary conditions. Walls are considered non-slipping and adiabatic, as no experimental measurements of the wall temperatures were available, except for the two water-cooled walls, which were treated as isothermal at 373 K, the measured exit temperature of the cooling water.

An unstructured tetrahedra mesh of 32 million elements is used (figure 3). This mesh is a result of several mesh convergence studies and improvements presented in Cheneau, Vié & Ducruix (2015), Cheneau (2019) and Mesquita (2021), which resulted in several successful validations against experimental data (e.g. gaseous velocity, liquid velocity and diameter, flame shape, flame dynamics, SPL), as shown in Cheneau *et al.* (2019*b*) and Mesquita *et al.* (2018, 2021*b*, 2023*a*,*b*). In the reaction region, the mesh keeps the flame thickening factor between 3 and 7.

5. Results

5.1. *Non-reacting flow, ignition and operating conditions*

The simulation is initiated from a non-reacting condition (OP_{lp} or OP_1) to ensure convergence of the flow field and liquid fuel, as described in Mesquita *et al.* (2018). Figure 5 characterises the aerodynamics of the non-reacting flow, showing that the flow topology is defined by a BVB mode: one can see the bubble-shaped CRZ and that it is in depression compared with the swirling flow. A PVC is also present (figure 5*e*). For all the studied operating conditions (Table 4), the flow topology is the same, presenting the same BVB mode and flow structures, with just a change in flow field magnitude (figure 5 and PVC frequency figure 5*f*).

The flow is ignited with a similar strategy to the experiments of Renaud (2015), as described in Mesquita *et al.* (2021*a*): at the operating point OP_1, a kernel is initialised in the CRZ, which, after propagation, leads to the stabilisation of a tulip flame (figure 2*a*). This tulip flame is then stabilised for 40 ms and studied, as shown in Mesquita *et al.* (2023*b*).

5.2. *Tulip and V stable flames: initial and final states*

Before discussing the transition, it is helpful to first examine the initial and final states, the tulip and V flames, respectively. The tulip flame, illustrated by the average HRR field in figure 2(*a*), is stabilised by a BVB mode, having just an inner ISL-stabilised branch, which is rooted at the pilot spray (thus, a BVB/S-ISL flame). Figure 6(*a*) shows an instantaneous

https://doi.org/10.1017/jfm.2025.10937 Published online by Cambridge University Press

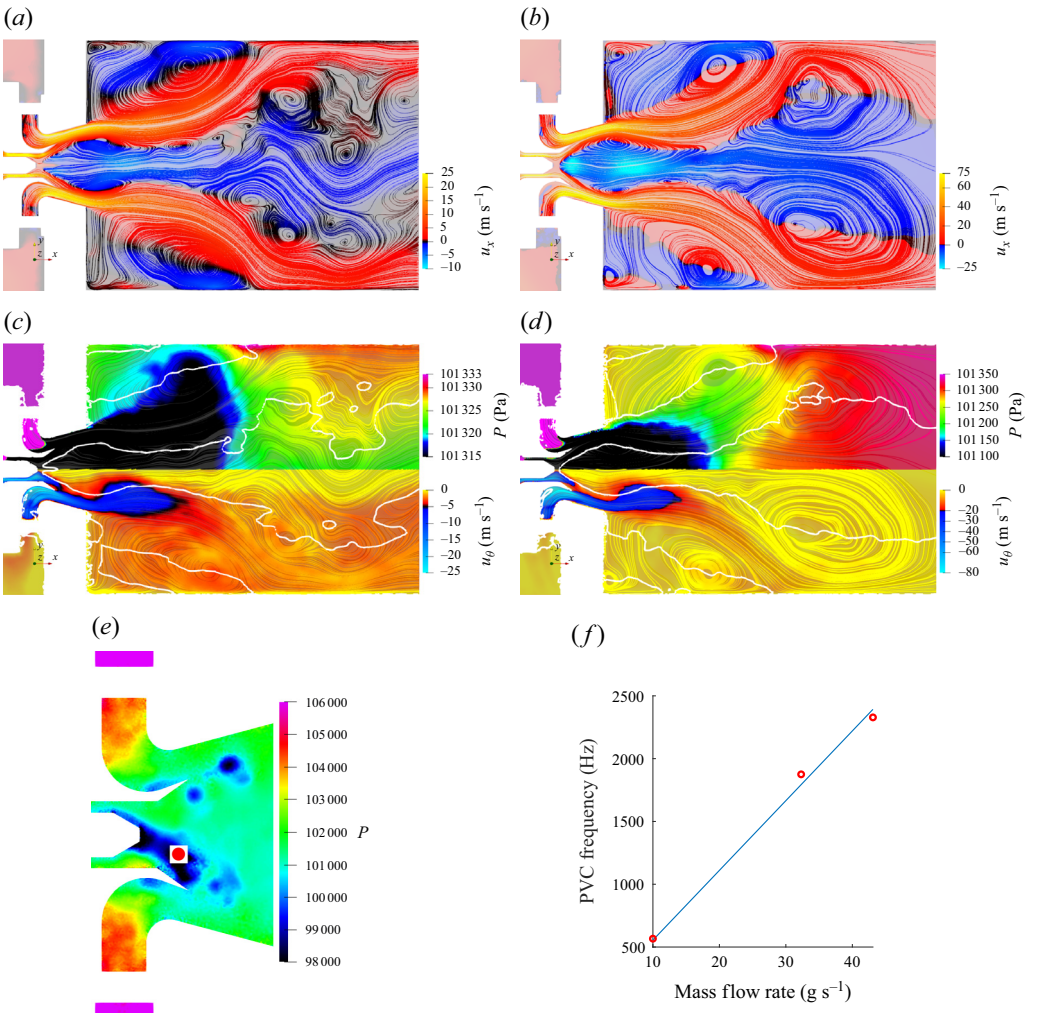


Figure 5. Large-eddy simulation results, time averaged over 40 ms, of OP_{lp} non-reacting flow (*a*) axial velocity and (*c*) pressure (top) and swirl velocity (bottom). Panels (*b*) and (*d*) represent the same fields, respectively, for the OP_1 non-reacting flow. The flow is swirling clockwise (negative u_θ) with respect to the axial direction. The recirculation zones are shown in blue in panels (*a*) and (*b*) and by the white contour of $u = 0$ m/s in panels (*c*) and (*d*). (*e*) Large-eddy simulation instantaneous pressure field showing the PVC in the low-pressure regions, with the measurement point for its frequency indicated by the red dot. (*f*) Linear correlation between PVC frequency and mass flow rate for the studied operating points in Table 4.

snapshot of the flame and its interaction with the spray, being attached to it. However, the tulip flame branches are stabilised by the bubble-shaped ISL, not following the spray droplets outwards, which mostly have a conical trajectory. Similarly to the non-reacting case, a PVC is also present with the same characteristic frequency, as the spray pushes the tulip flame downstream and allows sufficient space for the PVC to develop. The PVC has a strong interaction with the spray and imposes its dynamics on the spray for both the OP_1 $\phi = 0.5$ and $OP_{transition}$ $\phi = 0.7$ cases, dispersing the droplets and improving mixing (as generally shown for spray flames interacting with vortical structures, like in Dagan, Arad & Tambour (2015); Renaud *et al.* (2015*a*); Mesquita (2021)). A major characteristic of the BVB topology is the CRZ in depression compared with the swirling

https://doi.org/10.1017/jfm.2025.10937 Published online by Cambridge University Press

Operating Point	$\dot{m}_{air}$	T_{air}	$\dot{m}_{fuel}$	Power	Equivalence ratio ϕ	Staging factor α
OP_{lp}	10.0 g s^{-1}	473 K	0.45 g s^{-1}	21 kW	0.7	100 %
OP_1	32.3 g s^{-1}	473 K	1.02 g s^{-1}	45.9 kW	0.5	100 %
$OP_{transition}$	32.3 g s^{-1}	473 K	1.50 g s^{-1}	68 kW	0.7	100 %
OP_2	43.1 g s^{-1}	433 K	1.64 g s^{-1}	72 kW	0.6	15 %

Table 4. Studied operating points for the tulip-to-V flame shape transition and its parameters.

flow (figure 6*g*). This point will be discussed in greater detail in the following sections by analysing the radial momentum balance, but it is important to observe that the CRZ depression is responsible for the inward closing of the tulip flame branches: as it attracts the flow, droplets and fuel, the tulip flame branches bend inwards. Figure 6(*c*) presents the average flame superimposed on the mixture fraction field, showing that most of the flame branches are burning in a premixed lean regime at the global equivalence ratio, with only the flame root, attached to the spray, burning as a multi-regime spray flame in a rich mixture. Compared with the non-reacting field, which also presents a BVB mode, the tulip flame causes the CRZ bubble to stretch axially due to the increase in axial momentum caused by reaction (figure 6*e*). Thus, the bubble has a more elliptical shape, and the flow presents an hourglass-like shape: the first part is the bubble, followed by a bottleneck contraction, and the second part of the CRZ exhibits a divergent shape. This elliptic bubble and hourglass-shaped flow topology can also be seen in the flow field of the 'Trumpet-like' flame (assumed to be BVB/A-ISL) from Terhaar *et al.* (2014). We believe that this hourglass flow topology may be exclusively present in reacting flows, more specifically in BVB/A, F, S-ISL flames. Further theoretical work on this point would be valuable.

The V flame is illustrated by the average HRR field in figure 2(*b*), which shows its main characteristics: it is a conical flame, with its inner branches attached to the spray and stabilised over the conical ISL created by the CVB flow topology that stabilises the flame (thus, a CVB/S-ISL flame). Figure 6(*b*) shows an instantaneous snapshot of the V flame and its interactions with the spray: at the centre line, some droplets penetrate the CRZ, but most of the spray interacts with the flame branches until complete evaporation, as the spray also has a conical trajectory. Additionally, as for the tulip flame, the spray positions the flame sufficiently away from the pilot injector to allow a PVC to develop, which interacts with the spray, enhancing mixing, and with the flame, exciting it. Figure 6(*d*) presents the average V flame superimposed on the mixture fraction field, showing a very similar structure to the tulip flame, with a multi-regime-rich spray flame at its roots, but with flame branches burning in a premixed lean regime at the global equivalence ratio. As shown by the flames and flow fields, and highlighted by the flame shape nomenclature (tulip is a BVB/S-ISL, while the V flame is a CVB/S-ISL), the only difference between a tulip flame and a V flame is the vortex breakdown mode, as the flame structure, combustion regime and spray interactions are similar. This emphasises the role of the vortex breakdown mode in impacting the flame shape. Looking at the velocity (figure 6*f*) and pressure (figure 6*h*) fields, one can see the aerodynamics characteristics of the CVB mode, a large conical CRZ and that the CRZ is not in depression compared with the swirling jet (only the presence of the PVC is captured by the small low-pressure region downstream of the pilot injector).

To further understand the differences between the two vortex breakdown modes in these reacting conditions and the aerodynamic mechanisms that stabilise each of them, we investigate the velocity and pressure profiles for each mode. Figure 7 collect these

https://doi.org/10.1017/jfm.2025.10937 Published online by Cambridge University Press

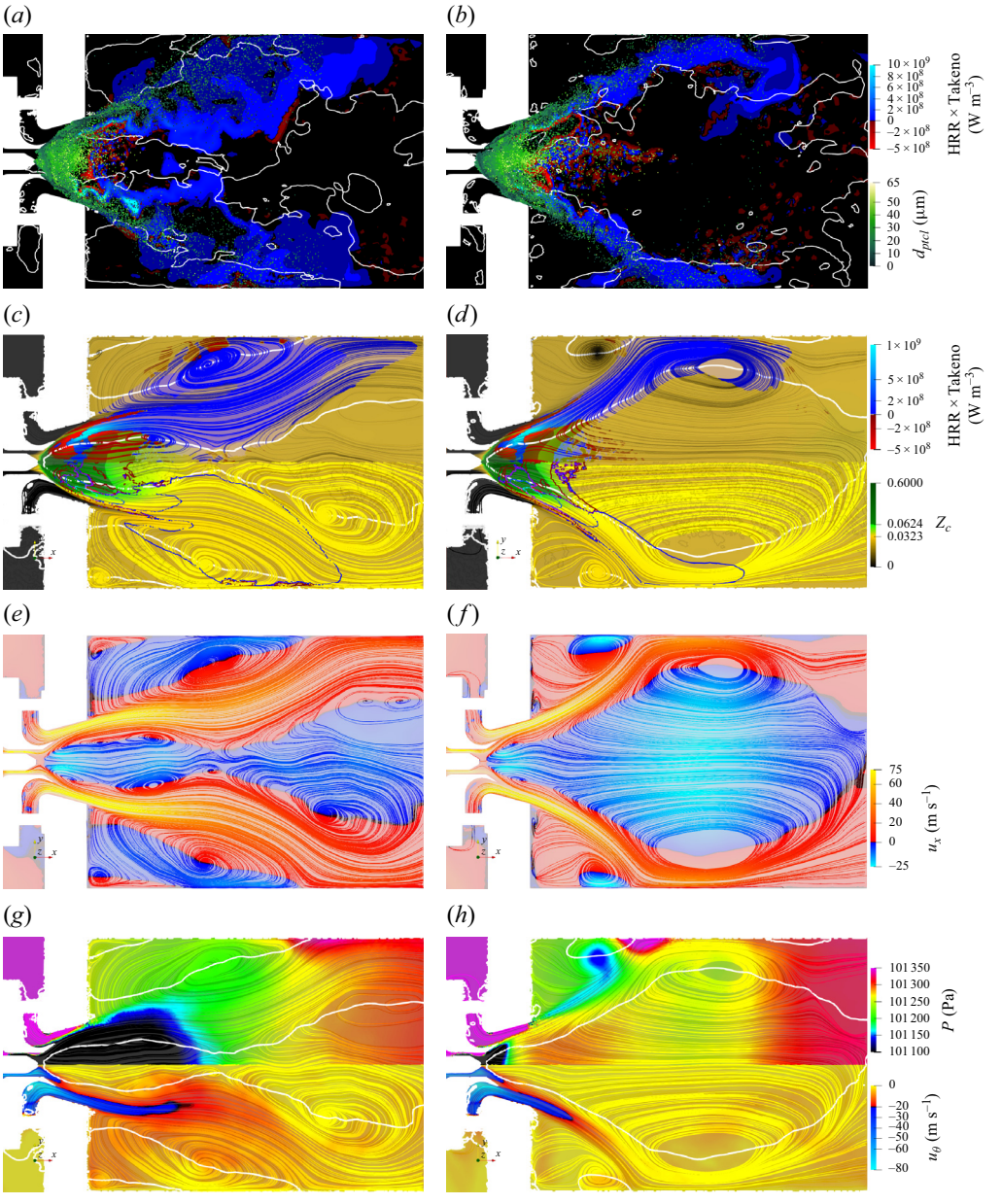


Figure 6. Large-eddy simulation results of OP_1 tulip flame: (*a*) instantaneous positive HRR times the Takeno index (TI) $HRR \times TI = HRR \cdot \nabla Y_{kerosene} \cdot \nabla Y_{O_2} / |\nabla Y_{kerosene} \cdot \nabla Y_{O_2}|$ (clipped to fit in the limits [−5e8; 1e9]), showing premixed combustion regions in blue and non-premixed ones in red, with superposed Lagrangian fuel droplets coloured by diameter; Time-averaged over 40 ms (*c*) $HRR \times TI$ field superposed to Bilger's carbon-defined gaseous mixture fraction, (*e*) axial velocity field, and (*g*) pressure (top) and swirl velocity (bottom) fields. Panels (*b*), (*d*) (*f*) and (*h*) represent the same fields, respectively, for the OP_1 V flame. The flow is swirling clockwise (negative u_θ) with respect to the axial direction. The recirculation zones are shown in blue in panels (*e*) and (*f*) and by the white contour of $u = 0$ m/s in the other panels.

https://doi.org/10.1017/jfm.2025.10937 Published online by Cambridge University Press

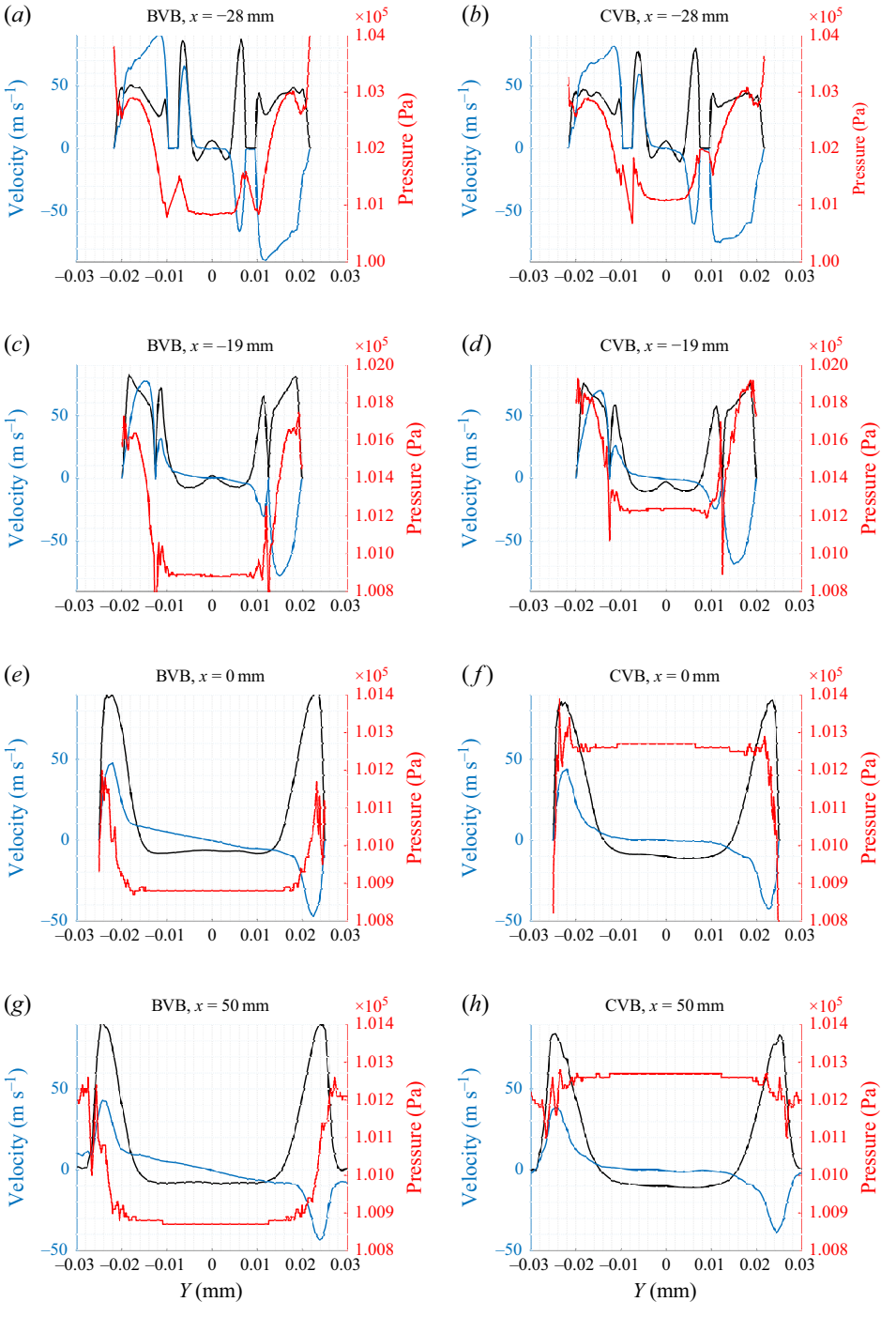


Figure 7. The OP_2 time-averaged profiles of swirl (blue) and axial (black) velocity and pressure (red) at different axial positions for the tulip flame BVB mode – (*a*), (*c*), (*e*) and (*g*), and V flame CVB mode – (*b*), (*d*), (*f*) and (*h*). As an axial reference, the entry of the combustor is at 0.0 mm and the CRZ contraction for the BVB mode at 70 mm. The small peak of positive axial velocity inside the CRZ shown in (*a*) to (*d*) is a consequence of air entrainment caused by the pilot spray; (*a*) BVB, $x = -28$ mm, (*b*) CVB, $x = -28$ mm, (*c*) BVB, $x = -19$ mm, (*d*) CVB, $x = -19$ mm, (*e*) BVB, $x = 0$ mm, (*f*) CVB, $x = 0$ mm, (*g*) BVB, $x = 50$ mm, (*h*) CVB, $x = 50$ mm.

https://doi.org/10.1017/jfm.2025.10937 Published online by Cambridge University Press

profiles for the OP_2 flames, shown here instead of OP_1 because in OP_2 there is no PVC and the characteristics of the two vortex breakdown modes are stronger due to the higher air mass flow rate. For both modes, until the entry of the divergent piece, the point where the airflow coming from the pilot and the multipoint stages mix, each air stage and swirler creates its own swirling vortex, two pairs of concentric vortices being visible in figure 7(*a*) and 7(*b*). As the flow moves downstream, the two swirling vortices merge, as illustrated in figures 7(*c*) and 7(*d*), resulting in a single swirling vortex further downstream. However, there is a notable difference between the BVB and CVB modes once the swirling vortices combine to form a single vortex and stabilise within the divergent region. Analysing the BVB profile (figures 7*e* and 7*g*), one can see an irrotational vortex region at the outmost positions, followed by a first rotational vortex region and then, in the CRZ, a second rotational region. This indicates that in the BVB mode, the swirling jet and the CRZ form part of the same vortex, where the CRZ rotates in solid-body motion alongside the swirling jet. In opposition, for the CVB mode (figures 7*f* and 7*h*), only the swirling jet rotates while the flow inside the CRZ does not. This is a major difference between the two topologies in reacting conditions and an important new insight into swirling flows. Indeed, Candel *et al.* (2014) states that swirling flows generally have the same classic vortex velocity profile, such as a Rankine or a Lamb–Oseen vortex, where the vortex core is in quasi-solid-body rotation (i.e. a rotational vortex). However, this does not apply to the CVB mode, which features a non-rotating, axial recirculating flow. The CVB then creates a setting where the swirling jet moves as if it were rotating around a non-rotating core, with the CRZ acting almost as a conical bluff body. These conclusions agree with the observations of Terhaar *et al.* (2015), who stated that it is required to impose a certain inlet velocity profile to enable the flow to stabilise in a CVB mode.

Furthermore, for the CVB mode, there is no strong negative radial pressure gradient inside the CRZ compared with the BVB mode, likely because the CVB recirculating flow is not rotating. The swirling motion of the jet only creates an axial pressure gradient due to the decreasing level of swirl as the jet moves downstream. This differs from the non-reacting turbulent CVB shown by Moise & Mathew (2021), which presents a CRZ in depression with respect to the swirling jet, even though the pressure difference is rather small and also smaller compared with the BVB case. It would be important to investigate whether the absence of depression and flow rotation in the CRZ is exclusive to a reacting CVB due to the higher temperature of the burnt recirculating gases or characteristic of the BIMER geometry, where the flame, swirl level and flow interaction with the walls could be in the right balance to allow this to happen. Based on a comparison of these results with those presented by Moise & Mathew (2021) for the non-reacting CVB, we will assume that the absence of flow rotation and depression in the CRZ is a characteristic of a reacting CVB. This assumption is made because all the CVB modes observed in the BIMER combustor are reacting (thus, we cannot directly compare non-reacting and reacting modes for the CVB), and because all the reacting CVB modes identified in the BIMER combustor exhibited the absence of rotation and depression within the CRZ. Additionally, Moise & Mathew (2021) raise the concern that in some non-reacting cases, less experienced observers may mistake the two modes for one another due to their similarities. The observations above provide additional insights into how to distinguish between the BVB mode and the CVB mode in reacting cases (other than the flame shape, which differs for a BVB or CVB mode).

A follow-up question that could be asked is why the CRZ is in rotation in the BVB mode and not in the CVB one. One possible explanation involves the timing of when the gas begins to recirculate. In the BVB mode, this occurs much earlier, at around $x = 70$ mm, where the flow still retains a significant amount of swirl motion (as shown in figure 6*g*).

https://doi.org/10.1017/jfm.2025.10937 Published online by Cambridge University Press

In contrast, in the CVB mode, the flow only begins to recirculate after reaching the wall much farther downstream, at approximately $x = 120$ mm. By this point, all the swirl momentum has dissipated, thus the recirculating flow is mostly axial (as shown in figure 6*h*), creating the bluff-body-like non-rotating CRZ.

5.3. *Flame shape time evolution and transition*

After gaining a better understanding of the differences between the two flame shapes and their respective flow fields, we proceed to study the transition. From the OP_1 tulip flame, the equivalence ratio is increased to $\phi = 0.7$, by increasing the fuel mass flow at a rate of 10 % increase per millisecond until reaching the operating point $OP_{transition}$ value as shown in table 4. Figure 8 compares the tulip flame and flow field after the equivalence ratio has been changed. One can see that increasing the pilot flow increases the size of the fuel-rich zone where the spray is present. The structure of the flame remains unchanged, with the flame region attached to the spray still burning in a partially premixed multi-regime (as it interacts with droplets and the fuel-rich mixture), while the flame branches continue to burn mostly in a lean-premixed mode. However, the increase in fuel inside the recirculation zone will intensify the partially premixed zone of the flame, causing a local temperature increase in the CRZ bubble, in addition to the general increase in temperature in the combustor caused by the higher equivalence ratio. The ISL branches of the tulip flame are particularly important for the transition precisely because they cause an increase in temperature inside the CRZ bubble. Indeed, if this were any of the M-BVB flames in figure 2 (BVB/L-BLE/A-OSL) instead of a tulip flame (BVB/S-ISL), this transition would not occur, because the bubble would not be heated. The impact of the tulip flame's temperature increases on the transition is detailed in the following paragraphs. Looking at the flow fields (figure 8*c*, 8*d*, 8*e*, 8*f*), one can see that the increase in spray mass flow does not affect the flow field significantly, neither the flow topology or the swirl level (as the fuel is also swirling). The air mass flow rate is much higher than the fuel flow, and the PVC imposes its dynamics over the spray, which minimises the impact of the fuel flow on the air. Thus, the only relevant change after the increase in equivalence ratio is the increase in temperature.

The evolution of the tulip flame is shown in figure 9, from the moment $t = 0$ ms, when the equivalence ratio has reached its final $\phi = 0.7$ value (figure 9*a*), to $t = 100$ ms (figure 9*h*). The flame shape remains the same for the first 60 ms (figure 9*d*), without any visible change. However, after $t = 70$ms (figure 9*e*), the flame branches, stabilising over the ISL, quickly expand radially. The CRZ also begins to expand radially, starting from the bottleneck just behind the CRZ bubble. At $t = 80$ms (figure 9*f*), the flame already exhibits a different shape, with the flame branches over the ISL considerably more radially open and pointing outwards. At $t = 100$ms (figure 9*h*), the flame has fully transitioned to a V shape (figure 2*b*), with its characteristic open flame branches going towards the walls. The CRZ has significantly expanded and changed to a conical shape. This indicates that increasing the equivalence ratio from $\phi = 0.5$ to $\phi = 0.7$ at OP_1 prompted the transition from a tulip flame to a V flame.

5.4. *Flow evolution*

Even if the flame shape lags around 70 ms to react to the change in equivalence ratio, some other aspects of the flow respond before the flame. It is useful to have in mind some flow convective time scales to put the transition time scales into perspective. The average convective times from the injector to the flame are between 0.2 ms (upstream-most portion of the flame, attached to the spray) and 5 ms (end of the flame branches),

https://doi.org/10.1017/jfm.2025.10937 Published online by Cambridge University Press

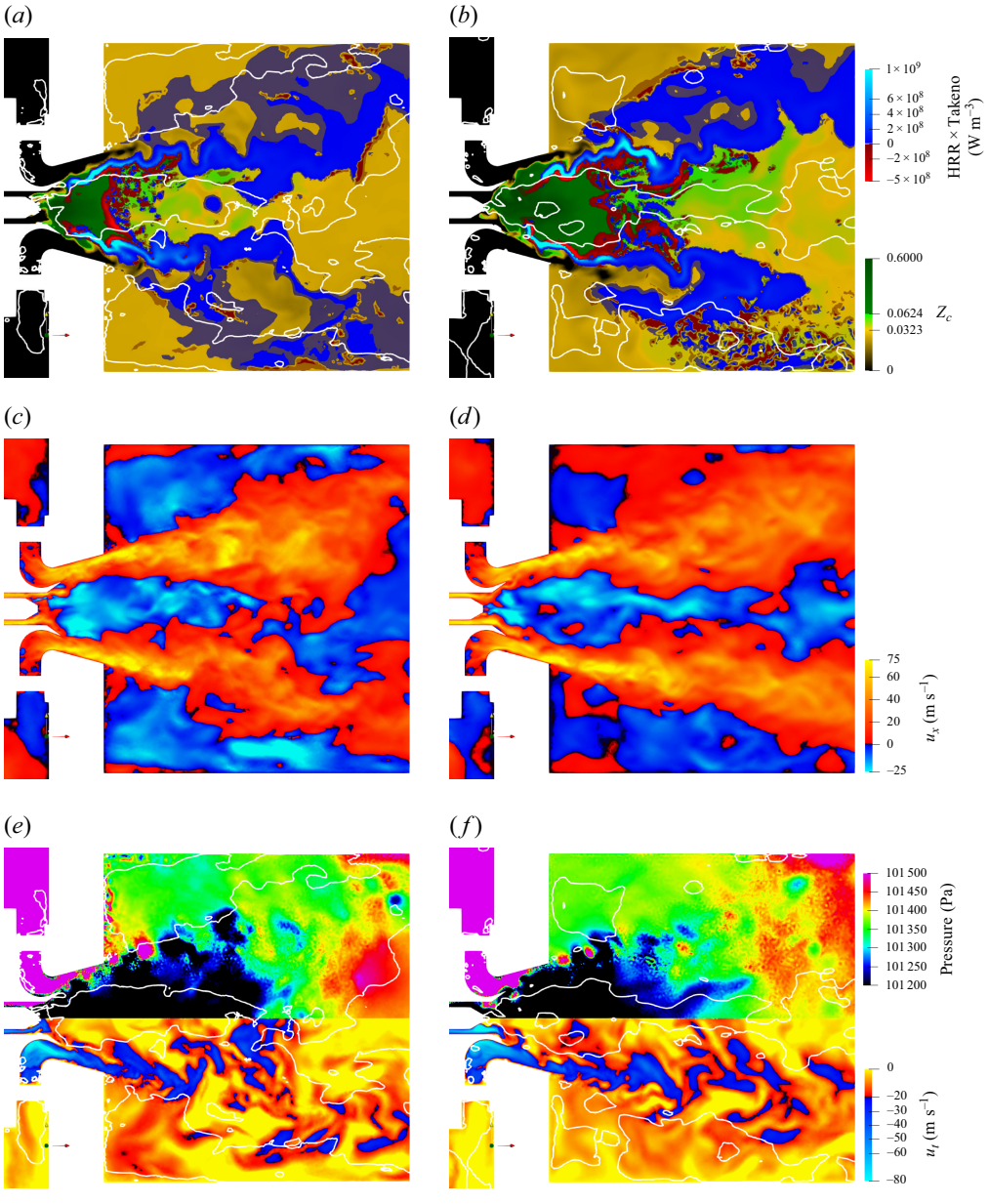


Figure 8. Large-eddy simulations instantaneous snapshots of OP_1 tulip flame (*a*) positive HRR times the TI $HRR \times TI = HRR \cdot \nabla Y_{kerosene} \cdot \nabla Y_{O_2} / |\nabla Y_{kerosene} \cdot \nabla Y_{O_2}|$ (clipped to fit in the limits [−5e8; 1e9]), showing premixed combustion regions in blue and non-premixed ones in red, superposed to Bilger's carbon-defined gaseous mixture fraction; (*c*) axial velocity; and (*e*) pressure (top) and swirl velocity (bottom). Panels (*b*), (*d*) and (*f*) represent the same fields, respectively, for the $OP_{transition}$ tulip flame. The flow is swirling clockwise (negative u_θ with respect to the axial direction). The recirculation zones are shown in blue in panels (*c*) and (*d*) and by the white contour of $u = 0$ m/s in the other panels.

which are much shorter than 60 ms. For the recirculation zone, characteristic times vary depending on the region. For the bubble portion (region before the bottleneck contraction), recirculation time is on average ≈ 23 ms from the injector, while for the second half of the recirculation zone, this takes approximately ≈ 60 ms, which is in the same range as the

https://doi.org/10.1017/jfm.2025.10937 Published online by Cambridge University Press

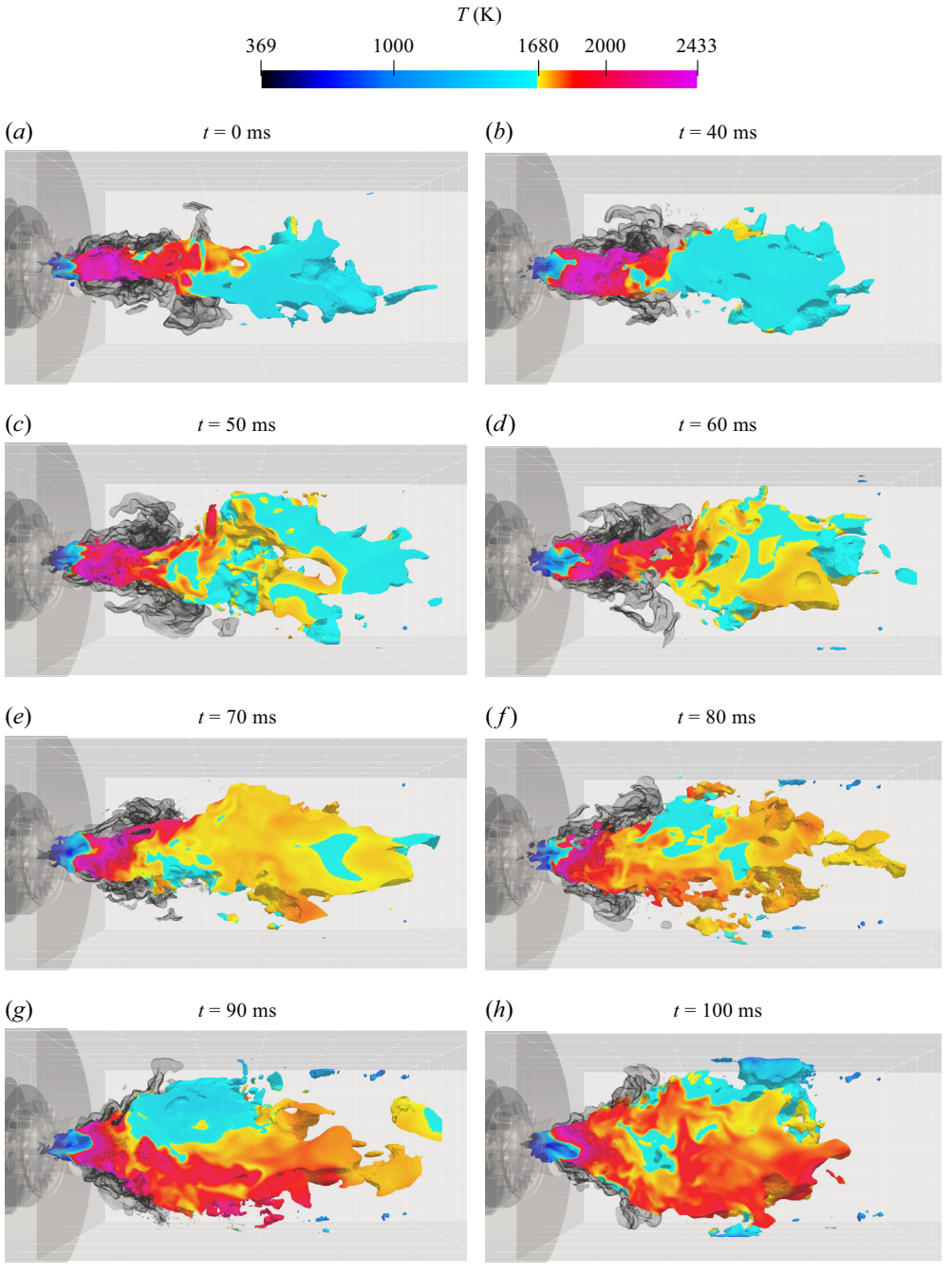


Figure 9. Three-dimensional visualisation of the CRZ by a clip at the centre plane of the iso-volume of negative axial velocity coloured by temperature. The flame is depicted by a black, transparent wireframe, defined as the iso-surface of HRR at $5 \cdot 10^7$ W/m^3.

transition times. This highlights the role of the different parts of the recirculation zone in the transition, which will be analysed closely in the following sections. Another flow aspect that is important to track over time is CRZ pressure, as a defining feature of the

https://doi.org/10.1017/jfm.2025.10937 Published online by Cambridge University Press

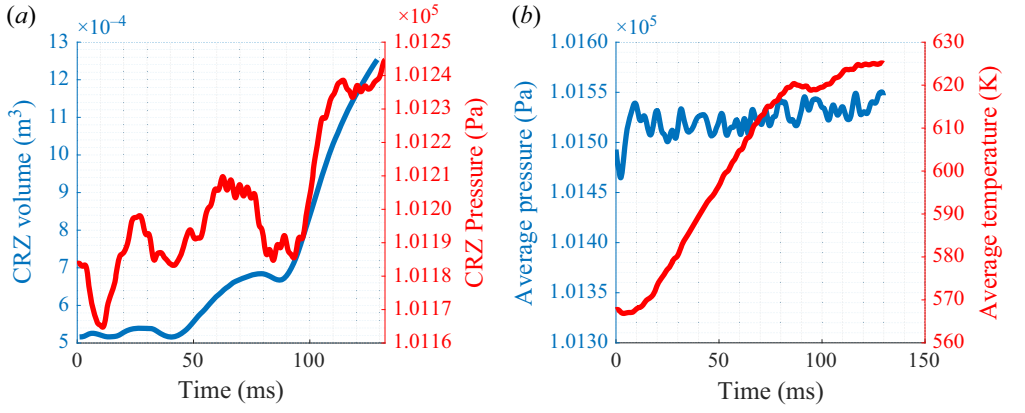


Figure 10. (*a*) Time evolution of the CRZ volume and pressure. Both signals are filtered with a second-order low-pass Butterworth filter with a cutoff frequency of 20 Hz. (*b*) Time evolution of the spatial average of pressure and temperature inside the combustion chamber.

tulip flame is the BVB topology, which features a CRZ bubble in depression with respect to the rest of the flow, as shown in figure 6. However, as already discussed, the final V flame has a conical CRZ (figure 6*f*) that is not in depression because the V flame is stabilised over a flow with a CVB mode (figure 6*h*), characterising not only a flame shape transition, but also a vortex breakdown mode transition. Differently from Santhosh *et al.* (2014), Terhaar *et al.* (2015), Santhosh & Basu (2016) or Rajamanickam & Basu (2018), here, the vortex breakdown mode transition occurs without little modification on the incoming flow velocities (such as changing the swirl number), as the increase in fuel mass flow to reach $\phi = 0.7$ does not alter the air flow significantly (as shown in figure 8). It is relevant, then, to follow how the CRZ behaves during the transition to understand the mechanism behind the vortex breakdown mode transition and its link with the flame shape transition. The time evolution of the CRZ volume and of the average pressure inside the first part of the CRZ (up to the CRZ contraction and bottleneck at $x = 0.07$ m) is plotted in figure 10(*a*). It is important to note that both quantities oscillate because of the excitation of the longitudinal acoustic mode of the combustion chamber at around 300 Hz (Renaud 2015; Mesquita *et al.* 2021*b*; Mesquita 2021), but they present an average mostly constant up to $t = 50$ ms. The works of Douglas *et al.* (2022) and O'Connor & Lieuwen (2012) show that acoustic excitation can change the structure of the flow field; however, this is not the case for the BIMER combustor. As shown by Mesquita (2021), the flow topology is the same between the non-reacting and the M flame flow fields, which is the flame with the highest activity of the longitudinal mode in the BIMER combustor. Similarly, the OP_1 and OP_2 tulip flames have the same topology and flow structure, but the OP_2 flame has a considerably higher activity of the longitudinal mode. Ruling out the impact of the longitudinal mode in the flow structure and topology and back to the time evolution of the CRZ, at instant $t = 50$ ms, the CRZ volume and pressure start to increase slowly and then more abruptly after $t \approx 90$ ms. This indicates that the evolutions of CRZ pressure and volume are correlated with each other and with the flame shape, as all three evolve synchronously.

Simultaneously with the flow evolution, one must consider what triggers this transition: the increase in equivalence ratio. Figure 10(*b*) shows the time evolution of the average pressure and temperature inside the chamber. The average temperature is constantly increasing due to the increase in equivalence ratio, stabilising only after 120 ms, while the

https://doi.org/10.1017/jfm.2025.10937 Published online by Cambridge University Press

average pressure inside the chamber evolves much less over the whole transition than the pressure inside the CRZ. These results indicate that both the CRZ shape and temperature evolution are closely related to the flame shape and the transition from vortex breakdown mode. To further study the transition, the following sections analyse the CRZ evolution and then consider the temperature effect.

5.5. *The CRZ radial balance evolution*

The radial evolution of the CRZ and the vortex breakdown can be understood by looking at the radial momentum balance in a cylindrical coordinate system

$$\rho\left(\frac{\partial u_r}{\partial t}+u_r\frac{\partial u_r}{\partial r}+u_x\frac{\partial u_r}{\partial x}\right)=\rho\frac{u_\theta^2}{r}-\frac{\partial p}{\partial r}+\left[\frac{1}{r}\frac{\partial}{\partial r}(r\tau_{rr})-\frac{\tau_{\theta\theta}}{r}+\frac{\partial \tau_{xr}}{\partial x}\right], \tag{5.1}$$

where ρ is the density, u_r the radial velocity component, u_θ the swirling velocity component, p the pressure and τ the shear stress tensor. When studying the vortex breakdown region, the centrifugal force and radial depression terms are considered to be the most relevant ones for the radial velocity budget (Lucca-Negro & O'Doherty 2001; Krause 1985; Brown & Lopez 1990; Lopez 1990). Considering this assumption, the radial momentum balance is reduced to

$$\rho\left(\frac{\partial u_r}{\partial t}+u_r\frac{\partial u_r}{\partial r}+u_x\frac{\partial u_r}{\partial x}\right)=\rho\frac{u_\theta^2}{r}-\frac{\partial p}{\partial r}. \tag{5.2}$$

Thus, as these quantities are representative of the radial evolution of the flow at the vicinity of the vortex breakdown (i.e. the CRZ boundaries), their evolution in time during the transition is plotted in figure 11 for a point over the CRZ boundary at the axial position of its bottleneck contraction ($x = 0.07$ m, $\theta = 0$ rad, i.e. centreline, and the radial position of the measurements follow the radial position of the CRZ contraction, i.e. figure 11*e*). First, one can see that during the transition the swirl velocity at this position mostly oscillates up to $t \approx 60$ ms, before reaching a minimum at $t \approx 70$ ms (figure 11*a*). The gradual increase of the pressure inside the CRZ (figure 10*a*) also increases the inverse of the radial pressure gradient (figure 11*b*). As the centrifugal force remains mostly constant up to $t \approx 60$ ms (as shown by the swirl velocity), the radial balance ($\rho u_\theta^2/r - \partial p/\partial r$) is mostly controlled by the radial pressure gradient, the radial balance progressively increasing with the increase in pressure inside the CRZ (figure 11*c*). With the radial balance becoming positive at $t \approx 70$ ms, this accelerates the flow outwards radially, the radial velocity component increasing in magnitude from this moment on (figure 11*d*) and ending with a positive value. This results in the radial expansion of the CRZ from $t \approx 70$ ms on, as shown by figure 11(*d*).

These results demonstrate how the radial expansion of the CRZ are linked to the progressive increase in pressure inside the CRZ bubble. The next section then discusses how the change in equivalence ratio can be linked with this suppression of the CRZ bubble depression.

5.6. *Temperature evolution and CRZ expansion*

As shown in figure 10(*b*), the temperature inside the combustion chamber constantly increases during this transition. The previous section demonstrated how the dynamics of the CRZ are linked to the flame shape transition; it is then necessary to follow the temperature evolution of the CRZ.

Figure 9 shows the temperature evolution over a slice of the iso-volume of negative axial velocity, representing the CRZ, along with the flame. At the initial instant, looking

https://doi.org/10.1017/jfm.2025.10937 Published online by Cambridge University Press

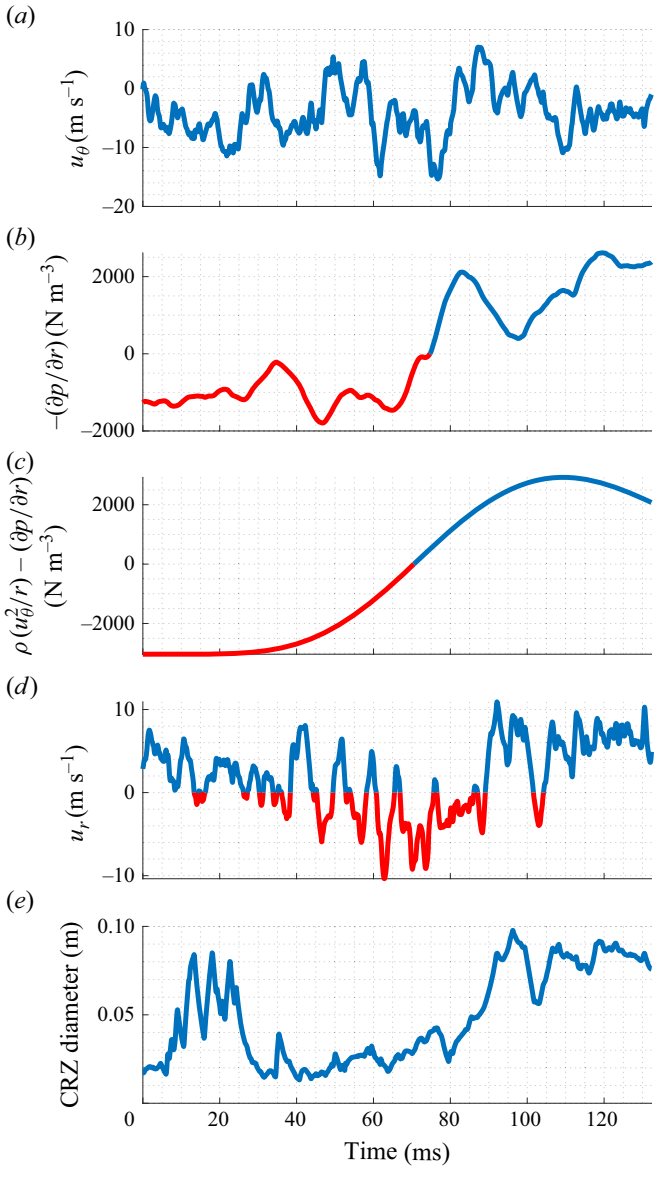


Figure 11. Dynamics and kinematics of a point over the CRZ at its contraction ($x = 0.07$ m): (*a*) velocity swirl component, (*b*) negative of the radial pressure gradient, (*c*) balance between centrifugal force and radial pressure gradient, (*d*) velocity radial component and (*e*) CRZ diameter. The radial pressure gradient signal is filtered with a second-order Butterworth low-pass filter with a cutoff frequency of 20 Hz. The balance between centrifugal force and radial pressure gradient is filtered using a sixth-order Butterworth low-pass filter with a cutoff frequency of 10 Hz. The velocity and diameter signals are filtered with a first-order Butterworth low-pass filter with a cutoff frequency of 60 Hz.

at the initial tulip flame (figure 9*b*), one can see that the temperature inside the CRZ is not uniform. First, the CRZ bubble presents very high temperatures since the roots of the flame over the ISL burn in a non-premixed regime. The second half of the CRZ exhibits lower temperatures, as the flame branches predominantly burn in a premixed regime around the global lean equivalence ratio value of $\phi = 0.7$. Thus, the two parts of the CRZ heat

https://doi.org/10.1017/jfm.2025.10937 Published online by Cambridge University Press

differently due to the flame structure, and the increase in equivalence ratio affects the two parts of the CRZ differently. While the CRZ bubble heats quickly, due to its size and proximity to the flame, the second half of the CRZ takes much longer to heat, as it is much larger and far from the flame. Indeed, as mentioned above, the recirculating times for the CRZ bubble are ≈ 22 ms from the injector, while it takes ≈ 60 ms for the flow to recirculate through the second half of the CRZ and reach the bottleneck contraction. Interestingly, it is the convective and heating time scales of the second half of the CRZ that are closely linked with the flame shape transition. Figures 9(*b*), 9(*c*), 9(*d*) and 9(*e*) show how progressively the temperature increases inside the second half of the CRZ up to $t = 70$ ms, with little modification of the flame shape and CRZ size. Between $t = 70$ ms (figure 9*e*) and $t = 80$ ms (figure 9*f*), the second half of the CRZ has mostly heated up to its final temperature. The bottleneck zone between the two parts of the CRZ is significantly warmer and begins to expand radially. At $t = 90$ ms (figure 9*g*), the CRZ is composed of a single conical part, which is warmer and only shows colder temperatures locally at its external boundaries. At $t = 100$ ms (figure 9*h*), one can clearly observe the conical flame and more uniform CRZ after the transition.

These results illustrate how the convective time of the flame, the temperature of the CRZ, its diameter and the flame shape are linked. As the flame branches are stabilised over the ISL, the heating and consequent expansion of the CRZ are responsible for the opening of the flame, which follows the ISL as the CRZ expands. However, the triggering of the change in shape at approximately $t \approx 70$ ms remains unexplained. To investigate this further, a link between the radial momentum balance and the CRZ pressure and temperature is proposed in the next section, based on the stable tulip flame, studied in Mesquita *et al.* (2023*b*) and the starting point of this transition.

5.7. *Criterion for the tulip flame and BVB mode transition*

As discussed in § 5.5, in the vicinity of the vortex breakdown, the radial motion of the flow is controlled by the balance between centrifugal force and radial pressure gradient (5.2). Indeed, looking at the three points over the streamline in the vicinity of the vortex breakdown in figure 6, one can see that:

(i) at P_1 the balance is positive and the flow is moving outwards;
(ii) between P_1 and P_2 the balance becomes negative, decelerating the flow and at P_2 the flow start going inwards;
(iii) P_3 is at the limit of the bottleneck region, where the CRZ bubble depression induces a smaller effect and the flow shows a very low swirl velocity. Thus, in this region, the balance is close to zero and oscillates.

Following this analysis, for a given point in the vicinity of the vortex breakdown

$$\rho \frac{u_\theta^2}{r} - \frac{\partial p}{\partial r} > 0\,; \quad \text{flow accelerated outwards,} \tag{5.3}$$

$$\rho \frac{u_\theta^2}{r} - \frac{\partial p}{\partial r} < 0\,; \quad \text{flow accelerated inwards.} \tag{5.4}$$

Thus, during this transition, the flow in the vicinity of the vortex breakdown must be accelerated outwards for the CRZ to expand radially. Thus, for this to be true, (5.3) must be verified. This is shown in figure 11(*c*) for the boundaries of the bottleneck region, represented by P_3 in figure 6. Considering a first-order approximation for the radial pressure gradient, we have

https://doi.org/10.1017/jfm.2025.10937 Published online by Cambridge University Press

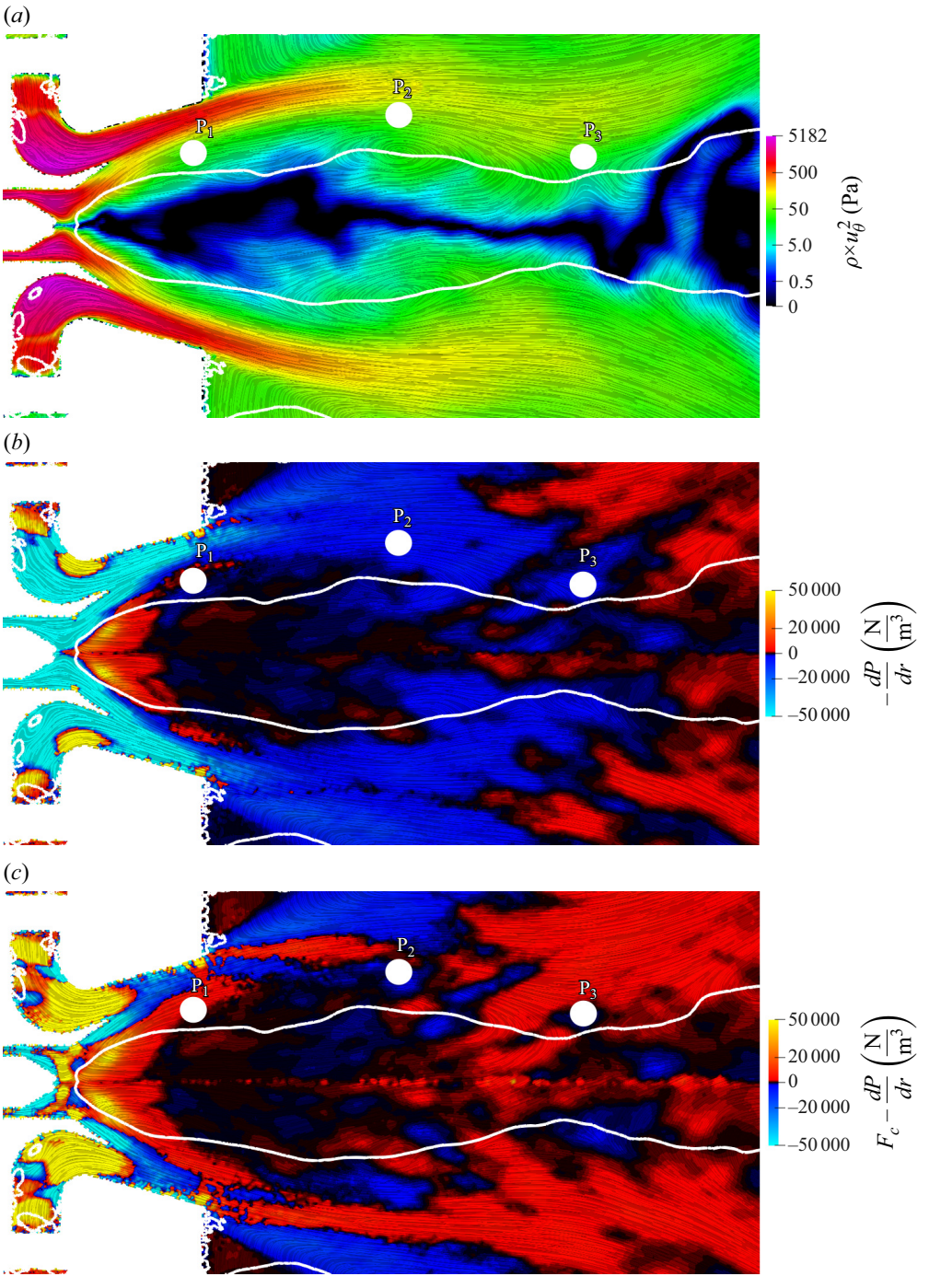


Figure 12. Time-averaged flow of the OP_1 stable tulip flame: LES fields time-averaged over 40 ms of (*a*) density (ρ) times the square of swirl velocity (u_θ^2), (*b*) the negative of the radial gradient of pressure and (*c*) radial balance between centrifugal force ($F_c = \rho u_\theta^2 / r$) and radial pressure gradient. The CRZ is limited by the white contour of $u = 0$ m/s.

https://doi.org/10.1017/jfm.2025.10937 Published online by Cambridge University Press

$$\rho \frac{u_{\theta,\,swirling\ jet}^2}{r_{CRZ}} - \frac{p_{swirling\,jet} - p_{axis}}{r_{vortex\ core}} > 0, \tag{5.5}$$

where in this case ρ is the local gas density, $u_{\theta,swirling\,jet}$ and $p_{swirling\,jet}$ are the swirl velocity and pressure, respectively, of the swirling jet at the vicinity of the vortex breakdown (e.g. at P_1, P_2 or P_3), p_{axis} is the pressure at the axis of rotation (i.e. the centreline of the chamber) and $r_{vortex\ core}$ is the radius of the vortex at the zone of interest, here the CRZ (thus $r_{CRZ} = r_{vortex\ core}$). As in this case, the CRZ radius is non-zero, we have

$$p_{axis} > p_{transition} = p_{swirling\,jet} - \rho u_{\theta,swirling\,jet}^2. \tag{5.6}$$

Thus, if the pressure at the axis is higher than the right-hand side term, the flow goes outward. This configures a first criterion to evaluate the stability of the tulip flame, establishing that the CRZ bubble opens and the flame shape changes if the pressure inside the CRZ exceeds $p_{transition}$. Averaging the value of $p_{transition}$ at the immediate vicinity outside the CRZ (by using an iso-surface of null axial velocity) and up to the bottleneck ($x = 0.07$ m) using time-averaged local values of the stable OP_1 tulip flame results in $p_{transition} \approx 101\,130$ Pa.

This value is then used as a reference when following the evolution of the average quantities inside the CRZ bubble and in the second half of the CRZ during the transition, as shown in figure 13. Following first the phenomena inside the CRZ bubble (figure 13 - red lines), its average temperature (figure 13*a*) and pressure (figure 13*b*) are increasing until reaching $P \approx P_{transition} = 101\,130$ Pa at $t \approx 47$ ms. At this moment, both the gas mass flux from the second half of the CRZ towards the CRZ bubble (figure 13*c*) and the volume of the second half of the CRZ (figure 13*d* – blue line) start to increase, causing both the temperature and pressure inside the bubble to decrease, the pressure going under the $P \approx P_{transition} = 101\,130$ Pa threshold. The volume of the CRZ bubble and its temperature then stabilise at $t \approx 60$ ms. Up to this time, the flame shape (figure 9*d*) and the flame diameter (figure 13*e*) remain unchanged.

Looking at the second half of the CRZ, after $t = 47$ ms, its temperature and the mass flux from it towards the bubble have kept increasing (figures 13*a* and 13*c*, respectively). However, as the volume of the CRZ bubble has stabilised at $t = 60$ ms (figure 13*d*), the increasing mass flux of burnt gas (at an also increasing temperature) results in a new increase in the pressure inside the CRZ bubble, and at $t \approx 68$ ms it goes over $P \approx P_{transition} = 101\,130$ Pa. At this instant, the pressure in the second half of the CRZ starts decreasing, and the mass flux towards the CRZ bubble starts to steeply increase, along with the pressure and volume of the CRZ bubble. The volume of the second half of the CRZ, which had a positive trend, presents a sudden decrease at this moment, a consequence of the mass transfer towards the CRZ bubble. After a while, however, it regains its increasing trend. The flame diameter closely follows the evolution of the CRZ bubble volume, increasing steeply as soon as the latter starts to expand at $t \approx 80$ ms, as shown in the image sequence of figure 9(*f*), 9(*g*), 9(*h*).

The final state exhibits a CRZ with a single conical part, characterised by uniform average temperature and pressure, as illustrated in figure 13(*a*) and 13(*b*). The mass flux inside the CRZ is also much higher for the CVB, due to the larger diameter of the conical CRZ.

The $P_{transition}$ criterion is then closely related to the instant when the volume of the CRZ bubble suddenly expands and starts changing towards a conical CRZ. It represents a criterion for the stability limits of the BVB mode; moreover, as soon as the depression

https://doi.org/10.1017/jfm.2025.10937 Published online by Cambridge University Press

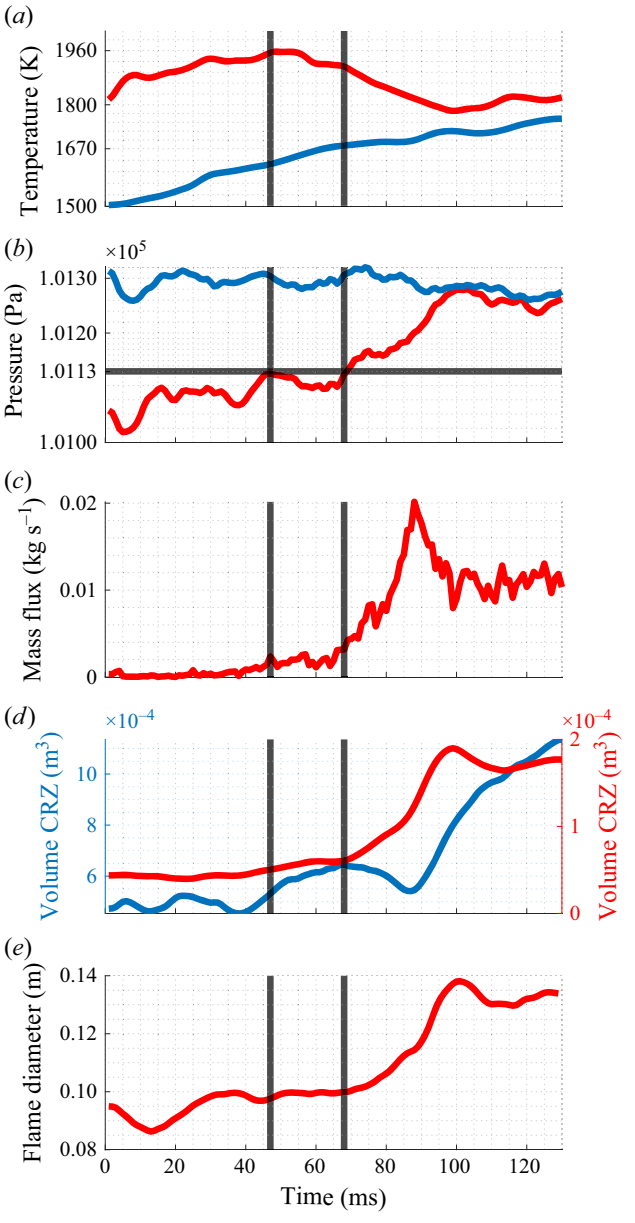


Figure 13. (*a*) Time evolution of average temperature inside the CRZ bubble (red) and the second half of the CRZ (blue). (*b*) Time evolution of average pressure inside the CRZ bubble (red) and the second half of the CRZ (blue). Black horizontal line corresponds to $P_{transition} = 101\,130$ Pa. (*c*) Time evolution of the mass flux between the second part of the CRZ towards the CRZ bubble measured at the bottleneck contraction position $x = 0.07$ m. (*d*) Time evolution of the volume of the CRZ bubble (red) and of the second half of the CRZ (blue). (*e*) Time evolution of flame diameter measured at the bottleneck contraction position $x = 0.07$ m. Vertical lines represent the time instants when $P = P_{transition}$. All signals are filtered with a second-order Butterworth low-pass filter with a cutoff frequency of 40 Hz.

https://doi.org/10.1017/jfm.2025.10937 Published online by Cambridge University Press

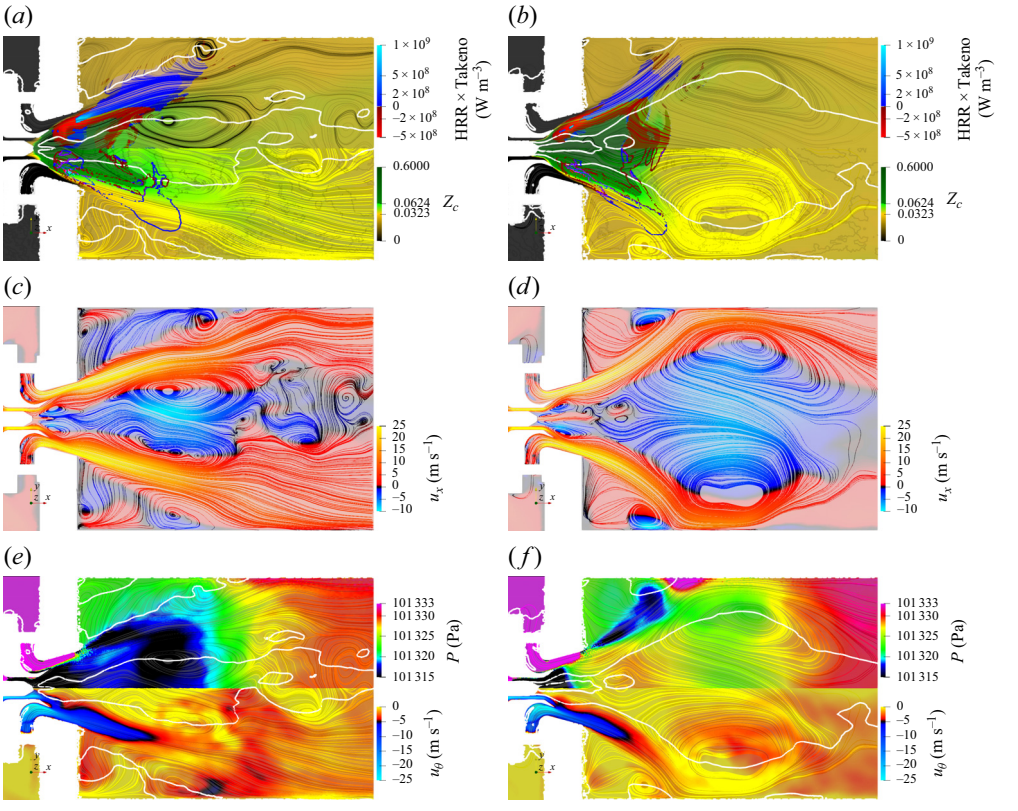


Figure 14. Large-eddy simulation results, time-averaged over 40 ms, of OP_{lp} tulip flame (*a*) positive HRR times the TI $HRR \times TI = HRR \cdot \nabla Y_{kerosene} \cdot \nabla Y_{O_2} / |\nabla Y_{kerosene} \cdot \nabla Y_{O_2}|$ (clipped to fit in the limits [−5e8; 1e9]), showing premixed combustion regions in blue and non-premixed ones in red, superposed to Bilger's carbon-defined mixture fraction; (*c*) axial velocity; and (*e*) pressure (top) and swirl velocity (bottom). Panels (*b*), (*d*) and (*f*) represent the same fields, respectively, for the OP_{lp} V flame. The flow is swirling clockwise (negative u_θ) with respect to the axial direction. The recirculation zones are shown in blue in figures (*c*) and (*d*) and by the white contour of $u = 0$m/s in the other panels.

inside the CRZ bubble is eliminated, the vortex breakdown mode changes towards a CVB mode. This shows yet again that the characteristic feature of the BVB mode is the depression in the centre of the bubble and that it is precisely this depression that maintains the bubble shape of the CRZ.

6. Discussion on BVB stability

After analysing this transition, several questions arise concerning the tulip-BVB and V-CVB flames and flow stability, as well as the application of the criterion to other operating conditions to evaluate its generalisation.

6.1. *Stability criterion applied to the OP_{lp} case*

A similar tulip-BVB to V-CVB transition is observed in the same burner, but for a low power operation, OP_{lp} presented in table 4, with the flame and flow shown in figure 14 before and after the transition. The triggering of this transition, however, is slightly different to the previous case. Instead of increasing the equivalence ratio after the tulip flame is stable, in this second case, the non-reacting case is already at OP_{lp}, so the flame

https://doi.org/10.1017/jfm.2025.10937 Published online by Cambridge University Press

is ignited already at $\phi = 0.7$. Thus, no boundary conditions are changed for this lower flow rate condition. We start tracking the flow once the ignition transient is fully flushed out and the flame is stable after 100 ms, as discussed in Mesquita *et al.* (2021*b*). We use this second case to test our pressure criterion, which is calculated in the same manner and is $P_{transition} \approx 101\,312$ Pa. An analysis of the transition is carried out, with the results summarised in figure 15. The pressure inside the CRZ bubble increases until reaching $P_{transition} \approx 101\,312$ Pa, at $t = 34$ ms. At this instant, the temperature begins to sharply decrease as the CRZ volume and the flame diameter increase significantly, marking the transition. Therefore, these results indicate that the pressure criterion for the BVB mode is achieved at a lower mass flow rate operating condition. Furthermore, this case shows that the BVB mode will transition not only if the operating conditions change to make the CRZ pressure higher than $P_{transition}$, but whenever the operating conditions result in a CRZ pressure over $P_{transition}$, even if the flame is not present yet. This reinforces the usefulness of the criterion in understanding the range of conditions where a tulip-BVB flame is stable.

6.2. *Stability criterion applied to the OP_2 case*

The $P_{transition}$ criterion is also evaluated by applying it to a third operating condition, now at a higher air mass flow rate and using the multipoint injection system, the OP_2 operating point in table 4. Unlike the other two points, under these operating conditions and numerical set-up, the tulip flame is stable; thus, the criterion should provide a higher $P_{transition}$ pressure than the average pressure inside the CRZ bubble. For the OP_2 tulip flame, the criterion gives $P_{transition} \approx 100\,940$ Pa, while the average pressure inside the CRZ bubble is $P = 100\,885$ Pa, which is lower than the $P_{transition}$. This is consistent with the stable tulip flame under these conditions and numerical set-up; therefore, the criterion is also able to characterise stable flames. However, one must note that the average pressure is very close to $P_{transition}$, suggesting that this flame and the BVB mode at these conditions are very close to their stability limits. Thus, they could easily transition with an increase in combustor temperature, due to an increase in equivalence ratio, a change in combustor wall temperature, a change in air inlet temperature, or a change in the staging factor, for example.

6.3. *Relationship between BVB mode stability and operating conditions*

To study the effect of the operating conditions on the BVB mode stability, figure 16 shows the evolution of both the CRZ average pressure and of $P_{transition}$ with the air mass flow rate for the three operating conditions OP_{lp}, OP_1 and OP_2. Increasing the mass flow rate intensifies the stability of the BVB mode, as the difference between the CRZ average pressure and $P_{transition}$ rises. This is a significant result, as it strengthens the theoretical basis behind the $P_{transition}$ stability criterion. Increasing the mass flow rate increases the swirl velocity, which then results in an increase in the CRZ depression. This creates a higher radial pressure gradient, which leads to a relatively higher $P_{transition}$ and improved stability for the BVB mode. Ultimately, this means that the BVB mode and a tulip flame can be stable for higher equivalence ratios (withstanding higher temperatures) for higher mass flow rates.

In opposition, figure 16 also shows that the BVB mode is not possible for a sufficiently low mass flow rate, as $P_{transition}$ decreases with decreasing air mass flow rate and becomes closer and closer to the CRZ average pressure. This is also in agreement with the previous discussion, as at some point, the swirl velocity is not high enough to create the CRZ depression or even vortex breakdown, as previously discussed and shown in various works,

https://doi.org/10.1017/jfm.2025.10937 Published online by Cambridge University Press

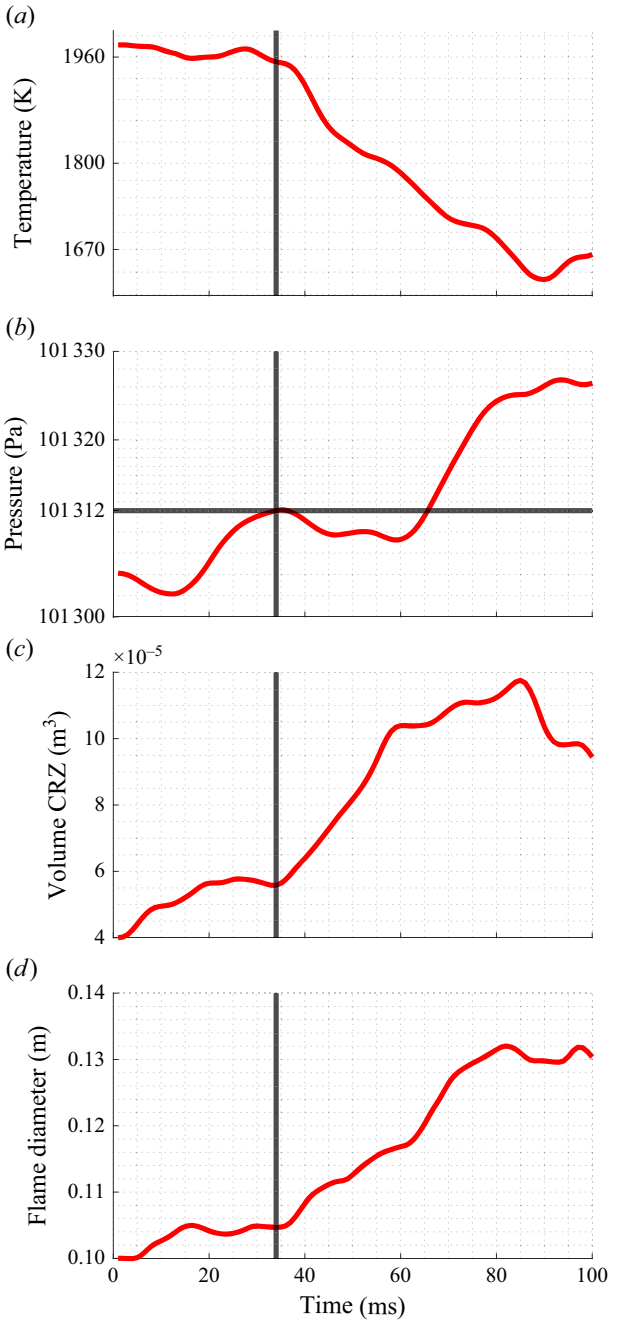


Figure 15. For OP_{lp}. (*a*) Time evolution of average temperature inside the CRZ bubble. (*b*) Time evolution of average pressure inside the CRZ bubble. Black horizontal line corresponds to $P_{transition} = 101\,312$ Pa. (*c*) Time evolution of the volume of the CRZ bubble. (*d*) Time evolution of flame diameter measured at the bottleneck contraction position $x = 0.07$ m. All signals are filtered with a second-order Butterworth low-pass filter with a cutoff frequency of 40 Hz.

https://doi.org/10.1017/jfm.2025.10937 Published online by Cambridge University Press

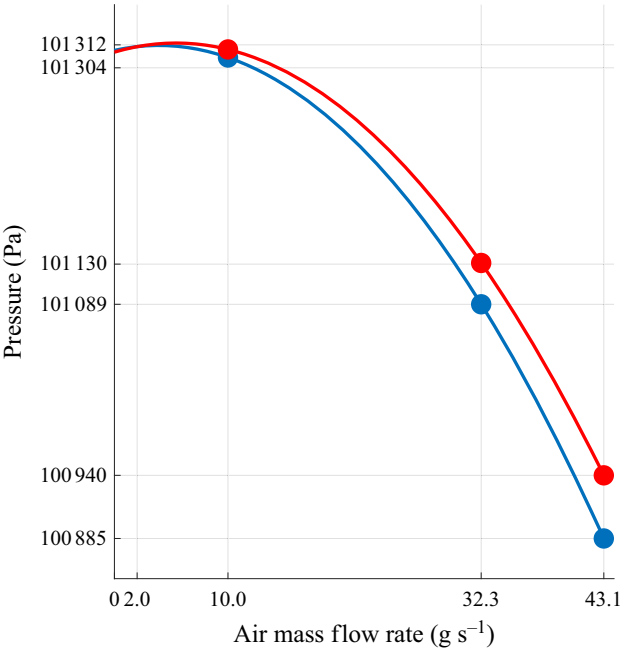


Figure 16. Evolution of the CRZ average pressure for BVB topology tulip flames (blue circles) and of $P_{transition}$ (red circles) with the air mass flow rate. Lines represent second-order polynomial fitting of the data.

including Lucca-Negro & O'Doherty (2001), Sarpkaya (1995) and Rajamanickam & Basu (2018).

Ultimately, figure 16 highlights that relying on a flame stabilised by the BVB mode in a real aero-engine presents its challenges. During operation, the air mass flow rate can vary significantly, thereby affecting the stability of the BVB flow and flame, and creating the requirement to ensure the flame and flow remain stable throughout the operation cycle. In particular, critical manoeuvres such as windmilling high-altitude relight, when the air mass flow rate can be significantly reduced, pose a risk to the stability of the BVB mode, potentially causing an unexpected flame shape transition and thus altering the operating characteristics of the combustor. Therefore, figure 16 illustrates that the flow topology and flame shape have to be carefully studied before being considered for an aero-engine application, having in mind the range of operating conditions and regimes.

6.4. *Stability criterion applied to the V flame CVB-to-BVB transition*

A question that quickly comes to mind is whether this BVB-to-CVB transition is reversible. Is it possible to go back to a tulip shape from the resulting V flame when the equivalence ratio is reduced again to $\phi = 0.5$? The answer is no: when the V flame is stabilised at the end of the previous transition and the equivalence ratio is reduced again to $\phi = 0.5$, the resulting flame is the OP_1 V flame presented in figure 6(d), with a flow field shown in figures 6(f) and 6(h). Once the flame stabilises in a V shape and the flow is in a CVB mode, both become very stable, and reducing the equivalence ratio to $\phi = 0.5$ is not sufficient to force the vortex breakdown mode back to a BVB mode. This indicates that once the hotter flame forces the BVB mode into a CVB mode, the CVB mode is responsible for the topology and flame stabilisation, rather than the higher CRZ temperature, which is merely the means to trigger the transition. However, this does not mean that reducing the equivalence ratio further, to a value lower than $\phi = 0.5$, could not

https://doi.org/10.1017/jfm.2025.10937 Published online by Cambridge University Press

eventually reverse the transition. Indeed, if we blow off the V flame, the non-reacting flow in the BIMER combustor reverts back to a BVB mode, showing that the flame and CRZ temperature have a role in stabilising the CVB mode, and that the reacting CVB mode might not be identical to a non-reacting CVB.

Nevertheless, a CVB to BVB mode transition for a value higher than the initial equivalence ratio of $\phi = 0.5$ was also observed in the BIMER combustion for the OP_2 operating conditions ($\phi = 0.6$); therefore, it is not linked with changes in temperature in the CRZ, but rather with a strong aerodynamic mechanism that is required to force the reverse CVB to BVB transition. This transition is described in detail in Mesquita *et al.* (2021*a*); still, for the sake of this discussion, it is interesting to mention that the CVB mode transitions to the BVB one when the CRZ boundaries are being pushed inwards by toroidal vortices formed in the ISL by longitudinal acoustic forcing. The vortices act then in two ways that lead to the transition: (i) reducing the diameter of the vortex core (i.e. the diameter of the swirling jet) intensifies the depression in the centre of the CRZ; and (ii) the vortices constrict the CRZ at its middle, reducing the recirculating flow towards the upstream-most portion of the CRZ, also intensifying the CRZ depression. Once the vortex is large enough, the CRZ depression is intense enough to attract the swirling jet inwards and stabilise the bubble-shaped CRZ and the BVB mode.

Therefore, the CVB to BVB transition is ultimately triggered by the opposite mechanism of the tulip-BVB to V-CVB transition presented here: the transition occurs when the pressure inside the CRZ falls below a certain value. This highlights that, once again, the pressure at the centre of the swirling vortex is crucial to determine the vortex breakdown mode and the flow topology in the presence of a flame. Thus, it is also interesting to apply the pressure stability criterion to the CVB-BVB case to assess the validity of the methodology in the opposite CVB-to-BVB transition. In this case, however, as we evaluate the limit when the flow begins to accelerate inwards, the transition occurs when

$$P_{axis} < P_{transition} = P_{swirling\,jet} - \rho u^2_{\theta,swirling\,jet}. \tag{6.1}$$

Similarly to the BVB to CVB transition, $P_{transition}$ is calculated over the swirling jet in the vicinity of the CRZ for the stable OP_2 $\alpha = 15\,\%$ V flame. This results in $P_{transition} \approx 101\,200$ Pa. Figure 17 plots the time evolution of the average pressure inside the CRZ for the CVB to BVB transition. The pressure inside the CRZ is at first almost constant. However, it starts decreasing when the toroidal vortices become sufficiently large not only to make the swirling jet oscillate but to progressively decrease the CRZ radius, triggering the mechanism described in the previous paragraph and reducing the pressure inside the CRZ. Once the pressure becomes inferior to $P_{transition} \approx 101\,200$ Pa, the radial balance between centrifugal force and radial pressure gradient becomes negative (as shown in Mesquita *et al.* 2021*a*) and the transition is triggered. After that, the pressure drops significantly and the flow moves to a BVB mode. These results show that the $P_{transition}$ pressure criterion also yields sensible results for the CVB-to-BVB transition, indicating that the pressure at the centre of the swirling vortex is characteristic of each mode and that the CRZ pressure change is characteristic of the transition in both directions.

If we return to the initial question of whether reducing the equivalence ratio can reverse the BVB to CVB transition, we see that for the CVB mode, the pressure inside the CRZ does not decrease considerably once the equivalence ratio is reduced to $\phi = 0.5$; only the temperature inside the CRZ decreases. A reduction in pressure inside the CRZ is the essential phenomenon that forces the CVB towards the BVB transition; therefore, without a forced reduction in pressure inside the CRZ, the CVB mode remains stable. Indeed, if one analyses figure 13(*b*), one can see that the final pressure is higher in the CRZ after the transition to the CVB mode, but not due to an increase in temperature, as the final average

https://doi.org/10.1017/jfm.2025.10937 Published online by Cambridge University Press

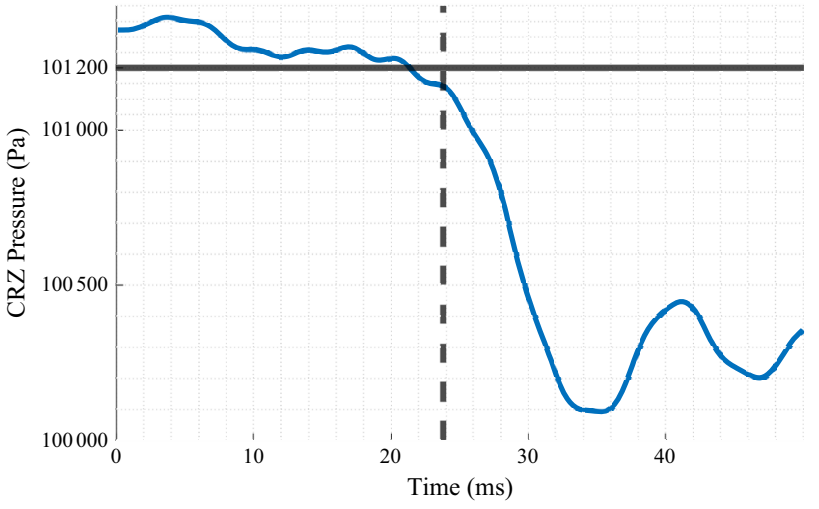


Figure 17. Time evolution of the average pressure inside the CRZ for the OP_2 CVB-to-BVB transition. Black horizontal line corresponds to $P_{transition} \approx 101\,200$ Pa. The signal is filtered with a 4th-order Butterworth low-pass filter with a cutoff frequency of 80 Hz. The dashed vertical line identifies the moment at which the inner flame has merged in the CRZ.

temperature inside the CVB CRZ decreases at the end of the transition. This indicates that the higher pressure inside the CRZ for the CVB mode compared with the BVB mode is a consequence of the aerodynamics of the mode itself. Therefore, once the CVB mode is stabilised, there is an aerodynamic mechanism that keeps that mode stable and prevents the pressure from decreasing, even if the equivalence ratio is reduced back to $\phi = 0.5$. We can then use the aerodynamic characteristics of each mode to try to understand why the transition is not reversible.

The bubble mode is stable because the swirling jet creates a depression at the axis of rotation that attracts itself, and, as the central depression attracts the swirling flow inside, it strangles the CRZ. Thus, this strangulation of the CRZ bubble limits the recirculating mass flux from the back of the combustor towards the bubble, ensuring the pressure inside the CRZ remains low and making most of the air that recirculates inside the bubble come primarily from the swirling jet, rather than from the back of the combustor. In this manner, the recirculating flow inside the bubble is primarily composed of swirling flow, which reinforces the creation of a negative radial pressure gradient within the bubble, ensuring that the swirling flow remains attracted inside.

For the reacting CVB, as illustrated by the velocity and pressure profiles in § 5.2, the recirculating flow does not rotate, likely because the gas recirculates much farther downstream when most of its swirling momentum has dissipated. Thus, the local negative radial pressure gradient created by the jet swirling motion at the CRZ boundary is compensated by a purely axial flow and not a swirling flow, which does not induce a constantly decreasing pressure towards the axis inside the vortex. In the reacting CVB mode, then, the local negative radial pressure gradient in the swirling jet is used to radially and tangentially accelerate the recirculating flow as it merges with the swirling jet in the ISL, as shown in the velocity profiles in figure 7(f) and 7(h) and illustrated by the schematics in figure 18. The CVB axial flow in the CRZ reduces the total radial pressure gradient at the swirling jet level compared with the BVB mode; therefore, as there is no negative radial pressure attraction from the CRZ (plus the effect of dilatation from combustion and entrainment created by the jet), the swirling jet moves outwards

https://doi.org/10.1017/jfm.2025.10937 Published online by Cambridge University Press

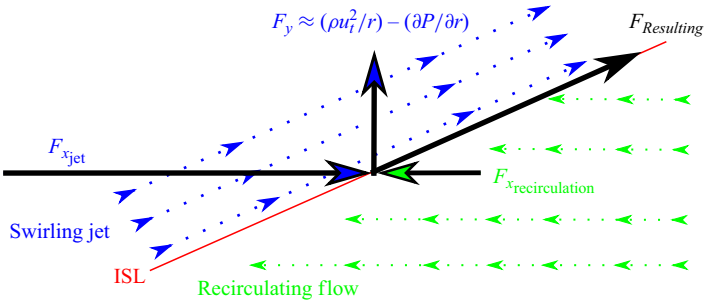


Figure 18. Schematics showing the forces acting at a fluid particle moving from the recirculating gas to the swirling jet in the CVB mode. The recirculating flow is accelerated radially by the centrifugal effect of the swirling jet.

in a conical trajectory by centrifugal acceleration. Simultaneously, the conical shape of the topology allows a higher recirculating mass flow to continuously 'feed' the radially expanding swirling jet, preserving continuity, as the purely axial flow recirculates upstream in the CRZ. These characteristics ensure that the CVB swirling jet remains stable in its conical trajectory, allowing the reacting CVB mode to create the aerodynamic stabilisation mechanisms that ensure stability with a margin of independence from CRZ temperature, and maintain the CVB mode stable for $\phi = 0.5$.

6.5. *Discussion on the need for a more detailed flame shape nomenclature and a flame shape transitions typology: pure flame or flow–flame shape transitions?*

In the literature review presented in this work, we showed that there is often no significant distinction between a flame shape transition and a flow topology transition that leads to a flame shape transition. However, this work has shown that, in some cases, a change in flow topology is precisely the cause of the flame shape transition, although this is not systematically accounted for. This oversight likely occurs because only the change in flame shape is often visible, thus capturing the attention of researchers and engineers.

The significance of flow topology becomes particularly evident when we apply the flame shape nomenclature from table 1 to compare different flame shapes. As illustrated by the transition discussed in this work, the difference between a tulip flame (BVB/S-ISL) and a V flame (CVB/S-ISL) lies in the vortex breakdown mode. This distinction highlights the important role of flow topology in flame shape transitions. Therefore, we argue that using the nomenclature of table 1 could be beneficial in identifying all the stabilisation mechanisms for a given flame, highlighting clearly which one changes when the flame transitions from one shape to another. Furthermore, the cases presented in this work emphasise the need for a clear distinction in describing flame shape transitions when (i) only the flame transitions to when (ii) the flow topology change correlates with the flame shape change, regardless of causality. Thus, we also propose a typology to classify:

(i) a flame shape transition when only the flame shape changes, with the flow remaining in the same topology, as a pure flame shape transition. Examples of this transition are the tulip (figure 2*c*) to M (figure 2*e*) transition, as in Renaud *et al.* (2015*b*) and Mesquita *et al.* (2023*a*), or ISL to OSL transitions, as in tulip OP_1 (figure 2*a*) to tulip OP_2 (figure 2*c*) in Taamallah *et al.* (2015*b*, 2016) and Foley *et al.* (2017) or likely the ones in Huang & Yang (2004) and Han *et al.* (2018, 2019, 2020);

https://doi.org/10.1017/jfm.2025.10937 Published online by Cambridge University Press

(ii) a flame shape transition that correlates with a flow topology change as a flow–flame shape transition. Examples of this transition are the one in this work, the V (figure 2*f*) to M (figure 2*e*) of (Mesquita *et al.* 2021*a*), and likely the ones in Chterev *et al.* (2014), Terhaar *et al.* (2014), Hermeth *et al.* (2014), Guiberti *et al.* (2015), Santhosh & Basu (2016), Malbois *et al.* (2017), Taamallah *et al.* (2019), Degeneve *et al.* (2019), Langella *et al.* (2019), Domingo-Alvarez *et al.* (2020), Legros *et al.* (2021), Soli & Langella (2022) and Tomasch *et al.* (2025).

We believe these nomenclatures can help connect mechanisms across different studies and facilitate comparisons between research from various groups, potentially revealing more universal mechanisms driving flame shape transitions.

7. Conclusions

This work investigated, using LES, the transition from a tulip flame shape (BVB/S-ISL flame, as per the nomenclature adopted in this work) stabilised over a BVB to a V flame shape (CVB/S-ISL flame) stabilised over a CVB. The transition is triggered when the equivalence ratio is increased from $\phi = 0.5$ to $\phi = 0.7$.

Following the increase in equivalence ratio, a constant increase in temperature inside the combustion chamber is observed. Simultaneously, the pressure inside the CRZ bubble increases, while the average pressure inside the combustion chamber remains mostly constant. The change in flame shape was then correlated with this increase in pressure. These phenomena brought our attention to the CRZ dynamics. It was observed that the two parts of the 'hourglass-shaped' CRZ present for the tulip BVB flame show different characteristics and behaviour. The increase in temperature triggers the CRZ to open, creating a higher recirculating mass flux to compensate for the depression created by the swirling jet, allowing the vortex to expand radially in a conical path and stabilise a CVB mode. These results are in line with the observations of Billant *et al.* (1998), which stated that both BVB and CVB appeared at the same swirl level, but a temperature difference was responsible for the appearance of one mode over the other. Here, we demonstrate that an increase in temperature is responsible for triggering the change in vortex breakdown mode. A criterion for a limit pressure inside the CRZ was then devised based on the radial momentum equation and the balance between centrifugal force and radial pressure gradient, found to control the radial motion of the CRZ. This criterion helped understand the main events of the transition, showing that once the pressure inside the CRZ went over the limit $P_{transition}$ given by the criterion, the flow topology changed from a BVB mode to a CVB mode, forcing then the change in flame shape from a tulip flame (BVB/S-ISL flame) to a V (CVB/S-ISL flame).

Therefore, a significant achievement of this work is the identification of a novel mechanism for the controlled transition of the vortex breakdown mode. In the literature, controlled BVB to CVB transitions are only achieved by direct flow modifications, either by increasing the Reynolds number (Sarpkaya 1995) or the ratio of swirl and axial motion in co-axial flows (Santhosh *et al.* 2014; Terhaar *et al.* 2015; Rajamanickam & Basu 2018; Moise & Mathew 2019; Moise 2020; Moise & Mathew 2021; Douglas *et al.* 2022; Keeton *et al.* 2022). In this case, the flow properties remain unchanged; the increase in fuel mass flow rate does not result in significant alterations to the flow field. As a result, only the equivalence ratio increases, which causes the flame, stabilised by the ISL, to burn more intensely, subsequently raising the CRZ temperature. These results demonstrate how the increase in temperature within the combustion chamber, resulting from the increase in equivalence ratio, leads to a corresponding rise in pressure inside the CRZ bubble, thereby indicating a case of combustion-driven vortex breakdown mode transition. The results

https://doi.org/10.1017/jfm.2025.10937 Published online by Cambridge University Press

also showed that, in this case, the flame shape is completely symbiotic with the vortex breakdown mode, changing its shape to a V flame as a consequence of the change from a BVB to a CVB.

Furthermore, these results demonstrate for the first time that in reacting flows, the CRZ being in depression is a characteristic and exclusive feature of the BVB mode, as the vortex breakdown mode changes when the depression ceases due to an increase in temperature. This is a feature that has not been discussed in the literature to the best of the authors' knowledge, as most BVB-CVB comparison studies were either experimental or non-reacting or did not involve pressure measurements. Therefore, a major criterion for differentiating the BVB from the CVB mode is the strong negative radial pressure gradient between the CRZ and the swirling jet, which is present only in the BVB mode. This criterion can then be applied to the design of aeronautical combustors and injectors, where the stability of a BVB mode can be assessed based on the range of equivalence ratios, temperatures and air mass flow during operation.

Additionally, it was demonstrated that, for the reacting CVB mode, the absence of depression inside the CRZ, the absence of rotating motion in the recirculating flow and the increase in the flux of recirculating gases due to the conical shape are important mechanisms to sustain the open CRZ and the topology, along with the flame itself and the hot gases in the CRZ. These aerodynamic mechanisms provide the CVB mode with some independence from reductions in CRZ temperature, thereby maintaining the CVB mode stable when the equivalence ratio is reduced again to $\phi = 0.5$, creating an hysteresis and bi-stability, as the transition is not immediately reversible. Thus, this work also raises awareness of the stability limits of cases where the reacting flow is not the same as the non-reacting one, showing, for example, that a design aiming to rely on this CVB mode V flame needs to ideally also have a non-reacting CVB topology, or ensure a range of equivalence ratios and operating conditions where the CVB mode and V flame are stable.

Finally, to compare the flame shapes and transitions discussed in the literature with those observed in this study, we propose a detailed nomenclature for flame shapes. This nomenclature focuses on the mechanisms that stabilise the flame, rather than relying solely on subjective interpretations of its appearance. We also proposed a categorisation of flame shape transitions into two types: a pure flame shape transition, which occurs when the flame shape changes without any alteration in flow topology, and a flow–flame shape transition, which happens when the change in flame shape is associated with a change in flow topology. We believe that these nomenclatures can help the community connect mechanisms across various research works and facilitate the comparison of studies from different groups, thereby helping to reveal more general mechanisms that drive flame shape transitions.

Acknowledgements. We thank CERFACS for sharing the AVBP solver.

Funding. This work was granted access to the HPC resources of CINES under the allocation A0012B00164 made available by GENCI, and of the mesocentre computing centre of CentraleSupélec and Ecole Normale Supérieure Paris-Saclay supported by CNRS and Region Ile-de-France (http://mesocentre.centralesupelec.fr/). We finally thank CentraleSupélec and Université Paris-Saclay for L.C.C.M's PhD. grant.

Declaration of interests. The authors report no conflict of interest.

References

Abramzon, B. & Sirignano, W.A. 1989 Droplet vaporization model for spray combustion calculations. *Intl J. Heat Mass Transfer* **32**, 1605–1618.

Agostinelli, P.W., Laera, D., Chterev, I., Boxx, I., Gicquel, L. & Poinsot, T. 2022 On the impact of H2-enrichment on flame structure and combustion dynamics of a lean partially-premixed turbulent swirling flame. *Combust. Flame* **241**, 112120.

https://doi.org/10.1017/jfm.2025.10937 Published online by Cambridge University Press

ALEKSEENKO, S.V., DULIN, V.M., KOZOREZOV, Y.S., MARKOVICH, D.M., SHTORK, S.I. & TOKAREV, M.P. 2011 Flow structure of swirling turbulent propane flames. *Flow, Turbul. Combust.* **87** (4), 569–595.

ANGELBERGER, D., VEYNANTE, D., EGOLGOPOULOS, F. & POINSOT, T. 1998 Large eddy simulations of combustion instabilites in premixed flames. In *Proceedings of the Summer Program*, pp. 61–82.

ARNDT, C.M., STEINBERG, A.M., BÖHNKE, J., HADEF, R. & MEIER, W. 2019 High speed imaging of flame structure and dynamic processes in swirl stabilized prevaporized liquid fuel flames. In *AIAA Scitech 2019 Forum*. American Institute of Aeronautics and Astronautics.

BAE, J., ARDEBILI, Y.N., VENA, P. & CHAUDHURI, S. 2024 Effect of swirler spin on flame shape and combustion dynamics. *Proc. Combust. Inst.* **40** (1), 105663.

BILLANT, P., CHOMAZ, J.-M. & HUERRE, P. 1998 Experimental study of vortex breakdown in swirling jets. *J. Fluid Mech.* **376**, 183–219.

BOILEAU, M. 2007 Simulation aux grandes échelles de l'allumage diphasique des foyers aéronautiques. PhD thesis, INP Toulouse.

BROWN, G.L. & LOPEZ, J.M. 1990 Axisymmetric vortex breakdown Part 2. Physical mechanisms. *J. Fluid Mech.* **221**, 553–576.

BUTLER, T. & O'ROURKE, P. 1977 A tabulated chemistry method for spray combustion. In *International Symposium on Combustion*, vol. 16, pp. 1503–1515.

CANDEL, S., DUROX, D., SCHULLER, T., BOURGOUIN, J.F. & MOECK, J.P. 2014 Dynamics of swirling flames. *Annu. Rev. Fluid Mech.* **46**, 147–176.

CARNEIRO PITON, L., SENRA PESSANHA RIOS NOBREGA, G., FIGUEIRA DA SILVA, L.F., SCOUFLAIRE, P. & DARABIHA, N. 2020 Experimental study of the influence of the swirl number on lean premixed combustion regimes. *J. Braz. Soc. Mech. Sci. Engng* **42** (4), 210.

CHARLETTE, F., MENEVEAU, C. & VEYNANTE, D. 2002 A power-law flame wrinkling model for LES of premixed turbulent combustion Part II: dynamic formulation. *Combust. Flame* **131** (1–2), 181–197.

CHENEAU, B. 2019 étude numérique de la dynamique de combustion dans un bruleur diphasique turbulent à deux étages. PhD thesis, Université Paris-Saclay.

CHENEAU, B., VIÉ, A. & DUCRUIX, S. 2015 Large eddy simulations of a liquid fuel swirl burner: Flame characterization for pilot and multipoint injection strategies. In *GT2015-42821. In Proceedings of the ASME 2015: Turbine Technical Conference and Exposition*, Montréal, Canada.

CHENEAU, B., VIÉ, A. & DUCRUIX, S. 2019*a* Characterization of the hysteresis cycle in a two-stage liquid-fueled swirled burner through numerical simulation. *Proce. Combust. Inst.* **37**, 5245–5253.

CHENEAU, B., VIÉ, A. & DUCRUIX, S. 2019*b* Numerical study of flame shapes and structures in a two-stage two-injection Aeronautical burner with variable fuel staging using Eulerian large eddy simulations. *ASME. J. Eng. Gas Turbines Power* **141** (7), 071014.

CHONG, C.T., LAM, S.S. & HOCHGREB, S. 2016 Effect of mixture flow stratification on premixed flame structure and emissions under counter-rotating swirl burner configuration. *Appl. Therm. Engng* **105**, 905–912.

CHTEREV, I. *et al.* 2014 Flame and flow topologies in an annular swirling flow. *Combust. Sci. Technol.* **186** (8), 1041–1074.

CIARDIELLO, R., SKIBA, A.W., GORDON, R.L. & MASTORAKOS, E. 2020 Experimental assessment of the lean blow-off in a fully premixed annular combustor. *Exp. Therm. Fluid Sci.* **112**, 109994.

COLIN, O., DUCROS, F., VEYNANTE, D. & POINSOT, T. 2000 A thickened flame model for large Eddy simulations of turbulent premixed combustion. *Phys. Fluids* **12**, 1843–1863.

COLIN, O. & RUDGYARD, M. 2000 Development of high-order Taylor–Galerkin schemes for LES. *J. Comput. Phys.* **162** (2), 338–371.

DAGAN, Y., ARAD, E. & TAMBOUR, Y. 2015 On the dynamics of spray flames in turbulent flows. *Proc. Combust. Inst.* **35** (2), 1657–1665.

DAGAN, Y., ARAD, E. & TAMBOUR, Y. 2016 The evolution of local instability regions in turbulent non-premixed flames. *J. Fluid Mech.* **803**, 18–50.

DEGENEVE, A., MIRAT, C., CAUDAL, J., VICQUELIN, R. & SCHULLER, T. 2019 Effects of swirl on the stabilization of non-premixed oxygen-enriched flames above coaxial injectors. *J. Engng Gas Turbines Power* **141** (12), 121018.

DODDS, W.J. & BAHR, D.W. 1990 *Design of Modern Gas Turbine Combustors*. Academic Press.

DOMINGO-ALVAREZ, P., BÉNARD, P., MOUREAU, V., LARTIGUE, G. & GRISCH, F. 2020 Impact of spray droplet distribution on the performances of a kerosene lean/Premixed injector. *Flow, Turbul. Combust.* **104** (2–3), 421–450.

DOUGLAS, C.M., EMERSON, B.L. & LIEUWEN, T.C. 2022 Dynamics and bifurcations of Laminar annular swirling and non-swirling jets. *J. Fluid Mech.* **943**, A35.

https://doi.org/10.1017/jfm.2025.10937 Published online by Cambridge University Press

DRISCOLL, J. & TEMME, J. 2011 Role of Swirl in Flame Stabilization. In *49th AIAA Aerospace Sciences Meeting including the New Horizons Forum and Aerospace Exposition*. American Institute of Aeronautics and Astronautics.

DURBIN, M.D., VANGSNESS, M.D., BALLAL, D.R. & KATTA, V.R. 1996 Study of flame stability in a step swirl combustor. *J. Engng Gas Turbines Power* **118** (2), 308–315.

DUROX, D., MOECK, J.P., BOURGOUIN, J.-F., MORENTON, P., VIALLON, M., SCHULLER, T. & CANDEL, S. 2013 Flame dynamics of a variable swirl number system and instability control. *Combust. Flame* **160** (9), 1729–1742.

FIORINA, B. *et al.* 2016 Modeling challenges in combusting aeronautical combustion chambers. *Aerospace Lab* **11**, 19.

FOLEY, C., CHTEREV, I., NOBLE, B., SEITZMAN, J. & LIEUWEN, T. 2017 Shear layer flame stabilization sensitivities in a swirling flow. *Intl J. Spray Combust. Dyn.* **9** (1), 3–18.

FRANZELLI, B., RIBER, E., SANJOSÉ, M. & POINSOT, T. 2010 A two-step chemical scheme for kerosene–air premixed flames. *Combust. Flame* **157** (7), 1364–1373.

GUIBERTI, T.F., DUROX, D., ZIMMER, L. & SCHULLER, T. 2015 Analysis of topology transitions of swirl flames interacting with the combustor side wall. *Combust. Flame* **162** (11), 4342–4357.

HAN, X., LAERA, D., MORGANS, A.S., LIN, Y. & SUNG, C.-J. 2018 The effect of stratification ratio on the macrostructure of stratified swirl flames: experimental and numerical study. *J. Engng Gas Turbines Power* **140** (12), 121004.

HAN, X., LAERA, D., MORGANS, A.S., SUNG, C.J., HUI, X. & LIN, Y.Z. 2019 Flame macrostructures and thermoacoustic instabilities in stratified swirling flames. *Proc. Combust. Inst.* **37** (4), 5377–5384.

HAN, X., LAERA, D., YANG, D., ZHANG, C., WANG, J., HUI, X., LIN, Y., MORGANS, A.S. & SUNG, C.-J. 2020 Flame interactions in a stratified swirl burner: flame stabilization, combustion instabilities and beating oscillations. *Combust. Flame* **212**, 500–509.

HANNEBIQUE, G., SIERRA, P., RIBER, E. & CUENOT, B. 2013 Large eddy simulation of reactive two-phase flow in an aeronautical multipoint burner. *Flow, Turbul. Combust.* **90**, 449–469.

HARVEY, J.K. 1962 Some observations of the vortex breakdown phenomenon. *J. Fluid Mech.* **14** (4), 585–592.

HERMETH, S., STAFFELBACH, G., GICQUEL, L.Y.M., ANISIMOV, V., CIRIGLIANO, C. & POINSOT, T. 2014 Bistable swirled flames and influence on flame transfer functions. *Combust. Flame* **161** (1), 184–196.

HUANG, Y. & YANG, V. 2004 Bifurcation of flame structure in a lean-premixed swirl-stabilized combustor: transition from stable to unstable flame. *Combust. Flame* **136** (3), 383–389.

HUANG, Y. & YANG, V. 2005 Effect of swirl on combustion dynamics in a lean-premixed swirl-stabilized combustor. *Proc. Combust. Inst.* **30** (2), 1775–1782.

HUANG, Y. & YANG, V. 2009 Dynamics and stability of lean-premixed swirl-stabilized combustion. *Prog. Energ. Combust. Sci.* **35** (4), 293–364.

IDAHOSA, U., SAHA, A., XU, C. & BASU, S. 2009 Characterization of Combustion Dynamics in Swirl Stabilized Flames. In *ASME. (2009). Power Conference*. pp. 517–531. ASMEDC.

JAEGLE, F. 2009 Large eddy simulation of evaporating sprays in complex geometries using eulerian and lagrangian methods. PhD thesis, Institut Polytechnique de.

KALLIFRONAS, D.P., AHMED, P., MASSEY, J.C., TALIBI, M., DUCCI, A., BALACHANDRAN, R. & SWAMINATHAN, N. 2023 Scaling of flame describing functions in premixed swirling flames. *Flow, Turbul. Combust.* **111** (3), 929–951.

KEETON, B.W., CARPIO, J., NOMURA, K.K., SÁNCHEZ, A.L. & WILLIAMS, F.A. 2022 Vortex breakdown in variable-density gaseous swirling jets. *J. Fluid Mech.* **936**, A1.

KONLE, M. & SATTELMAYER, T. 2009 Interaction of heat release and vortex breakdown during flame flashback driven by combustion induced vortex breakdown. *Exp. Fluids* **47** (4-5), 627–635.

KRAUSE, E. 1985 A contribution to the problem of vortex breakdown. *Comput. Fluids* **13**, 375–381.

KUO, K.K. & ACHARYA, R. 2012 *Fundamentals of Turbulent and Multiphase Combustion: Kuo/Fundamentals of Turbulent Multi-Phase Combustion*. John Wiley & Sons, Inc.

LANGELLA, I., HEINZE, J., BEHRENDT, T., VOIGT, L., SWAMINATHAN, N. & ZEDDA, M. 2019 Turbulent flame shape switching at conditions relevant for gas turbines. *J. Eng. Gas Turbines Power* **142** (1), 011026.

LEFEBVRE, A.H. & BALLAL, D.R. 2010 *Gas Turbine Combustion*, 3rd edn. Taylor and Francis.

LEFEBVRE, A.H. 1980 Airblast atomization. *Prog. Energy Combust.* **6** (3), 233–261.

LEGIER, J.P., POINSOT, T. & VEYNANTE, D. 2000 Dynamically thickened flame LES model for premixed and non-premixed combustion. In *Proceedings of the Summer Program, Center for Turbulence Research*, NASA, Ames/Stanford University.

LEGROS, S., *et al.* 2021 Combustion for aircraft propulsion: progress in advanced laser-based diagnostics on high-pressure kerosene/air flames produced with low-NOx fuel injection systems. *Combust. Flame* **224**, 273–294.

https://doi.org/10.1017/jfm.2025.10937 Published online by Cambridge University Press

LOPEZ, J.M. 1990 Axisymmetric vortex breakdown Part 1. Confined swirling flow. *J. Fluid Mech.* **221**, 533–552.

LUCCA-NEGRO, O. & O'DOHERTY, T. 2001 Vortex breakdown: a review. *Prog. Energy Combust.* **27**, 431–481.

MALBOIS, P., SALAUN, E., FRINDT, F., CABOT, G., RENOU, B., GRISCH, F., BOUHERAOUA, L., VERDIER, H. & RICHARD, S. 2017 *Experimental Investigation With Optical Diagnostics of a Lean-Premixed Aero-Engine Injection System Under Relevant Operating Conditions*. American Society of Mechanical Engineers Digital Collection.

MARKOVICH, D.M., ABDURAKIPOV, S.S., CHIKISHEV, L.M., DULIN, V.M. & HANJALIĆ, K. 2014 Comparative analysis of low- and high-swirl confined flames and jets by proper orthogonal and dynamic mode decompositions. *Phys. Fluids* **26** (6), 065109.

MESQUITA, L.C.C. 2021 Simulation and analysis of the shape, performance and stability of flames in a two-stage lean-burn aeronautical combustor. PhD thesis, Université Paris-Saclay.

MESQUITA, L.C.C., VIÉ, A., ZIMMER, L. & DUCRUIX, S. 2021*a* Numerical analysis of flame shape bifurcation in a two-stage swirled liquid burner using large eddy simulation. *Proc. Combust. Inst.* **38** (4), 5971–5978.

MESQUITA, L.C.C., VIÉ, A. & DUCRUIX, S. 2017 Two-phase flow large eddy simulations of a staged multipoint swirling burner: comparisons between euler-euler and euler-lagrange descriptions. GT2017-64489. In *Proceedings of the ASME 2017: Turbine Technical Conference and Exposition*, Charlotte, NC, USA.

MESQUITA, L.C.C., VIÉ, A. & DUCRUIX, S. 2018 Large eddy simulations of a two-phase staged swirling burner using an euler-lagrange approach: validation of the injection strategy. GT2018-76125. In *Proceedings of the ASME Turbo Expo, 2018*, Oslo, Norway.

MESQUITA, L.C.C., VIÉ, A. & DUCRUIX, S. 2021*b* *LES of the Ignition of a Two-Phase Staged Swirling Burner: Influence of Ignition Location and Operating Conditions On the Flame Shape*. American Society of Mechanical Engineers Digital Collection.

MESQUITA, L.C.C., VIÉ, A. & DUCRUIX, S. 2023*a* Flashback-induced flame shape transition in a two-stage LPP aeronautical combustor. *Proc. Combust. Inst.* **39** (4), 4781–4790.

MESQUITA, L.C.C., VIÉ, A. & DUCRUIX, S. 2023*b* Numerical analysis of flame shape impact on the performance of fuel staging in a lean-burn aeronautical burner. *J. Engng Gas Turbines Power* **146** (4), 041003.

MOISE, P. 2020 Bistability of bubble and conical forms of vortex breakdown in Laminar swirling jets. *J. Fluid Mech.* **889**, A31.

MOISE, P. & MATHEW, J. 2019 Bubble and conical forms of vortex breakdown in swirling jets. *J. Fluid Mech.* **873**, 322–357.

MOISE, P. & MATHEW, J. 2021 Hysteresis and turbulent vortex breakdown in transitional swirling jets. *J. Fluid Mech.* **915**, A94.

NICOUD, F. & DUCROS, F. 1999 Subgrid-scale stress modelling based on the square of the velocity gradient tensor. *Flow, Turbul. Combust.* **62** (3), 183–200.

NOGENMYR, K.-J., PETERSSON, P., BAI, X.S., FUREBY, C., COLLIN, R., LANTZ, A., LINNE, M. & ALDÉN, M. 2011 Structure and stabilization mechanism of a stratified premixed low swirl flame. *Proc. Combust. Inst.* **33** (1), 1567–1574.

OBERLEITHNER, K., SIEBER, M., NAYERI, C.N., PASCHEREIT, C.O., PETZ, C., HEGE, H.-C., NOACK, B.R. & WYGNANSKI, I. 2011 Three-dimensional coherent structures in a swirling jet undergoing vortex breakdown: stability analysis and empirical mode construction. *J. Fluid Mech.* **679**, 383–414.

OBERLEITHNER, K., STÖHR, M., IM, S.H., ARNDT, C.M. & STEINBERG, A.M. 2015 Formation and flame-induced suppression of the precessing vortex core in a swirl combustor: experiments and linear stability analysis. *Combust. Flame* **162** (8), 3100–3114.

O'CONNOR, J. & LIEUWEN, T. 2012 Recirculation zone dynamics of a transversely excited swirl flow and flame. *Phys. Fluids* **24** (7), 075107.

PAPAFILIPPOU, N., CHISHTY, M.A. & GEBART, R. 2022 On the flame shape in a premixed swirl stabilised burner and its dependence on the laminar flame speed. *Flow, Turbul. Combust.* **108** (2), 461–487.

PARRA-SANTOS, M.T., MENDOZA-GARCIA, V., SZASZ, R., GUTKOWSKI, A.N. & CASTRO-RUIZ, F. 2015 Influence of flow swirling on the aerothermodynamic behaviour of flames. *Combust. Explosion Shock Waves* **51** (4), 424–430.

PAULHIAC, D. 2015 Modélisation de la combustion d'un spray dans un bruleur aéronautique. PhD thesis, Institut National Polytechnique de Toulouse.

POINSOT, P. & VEYNANTE, D. 2012 *Theoretical and Numerical Combustion*, 3rd edn. e-learning@CERFACS.

https://doi.org/10.1017/jfm.2025.10937 Published online by Cambridge University Press

POINSOT, T. & LELE, S. 1992 Boundary conditions for direct simulations of compressible viscous flows. *J. Comput. Phys.* **101** (1), 104–129.
PROVIDAKIS, T. 2013 Compétition entre structures aérodynamiques et modes acoustiques dans une flamme swirlée: influence de la répartition de carburant. PhD thesis, Ecole Centrale Paris.
RAJAMANICKAM, K. & BASU, S. 2018 Insights into the dynamics of conical breakdown modes in coaxial swirling flow field. *J. Fluid Mech.* **853**, 72–110.
RENAUD, A. 2015 High-speed diagnostics for the study of flame stabilization and transient behaviour in a swirled burner with variable liquid-fuel distribution. PhD thesis, CentraleSupélec.
RENAUD, A., DUCRUIX, S., SCOUFLAIRE, P. & ZIMMER, L. 2015*a* Experimental study of the interactions between air flow rate modulations and PVC in a swirl-stabilised liquid fuel burner. v04at04a063. In *Proceedings of the ASME 2015: Turbine Technical Conference and Exposition*, Montréal, Canada.
RENAUD, A., DUCRUIX, S., SCOUFLAIRE, P. & ZIMMER, L. 2015*b* Flame shape transition in a swirl stabilised liquid fueled burner. *Proc. Combust. Inst.* **35**, 3365–3372.
RENAUD, A., DUCRUIX, S. & ZIMMER, L. 2017 Bistable behaviour and thermo-acoustic instability triggering in a gas turbine model combustor. *Proc. Combust. Inst.* **36**, 3899–3906.
RIZK, N.K. & LEFEBVRE, A.H. 1983 Influence of atomizer design features on mean drop size. *Am. Inst. Aeronaut. Astronaut.* **21**, 1139–1142.
RIZK, N.K. & LEFEBVRE, A.H. 1985 Internal flow characteristics of simplex swirl atomizers. *J. Propul. Power* **1** (3), 193–199.
ROCHETTE, B. 2019 Modélisation et simulation de la combustion turbulente diphasique dans les moteurs aéronautiques. PhD thesis, Institut National Polytechnique de Toulouse.
SANJOSÉ, M. 2009 Evaluation de la méthode euler-euler pour la simulation aux grandes échelles des chambres à carburant liquide. PhD thesis, Institut Polytechnique de.
SANJOSÉ, M., SENONER, J.-M., JAEGLE, F., CUENOT, B., MOREAU, S. & POINSOT, T. 2011 Fuel injection model for Euler–Euler and Euler–Lagrange large-eddy simulations of an evaporating spray inside an aeronautical combustor. *Intl J. Multiphase Flow* **37** (5), 514–529.
SANTHOSH, R. & YADAV, R. 2025 Flame stabilization modes in non-premixed NH3/H2/N2 swirling flames-a numerical study. *Combust. Sci. Technol.* **0** (0), 1–23. https://doi.org/10.1080/00102202.2025.2509855 publisher: Taylor & Francis _eprint:.
SANTHOSH, R. & BASU, S. 2016 Transitions and blowoff of unconfined non-premixed swirling flame. *Combust. Flame* **164**, 35–52.
SANTHOSH, R., MIGLANI, A. & BASU, S. 2014 Transition in vortex breakdown modes in a coaxial isothermal unconfined swirling jet. *Phys. Fluids* **26** (4), 043601. https://doi.org/10.1063/1.4870016 arXiv:.
SARPKAYA, T. 1971 On stationary and travelling vortex breakdowns. *J. Fluid Mech.* **45** (3), 545–559.
SARPKAYA, T. 1995 Turbulent vortex breakdown. *Phys. Fluids* **7**, 2301–2303.
SCHILLER, L. & NAUMANN, A. 1935 A drag coefficient correlation. *Zeitschrift Des Vereins Deutscher Ingenieure* **77**, 318–320.
SHUM-KIVAN, F., MARRERO SANTIAGO, J., VERDIER, A., RIBER, E., RENOU, B., CABOT, G. & CUENOT, B. 2017 Experimental and numerical analysis of a turbulent spray flame structure. In *Proceedings of the Combustion Institute*
SIRIGNANO, W.A. 2010 *Fluid Dynamics and Transport of Droplets and Sprays*, 2nd edn. Cambridge University Press.
SOLI, A. & LANGELLA, I. 2022 Numerical investigation of a coupled blow-off/Flashback process in a high-pressure lean-burn combustor. *ASME. J. Eng. Gas Turbines Power*. **145** (2), 021010.
STONE, C. & MENON, S. 2002 Swirl control of combustion instabilities in a gas turbine combustor. *Proc. Combust. Inst.* **29** (1), 155–160.
SWEENEY, M.S., HOCHGREB, S., DUNN, M.J. & BARLOW, R.S. 2012 The structure of turbulent stratified and premixed methane/air flames II: swirling flows. *Combust. Flame* **159** (9), 2912–2929.
SYRED, N. 2006 A review of oscillation mechanisms and the role of the precessing vortex core (PVC) in swirl combustion systems. *Prog. Energy Combust.* **32** (2), 93–161.
TAAMALLAH, S., DAGAN, Y., CHAKROUN, N., SHANBHOGUE, S.J., VOGIATZAKI, K. & GHONIEM, A.F. 2019 Helical vortex core dynamics and flame interaction in turbulent premixed swirl combustion: a combined experimental and large eddy simulation investigation. *Phys. Fluids* **31** (2), 025108.
TAAMALLAH, S., LABRY, Z.A., SHANBHOGUE, S.J. & GHONIEM, A.F. 2015*a* Thermo-acoustic instabilities in lean premixed swirl-stabilized combustion and their link to acoustically coupled and decoupled flame macrostructures. *Proc. Combust. Inst.* **35** (3), 3273–3282.
TAAMALLAH, S., SHANBHOGUE, S.J. & GHONIEM, A.F. 2016 Turbulent flame stabilization modes in premixed swirl combustion: physical mechanism and Karlovitz number-based criterion. *Combust. Flame* **166**, 19–33.

https://doi.org/10.1017/jfm.2025.10937 Published online by Cambridge University Press

TAAMALLAH, S., SHANBHOGUE, S.J., SANUSI, Y.S., MOKHIEMER, E.M.A. & GHONIEM, A.F. 2015*b* Transition from a single to a double flame structure in swirling reacting flows: mechanism, dynamics, and effect of thermal boundary conditions. In *Volume 5C: Heat Transfer*, pp. V05CT17A014. American Society of Mechanical Engineers.

TANGIRALA, V., R., H., Chen, & DRISCOLL, J.F. 1987 Effect of heat release and swirl on the recirculation within swirl-stabilized flames. *Combust. Sci. Technol.* **51** (1-3), 75–95.

TERHAAR, S., OBERLEITHNER, K. & PASCHEREIT, C.O. 2014 Impact of steam-dilution on the flame shape and coherent structures in swirl-stabilized combustors. *Combust. Sci. Technol.* **186** (7), 889–911.

TERHAAR, S., REICHEL, T.G., SCHRÖDINGER, C., RUKES, L., PASCHEREIT, C.O. & OBERLEITHNER, K. 2015 Vortex breakdown types and global modes in swirling combustor flows with axial injection. *J. Propul. Power* **31** (1), 219–229.

TOMASCH, S., NEDUNCHEZHIAN, S., CHRISTOPH, S. & ERTESVÅG, I.S. 2025 A numerical study of flow structures and flame shape transition in swirl-stabilized turbulent premixed flames subject to local extinction. *Combust. Sci. Technol.* **197** (2), 338–370.

TUMMERS, M., HUBNER, A., VANVEEN, E., HANJALIC, K. & VANDERMEER, T. 2009 Hysteresis and transition in swirling nonpremixed flames. *Combust. Flame* **156** (2), 447–459.

WICKSALL, D.M., AGRAWAL, A.K., SCHEFER, R.W. & KELLER, J.O. 2005 The interaction of flame and flow field in a lean premixed swirl-stabilized combustor operated on H2/CH4/air. *Proc. Combust. Inst.* **30** (2), 2875–2883.

WOLF, P., BALAKRISHNAN, R., STAFFELBACH, G., GICQUEL, L. & POINSOT, T. 2012 Using LES to study reacting flows and instabilities in annular combustion chambers. *Flow, Turbul. Combust.* **88** (1), 191–206.

https://doi.org/10.1017/jfm.2025.10937 Published online by Cambridge University Press